Forschungszentrum Karlsruhe
in der Helmholtz-Gemeinschaft

Wissenschaftliche Berichte
FZKA 7164

Molecular Break-Junctions: Interaction with Light and Conductance Switching

J. U. Würfel

Institut f¨ur Nanotechnologie

August 2005

Forschungszentrum Karlsruhe
in der Helmholtz-Gemeinschaft

Wissenschaftliche Berichte
FZKA 7164

Molecular Break-Junctions: Interaction with Light and Conductance Switching

Jan Ulrich Würfel
Institut für Nanotechnologie

von der Fakultät für Physik der
Universität Karlsruhe (TH)
genehmigte Dissertation

Forschungszentrum Karlsruhe GmbH, Karlsruhe
2005

Impressum der Print-Ausgabe:

Als Manuskript gedruckt

Forschungszentrum Karlsruhe GmbH
Postfach 3640, 76021 Karlsruhe

Mitglied der Hermann von Helmholtz-Gemeinschaft
Deutscher Forschungszentren (HGF)

ISSN 0947-8620

urn:nbn:de:0005-071646

Molecular Break-Junctions: Interaction with Light and Conductance Switching

---

Bruchkontakte mit Molekülen: Wechselwirkung mit Licht und Leitwertsprünge

Zur Erlangung des akademischen Grades eines

DOKTORS DER NATURWISSENSCHAFTEN

von der Fakultät für Physik der

Universität Karlsruhe (TH)

genehmigte

DISSERTATION

von

Dipl.-Phys. Jan Ulrich Würfel

aus

Böblingen

Tag der mündlichen Prüfung:	24. Juni 2005
Referent:	Prof. Dr. Hilbert von Löhneysen
1. Korreferent:	Prof. Dr. Elmar Dormann
2. Korreferent:	Prof. Dr. Heiko B. Weber

Abstract

In this work, we analyzed electronic transport across metal–molecule–metal bridges using gold mechanically-controlled break-junctions. In particular, we studied the influence of illumination on these contacts as well as stochastic conductance fluctuations which can be detected on molecular junctions. When visible light is applied to tunnel junctions, i.e. bare break-junctions, the conductance increases. This can be explained by thermal expansion of the electrodes of the break-junction. Molecular contacts also exhibit an increase of the conductance where the mechanism is not yet clear. Without illumination, we measured the conductance of molecular junctions for extended periods of time, this can be performed for several days. We observed stochastic fluctuations of the conductance where one specific value of fluctuation is preferred. This preferred value is independent of the conductance value of the junction. Such fluctuations were observed on several samples comprising different molecules and might be identified with single molecules breaking and re-establishing chemical contact.

Bruchkontakte mit Molekülen: Wechselwirkung mit Licht und Leitwertsprünge

Kurzzusammenfassung

In dieser Arbeit wurde elektronischer Transport über Metall-Molekül-Metall-Brücken mittels mechanisch kontrollierter Goldbruchkontakte untersucht. Insbesondere ging es dabei um die Wechselwirkung dieser Kontakte mit Licht und um stochastische Leitwertsprünge, die an molekularen Kontakten beobachtet werden können. Wurden Bruchkontakte ohne Moleküle im Tunnelregime beleuchtet, so stieg der Leitwert der Proben an, was durch thermische Expansion der Bruchelektroden erklärt werden kann. Bei molekularen Kontakten zeigt sich ebenfalls eine Stromerhöhung, deren Mechanismus aber noch unklar ist. Ohne Beleuchtung wurde außerdem der Leitwert molekularer Kontakte über lange Zeiträume, bis zu einigen Tagen, beobachtet. Es zeigte sich, dass der Leitwert fluktuiert und dass ganz bestimmte Leitwertsprungamplituden gehäuft auftreten. Die Sprungamplitude ist dabei unabhängig vom Leitwert. Solche Sprünge konnten an mehreren Proben und unter Verwendung verschiedener Moleküle beobachtet werden. Als mögliche Ursache für diese Sprünge werden Moleküle diskutiert, deren chemische Bindung zu den Elektroden reißt und neu gebildet wird.

Deutsche Zusammenfassung

In den letzten Jahrzehnten konnte die Leistung siliziumbasierter Schaltkreise durch fortschreitende Miniaturisierung immer weiter gesteigert werden. Die Größe der kleinsten Schaltelemente nahm dabei exponenziell mit der Zeit ab, was als das Moor'sche Gesetz bekannt ist. Nach diesem Gesetz werden die kleinsten Halbleiterelemente in 10-20 Jahren atomare Größenordnungen erreichen. In solchen Dimensionen können quantenmechanische Effekte nicht mehr vernachlässigt werden. Außerdem steigen die Produktionskosten mit der Miniaturisierung stark an, sodass Alternativen zur Siliziumtechnologie immer mehr in den Blickpunkt aktueller Forschung rücken. Die *Molekulare Elektronik* – bei der einzelne (organische) Moleküle als Schaltelemente eingesetzt werden sollen – ist dafür ein vielversprechender Ansatz. Moleküle sind gegenwärtig die kleinsten vorstellbaren funktionellen Einheiten und können relativ preiswert hergestellt werden. Hinzu kommt, dass die Vielfalt der gesamten organischen Chemie zur Verfügung steht, sodass es vorstellbar ist, für praktisch jede Funktion ein passendes Molekül zu entwickeln.

Bevor molekulare Elemente in der Elektronik zum Einsatz kommen können, muss der elektronische Transport auf molekularer Ebene verstanden werden – dies ist Gegenstand der aktuellen Forschung. Um Stromtransportmessungen an Molekülen zu interpretieren, sollte das untersuchte System so einfach wie möglich gehalten werden. Optimal wären einzelne, chemisch kovalent an die Messelektroden gebundene Moleküle. Dafür werden – neben chemisch geeigneten Komponenten – Elektroden benötigt, deren Abstand sich auf molekularer Größenskala zuverlässig regeln lässt. In dieser Arbeit werden elektronenstrahl-lithographisch hergestellte mechanisch kontrollierbare Gold-Bruchkontakte für diese Aufgabe verwendet. Das Prinzip ist in Abbildung 1.1 auf Seite 3 dargestellt: Auf ein biegsames Substrat wird eine Schicht aus Polyimid (PI) aufgebracht. Auf diese wird elektronenstrahl-lithographisch ein dünner Gold-Draht strukturiert, der eine Engstelle mit einem Querschnitt von etwa 50×50 nm^2 aufweist (eine unter 45° aufgenommene Rasterelektronenmikroskopaufnahme ist in Abb. 1.1 zu sehen). In einer reaktiven Ionenätzanlage wird diese Engstelle unterätzt, sodass eine frei stehende Goldbrücke entsteht. Der Probenchip wird in eine Dreipunkt-Biegevorrichtung eingesetzt (siehe Abb. 1.1). Um Kontaminationen möglichst gering zu halten, befindet sich die Biegevorrichtung in einer Vakuumkammer, die bis zu einem Druck von etwa 10^{-7} mbar evakuiert wird. Unter diesen Bedingungen werden die Gegenlager so lange nach unten bewegt, bis die Goldbrücke reißt. Da die Stempelbewegung in eine Biegung des Substrats umgesetzt wird, die wiederum den Kontakt auf der Oberfläche dehnt, kann der Abstand der Bruch-Kontaktenden mit einer Genauigkeit von unter 0,1 Å variiert werden.

Die in dieser Arbeit eingesetzten Moleküle sind acetylgeschützte Dithiole, die alle nach folgendem Prinzip aufgebaut sind:

$$\underbrace{H_3COC}_{\text{Acetylgruppe}} -S-R-S- \underbrace{COCH_3}_{\text{Acetylgruppe}}$$

Die Moleküle, sie werden in Kapitel 3.2 vorgestellt, unterscheiden sich dabei nur im Zentralteil R. Um molekulare Kontakte zu erreichen, wird die Vakuumkammer belüftet und eine verdünnte Lösung eines der Moleküle auf einen geöffneten Bruchkontakt aufgebracht. Die Moleküle können eine der Acetylschutzgruppen in situ abspalten und durch eine kovalente Schwefel-Gold-Bindung ersetzen. Zu diesem Zeitpunkt überbrückt keines der Moleküle den Spalt zwischen den Elektroden. Wieder in Vakuum wird der Kontakt unter angelegter Spannung langsam geschlossen. Eines der Moleküle wird als erstes die zweite Elektrode berühren und kann dort seine zweite Acetylschutzgruppe durch eine Schwefel-Gold-Bindung ersetzen. An solch einem Gold-Molekül-Gold-Kontakt können reproduzierbare Stromspannungskennlinien bis hin zu Spannungen von ca. 1,5 V aufgenommen werden, wie schon in verschiedenen Arbeiten gezeigt wurde.

Ziel dieser Arbeit war es, die Eigenschaften molekularer Bruchkontakte bei Raumtemperatur näher zu untersuchen. Die Schwerpunkte lagen dabei insbesondere auf der Kalibrierung des Elektrodenabstandes, der Wechselwirkung von Molekül- sowie Tunnelbruchkontakten mit Licht und auf Leitwertfluktuationen von Molekülkontakten.
Die Abstandskalibrierung von Goldbruchkontakten bei Raumtemperatur kann nicht mit Hilfe der üblichen Methoden zur Charakterisierung von Tunnelkontakten durchgeführt werden, da für diese eine hohe Spannung von deutlich über einem Volt angelegt werden muss. Dies ist aber bei Goldtunnelkontakten bei Raumtemperatur wegen starker Oberflächendiffusion nicht möglich. Die verbleibenden Methoden sind: (i) Über geometrische Analyse der Biegevorrichtung und (ii) Durch Messung des Tunnelleitwertes bei kleiner Spannung als Funktion des Abstandes der Elektrodenspitzen. Die von den beiden Methoden gelieferten Abstands-Umrechnungsfaktoren liegen etwa um einen Faktor drei auseinander. Daher wird in der vorliegenden Arbeit in anderes Verfahren gewählt. Wird ein atomarer Goldkontakt auseinander gerissen, lagern sich die obersten Goldatome um. Dadurch vergrößert sich die Lücke zwischen den Goldspitzen. Diese Vergrößerung kann gemessen werden, indem der Goldkontakt wieder geschlossen wird. Dieses Verhalten wurde an jedem in dieser Arbeit untersuchtem Bruchkontakt beobachtet und ist auch in den Abbildungen mehrerer Veröffentlichungen, in denen solche Messungen mit Transmissionselektronenmikroskopen (TEM) oder Rastertunnelmikroskopen (STM) durchgeführt wurden, zu erkennen. Bei letzteren ist die Abstandskalibrierung bekannt und die publizierten Resultate können mit unseren Messungen verglichen werden. Es stellte sich heraus, dass nur die Abstandskalibrierung, die mittels des Tunnelleitwertes durchgeführt wurde, mit der Auswertung der veröffentlichten von TEM und STM Messungen kompatibel ist. Der Leitwert als Funktion des Elektrodenabstandes kann außerdem zur Charakterisierung von Molekülkontakten herangezogen werden. Dadurch können zeitliche Veränderungen besser beobachtet werden und die Strom-Spannungs-Messungen an Molekülkontakten können besser geplant werden.
Für die Wechselwirkung von molekularen oder Tunnelbruchkontakten mit Licht sind eine Vielzahl von Prozessen vorstellbar. Um nur einige zu nennen: In den Elektroden durch Photonen angeregte Elektronen könnten die Transmissionseigenschaften der Molekülkontakte bei bisher unerreicht hohen Energien untersuchen. Elektron-Loch-Paare könnten in der Molekülkontaktregion erzeugt werden. Dabei wäre es wegen der Hybridisierung der Molekülorbitale denkbar, dass das Loch zwar in einer Elektrode erzeugt, das Elektron aber in das höchste unbesetzte

Molekülorbital angeregt wird. Bei solch einem Szenario wäre die benötigte Anregungsenergie durch die am Kontakt anliegende Spannung einstellbar. Wir haben Bruchkontakte mit einem Titan:Saphir-Laser[1] beleuchtet und untersucht wie sich die Beleuchtung auf den Leitwert der Kontakte auswirkt. Der dominierende Effekt war eine Stromerhöhung ΔI unter Beleuchtung, die proportional zum aktuellen Strom I durch den Kontakt war. Diese Stromerhöhung war sehr universell, d.h. sie war unabhängig von der Beleuchtungsart (400 nm gepulst, 800 nm gepulst oder 800 nm Dauerstrich) und auch unabhängig davon, ob molekulare oder Tunnelkontakte beleuchtet wurden. Der Proportionalitätsfaktor $\frac{\Delta I}{I}$ schwankte stark von Probe zu Probe und betrug jeweils einige Prozent. Für Tunnelkontakte kann die Erhöhung durch thermische Expansion der durch die Beleuchtung erwärmten Elektroden erklärt werden: Die Elektroden dehnen sich aus, dadurch wird die Tunnelbarriere enger und der Strom steigt an. Die Temperaturerhöhung liegt dabei etwa bei 0,2 K. Diese Temperaturerhöhung ist konsistent mit einem einfachen thermischen Transportmodell (siehe Kapitel 3.1.4) des Wärmetransportes in Bruchkontaktproben. Bei molekularen Kontakten ist die gemessene Stromerhöhung schwieriger zu erklären: Eine wichtige Eigenschaft von Molekülkontakten ist, dass ihr Leitwert nicht ansteigt, wenn man den Elektrodenabstand leicht verringert. Insofern würden wir auch unter Beleuchtung (und unter Berücksichtigung der daraus resultierenden thermischen Expansion) erwarten, dass der Leitwert eines Molekülkontaktes konstant bleibt. Das ist aber nicht der Fall, sondern der Strom erhöht sich in vergleichbarem Maß wie bei Tunnelkontakten. Werden Kontakte mit einer asymmetrischen Stromspannungskennlinie beleuchtet, so zeigt sich, dass das lichtinduzierte Signal symmetrisch ist. Bei festem Vorzeichen der Spannung gilt nach wie vor $\Delta I \sim I$, jedoch hängt der Proportionalitätsfaktor von der Spannungsrichtung ab.
Molekulare Kontakte sind über mehrere Tage stabil. Während dieser Zeit kann eine kleine Spannung (etwa 10 mV) angelegt und der Leitwert des Molekülkontaktes gemessen werden. Wir untersuchten diese Langzeitleitwertmessungen auf Fluktuationen. Es zeigte sich, dass bei molekularen Kontakten Fluktuationen mit einer festen Amplitude gehäuft auftreten. Diese Fluktuationsamplitude ist unabhängig vom Leitwert des Kontaktes. In Histogrammen der Langzeitleitwertmessungen sind die Fluktuationen als äquidistante Peaks sehr deutlich zu sehen. Solcherlei Fluktuationen konnten wir an mehreren molekularen Kontakten beobachten, bei denen verschiedene Moleküle kontaktiert wurden. Möglicherweise können diese Fluktuationen mit einzelnen Molekülen identifiziert werden, deren chemische Bindung zwischen gebundenem und offenem Zustand fluktuiert. Bei einem der untersuchten Molekülkontakte ist diese Interpretation konsistent mit einer Stromspannungskennlinie, die an unserem Institut in einem anderen Aufbau bei tiefen Temperaturen an einem (vermutlich Einzel-) Molekülkontakt des gleichen Moleküls gemessen wurde.

Mit dieser Arbeit wurde das Spektrum der Untersuchungsmethoden für molekulare Bruchkontakte erweitert. Insbesondere wurden die Abstandsabhängigkeit des Leitwertes und die thermischen Eigenschaften mit in die Auswertung einbezogen. Die Wechselwirkung von Bruchkontakten mit Licht wurde untersucht und konnte für Tunnelkontakte mit einem thermischen Expansionsmodell der Elektroden beschrieben werden. Bei näherer Untersuchung des Langzeitleitwertes von molekularen Kontakten zeigten sich Leitwertfluktuationen mit fester Fluktuationsamplitude. Diese Fluktuationen führen zu äquidistanten Peaks in Leitwerthistogrammen. Eine mögliche Interpretation ist, dass die Fluktuationsamplitude dem Leitwert einzelner Molekül-Metallkontakte entspricht.

[1] Diese Arbeiten wurden in Würzburg in Zusammenarbeit mit der Arbeitsgruppe von Dr. W. Pfeiffer, Physikalisches Institut, EP 1, Universität Würzburg, durchgeführt.

Contents

Chapter 1

Introduction

In the last decades, silicon-based computer technology has experienced a tremendous success by continuously miniaturizing the size of the single transistors down to a feature size of currently roughly 200 nm. In the last years, this decrease in size has followed an exponential time dependence which is known as Moore's Law [1]. Accordingly, within roughly 10–20 years, this development will have reached its natural limits: when the feature sizes on a silicon chip are of the nanometer scale, quantum mechanical effects can no longer be ignored, even at room temperature. In addition, production costs for conventional lithographic silicon technology increase considerably for smaller features. Hence, in the near future, alternatives to silicon technology might become an important issue.

A promising vision to further reduce the feature size is to use single molecules as smallest functional elements. This field of scientific research is commonly denoted as *molecular electronics*. In addition to their size, molecules yield the possible advantage of low-cost production and the full diversity of organic chemistry, i.e. basically any functionality is conceivable considering how many molecular structures are possible. Quantum mechanical effects could be exploited in a controlled manner to yield new functionalities in electronics.

At present, molecular electronics is still a field of fundamental research, where the basic aim is to understand electronic transport on a molecular scale. From the physics point of view, the conductance through molecular systems offers the possibility to directly probe quantum mechanical properties such as energies of electronic orbitals. For recent reviews on molecular electronics, see [1–5].

In order to be able to interpret conductance measurements of molecular junctions, the complexity of the performed experiment needs to be reduced as much as possible. This calls for a stable chemical connection between the molecules and the electrodes. Additionally, it would be favorable to study the conductance of junctions made up of very few or even individual molecules. This is a very delicate task and requires contacts (electrodes) the distance of which can be accurately adapted to the size of the molecule. Whether indeed single molecules are measured is usually deduced from a set of indications. Several techniques have been reported to be able to provide few- or single-molecule contacts. In these publications, it is not unambiguously clear whether single or few molecule contacts are examined, but there are many indications for single molecules.

- Molecules can be embedded in a self-assembled monolayer (SAM) of non-conducting molecules (in most cases alkane mono-thiol SAMs) and studied by a scanning tunneling

microscope (STM) tip [6–9]. However, only in some of these measurements, a chemical contact between the molecule and the STM-tip was established [7–9].

- Xu et al. [10] repeatedly indented an STM-tip into a gold surface. The measurement is performed in a solution containing molecules. By interpreting the distance dependence of the conductance between the tip and the gold surface, the conductance of molecular junctions is deduced.

- Molecules can be contacted in a crossed-wire geometry. A monolayer is assembled on a gold wire several micrometers in diameter and contacted by a second, bare gold wire oriented at 90°. To control the distance of these wires, a current is passed through them and they are mounted in a magnetic field. By varying the field strength or the current, the wires can be approached and single-molecule measurements have been reported [11, 12].

- The mechanically-controlled break-junction (MCBJ) technique [13] can be employed to measure the conductance of molecular junctions. First measurements on such contacts were reported by Reed et al. [14] and followed by publications of several other groups [15–19]. This technique is explained in further detail below, as it was the method of choice for this thesis.

- There are several methods to fabricate nanoscopic gaps on a planar substrate. These can be obtained by shadow-evaporation techniques [20–22], by electrochemical etching methods [23], or by electromigration [24–26]. In most cases, the gap is created first and then the molecules are either evaporated or applied to the sample in a solution. In some electromigration experiments, the molecules are applied prior to creating the gap [24].

In this work, we used lithographically fabricated mechanically-controlled break-junctions (MCBJs) [27] to obtain molecular contacts. The working principle of these junctions is depicted in Fig. 1.1. They consist of a flexible substrate onto which a gold wire is structured by electron-beam (e-beam) lithography. In the center of the sample, the gold wire is underetched, forming a small bridge. The sample is then mounted into a three-point bending mechanism. By moving the pushing rod upwards, the sample surface including the gold bridge is stretched until the bridge breaks. This way, two opposing electrodes whose distance can be controlled with sub-Ångström precision are formed.

Mechanically-controlled break-junctions have proven to be a very successful tool to study single or few-molecule contacts [14–19, 28, 29], and single atom-contacts [27, 30–34]. The work presented in this thesis aims at further elucidating the room temperature properties of lithographically manufactured molecule- and tunnel-MCBJs. In particular, we are interested in the distance calibration, the thermal properties, and the response of MCBJs to illumination. The distance calibration of gold MCBJs at room temperature has never been accomplished to a satisfying degree of accuracy. It can be calculated using the geometry of the sample and setup, or it can be measured by monitoring the tunnel conduction of an open MCBJ while changing its gap width. Both methods differ by a factor of about three. In this work we study the possible reasons for this discrepancy and try to establish a method which can be employed to calibrate the distance dependence of the gold tips for molecular contacts.
When a current is transmitted through a molecular contact, energy is dissipated resulting in heating of the electrodes. Heating may also result from illuminating the junction. We

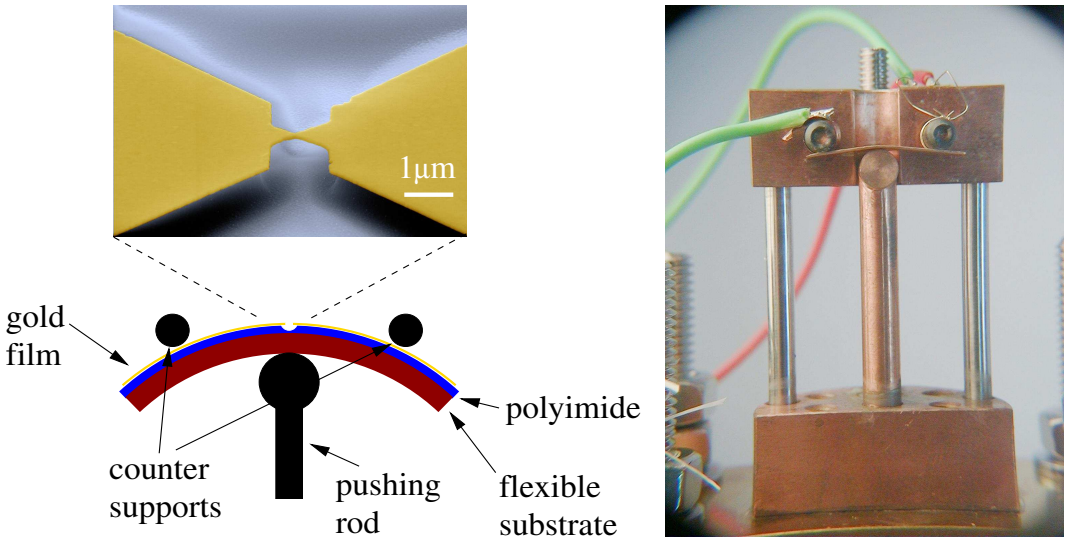

Figure 1.1: *Lithographically manufactured mechanically-controlled break-junctions. Lower left: sketch depicting the working principle. A thin gold wire is lithographically structured onto a bendable substrate and isolated from the latter by a thin layer of polyimide. The central region of the gold wire is a free-standing bridge (see scanning electron microscope (SEM) picture taken under an angle of 45° above the sketch). The sample is mounted into a three-point bending mechanism. Bending the sample stretches the gold bridge until it breaks, thus creating two free-standing gold electrodes whose respective distance can be controlled with sub-Ångström precision. Right: a photograph of the bending setup.*

will estimate the heat conduction properties of lithographically manufactured MCBJs. In principle, the thermal properties of nanoscopic systems can directly be employed: in this work temperature changes in the milli-Kelvin regime are measured as conductance change of the junction.
A multitude of interaction effects is conceivable when light is applied to a molecular MCBJ. To name a few: excited electrons in the leads can probe the electronic properties of molecular contacts at higher energies than those accessible by applying a bias voltage. Electron-hole pairs might be created by exciting an electron from the electrodes into the lowest unoccupied molecular orbital (LUMO) of the molecule. The energetic difference between the chemical potential of the electrodes and the LUMO of the molecule can be controlled by the bias voltage. Hence, this would lead to electrically tunable optical properties of the contact. As last example, the current through metal–molecule–metal contacts could be controlled by light, i.e. optical routers, optical switches and quantum ratchets are conceivable [35]. We will apply light of a titanium-sapphire ultrashort-pulse laser system to mechanically-controlled break-junctions and study the current response of tunnel and molecular junctions.

In summary, by analyzing the tip distance calibration, the thermal properties, and the interaction with light, we want to provide new methods to study and interpret the conductance measurements of molecular break-junctions.

After this introduction, in chapter 2, we will introduce the theoretical framework necessary to describe the measurements and interpretations given in the subsequent chapters. In the

experimental section, chapter 3, we will discuss in detail the sample properties of our MCBJs, the measurement setup used to contact and bend them, and the contact protocol followed to contact molecules in this work. The results obtained from our measurements will be presented and discussed in chapter 4. Finally, we will summarize the results of this thesis in chapter 5. Additional information and quick references about this work are provided in the appendices: In appendix A, a nomenclature table is given as a quick reference which includes most of the variables employed in this work. Some technical terms employed in this work are not standard terminology but rather defined in this thesis. They are listed in appendix B. An overview of frequently used abbreviations such as AFM for "Atomic Force Microscope" is given in appendix C.

Chapter 2

Theoretical Framework

In this thesis, we measure electronic transport through organic molecules coupled to gold leads. In order to interpret the results, it is necessary to introduce the theoretical framework for describing transport through molecules. This is done in sections 2.1 and 2.3. In section 2.2, we specify how the conductance of a tunnel gap can be calculated. This is used to calibrate the distance of mechanically controlled break junctions. What an "ideal" molecular current–voltage characteristic (IV) is expected to look like, will be described in section 2.4. Some of our measurements may be interpreted as conductance through several molecules in parallel. An introduction to this subject is given in section 2.5. To apply light to nanoscopic contacts, some basic knowledge about their optical properties and interactions is necessary and will be presented in section 2.6. Light or the measurement current might produce heat. A brief introduction to thermal transport and expansion is given in sections 2.7 and 2.8.

2.1 Scattering Formalism of Transport

In this chapter the concept of the scattering formalism is briefly introduced. Strictly speaking, it is appropriate when there is no interaction on the scatterer. But it can be used to introduce the concepts of transport on the nanoscale. More detailed descriptions can be found in recent reviews, e.g., [36–38] and books on the subject, e.g., [39, 40]. In the scattering formalism of transport, the mesoscopic system of interest is described by three components: the left and right leads at the chemical potentials μ_L and μ_R, and the scatterer in between them. The scatterer is the system we are interested in, e.g. a molecule between gold tips. For a scatterer with two leads, this is schematically represented in Fig. 2.1. Only quantum mechanical states, which extend over the whole system, can contribute to the current. Constraints such as the lateral dimension lead to different allowed states for the electrons in the subsystems and reduce the local density of states (LDOS) close to the scatterer. Thus, when the three components are brought together, only few states of the reservoirs energetically match the states of the leads and the scatterer, see Fig. 2.1. These states are denoted by Ψ_n and are commonly called *channels*.

One way to calculate the current is to sum up all in- and outgoing states, in one lead far from the scatterer. The incoming and outgoing states from all reservoirs (in the situation described above, the two contacts) of the system are linked via a scattering matrix. In the following, as is common practice, we will only distinguish between the *leads*, i.e. reservoirs plus leads, and the scatterer, i.e. the molecule.

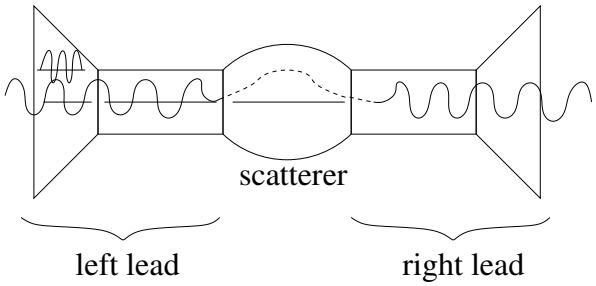

Figure 2.1: *A mesoscopic conductor can be modeled by three components: two reservoir-like leads and the scatterer, in our case a molecule between gold tips. Only states that match the boundary conditions of the leads and the scatterer can extend over the entire structure.*

The states can be partially transmitted or reflected by the scatterer. Because these two properties are linked[1], it is sufficient to know the transmission probability for every extended state. They are described by the transmission matrix $\mathbf{T} = \mathbf{T}(E)$. Its trace is directly related to the current [41]:

$$I = 2\frac{e}{h}\int dE \;\; tr(\mathbf{T}(E)) \;\; \{f(E-\mu_L) - f(E-\mu_R)\} \quad . \tag{2.1}$$

The factor 2 reflects the spin degeneracy, E is the energy of the state Ψ_n, $f(E-\mu_i)$ the Fermi distribution function of the left (L) and right (R) lead at the chemical potential μ_i.
The transmission matrix is energy-dependent in this equation. Transmission may be high at certain energies and low at others. However, at low voltage, an energy–independent transmission matrix is in general a good approximation. Then, eq. (2.1) reduces at zero temperature to:

$$I = 2\frac{e^2}{h} tr\{\mathbf{T}\}V\Big|_{V\to 0} \quad , \tag{2.2}$$

where $G_0 = 2\frac{e^2}{h}$ can be identified as the conductance quantum, $G_0 \approx 77.5\ \mu\mathrm{S} \approx \frac{1}{12{,}9\ \mathrm{k}\Omega}$. In this case, calculating the trace simply corresponds to summing up the transmission of all channels in the eigenbasis.
A formula similar to eq. (2.1) for interacting systems can be derived from the Keldysh formalism. This has been done by Meir and Wingreen [42]. The current is then calculated in terms of the Green's function G of the scatterer—more precisely of the scatterer coupled to the leads. This formula is widely used in theoretical calculations [43, 44].

$$I = 2\frac{e}{h}\int dE \;\; tr(\Gamma_L G \Gamma_R G^\dagger) \;\; \{f(E-\mu_L) - f(E-\mu_R)\} \tag{2.3}$$

Γ_i describes the coupling to the leads.
It should be stressed that the electronic wave function of a free molecule differs considerably from that of a molecule coupled to electrodes. To mention only the most important effects, the molecular orbitals are energetically shifted and broadened. Hence, it is inappropriate to consider "the molecule" as the scatterer. To take account of the interaction, one should

[1] This stems from the unitarity of the scattering matrix and physically corresponds to the conservation of probability.

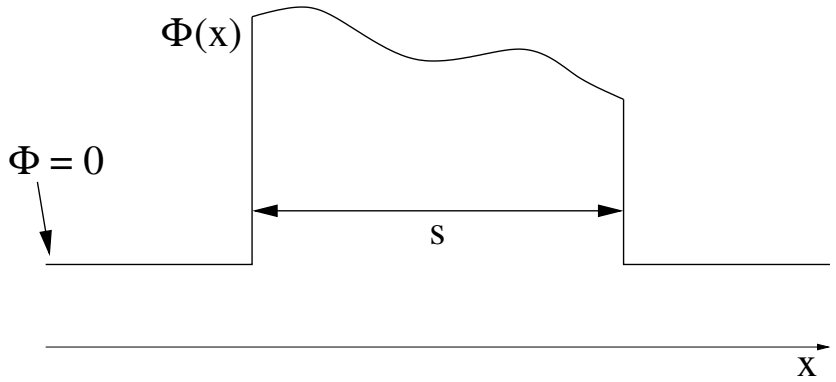

Figure 2.2: *Arbitrarily shaped one-dimensional tunneling barrier $\Phi(x)$. The gap width is denoted by s.*

rather consider the molecule in connection to the closest metal atoms, which is often called the "extended molecule". Concerning theoretical modeling of the extended molecule, Evers et al. [44] found that at least 50 gold atoms at each side are required to sufficiently take account for the metal–molecule interaction.

2.2 Tunneling

In this work, tunneling currents are used to calibrate the distance of the tips of gold break junctions. Thus it is worthwhile to look at how tunneling currents can be calculated.
A comprehensive introduction to this subject can be found in references [45] and [46].

2.2.1 Description of Tunneling Currents

In one dimension (WKB approach)

Often tunneling barriers are described as one-dimensional systems—especially in the case of metal–insulator–metal contacts or oxide layers. "One-dimensional" denotes a system where one assumes current flow exclusively normal to the interface and neglects the finite lateral dimension. These models yield current *densities*, not currents. A sketch of an arbitrarily shaped one-dimensional barrier $\Phi(x)$ is presented in Fig. 2.2.
In one dimension, the transmission probability of a contact can be computed as a scattering problem. Basically, the transmission probability T of a high rectangular barrier ($\Phi \gg e \cdot V$) is given by [45]

$$\begin{aligned} T &= \tfrac{16\,k^2\kappa^2}{(k^2+\kappa^2)^2} \cdot e^{-\frac{2s}{\hbar}\sqrt{2m\Phi}} \\ \text{with} \quad k^2 &= \tfrac{2mE}{\hbar^2} \quad \text{and} \quad \kappa^2 = \tfrac{2m\Phi}{\hbar^2} \quad , \end{aligned} \tag{2.4}$$

where Φ is the barrier height—denoted as $(E - V)$ in most textbooks, E denotes the energy of the particle and V the local potential—, s the barrier width, and m the effective mass of the electron. For arbitrarily but smoothly shaped one-dimensional barriers $\Phi(x)$, the WKB approximation[2] can be used, and the tunneling formulas presented below in section 2.2.3 are

[2]This approximation was first introduced by Lord Rayleigh and then developed by L. Brillouin, H.A. Kramers and G. Wentzel [47]. It would in principle work in higher dimensions but is then very complex.

derived applying this method. But what does "smooth" actually imply? According to [48] the length scale of the variation of the potential profile $\Phi(x)$ has to be large compared to the de Broglie wavelength of the electron. Written as a formula this condition yields:

$$\frac{\hbar}{\sqrt{2m|\Phi(x)|}} \ll \frac{2|\Phi(x)|}{|\frac{d\Phi(x)}{dx}|} \tag{2.5}$$

For an exemplary potential profile given in [49]—barrier height ~ 7 eV and barrier width ~ 5 Å—the inequality is fulfilled (0.9 Å compared with 4.8 Å). Hence, for these parameters, the approximation is justified, but for very small barriers, deviations from the computed tunnel currents can be expected.

In three dimensions (Bardeen's transfer Hamiltonian approach)

If effects of geometry are to be taken into account or in order to explain high resolution imaging of STMs, a three-dimensional approach is necessary. In this approach, developed by Bardeen [50], approximate wave functions are defined on either side of the contact (Ψ_R and Ψ_L), and a transfer Hamiltonian H_T describes the coupling between them. Using these ingredients, the transfer matrix element

$$M_{RL} = \langle \Psi_R | H_T | \Psi_L \rangle = \int d^3r \;\; \Psi_R^* H_T \Psi_L \tag{2.6}$$

can be calculated [45]. The tunneling rate $\Gamma_{R\leftarrow L}$ from L to R then follows from Fermi's golden rule,

$$\Gamma_{R\leftarrow L} = \frac{2\pi}{\hbar} |M_{RL}|^2 D_R(E) \quad . \tag{2.7}$$

If $|M_{RL}|^2$ does not depend on the energy E, the tunneling current is proportional to the density of states D_R of the electrode into which the electron tunnels. This result is widely used to interpret STM images.
For simple rectangular one-dimensional barriers, eq. (2.7) gives the same result as the 1d approach above. Its advantage is that the geometry and approximate wave functions of the tips can be taken into account, for example, s or d waves.

2.2.2 Parameters

Barrier height

For broad barriers between identical substances, a rectangular tunneling barrier height $\Phi(x) \equiv \Phi$ is to a good approximation the same as the work function W of the material. Several effects can influence this relationship:

1. For very thin barriers ($s \lesssim 3 \cdots 5$ Å), the barrier is reduced compared to a wide barrier of the same material [45, 51].

2. As a consequence of adsorbates on the contacts the work function can change up to about $\Delta W \approx \pm 1$ eV. For example, W is increased for He [52–54] or O_2 [55], and decreased for hydrocarbons [55].

3. The very strong electrical fields of thin biased barriers might lower the barrier height.

W [eV]	type of measurement	reference
$3.3 \cdots 4.3$	apparent barrier height of 10 Au MCBJs	[51]
4.0 - 4.58	thermally	in [58]
4.3	not specified	[57]
4.7 ± 1	apparent barrier height in STM	[59]
4.8	photoelectric work function	[60]
4.81	DuBridge's monochromatic method	in [58]
4.83 ± 0.02	contact potential against barium	[58]
4.90	by photoelectric effect	in [58]
5.1	by photoelectric effect	[61]
(5.2 ± 0.35)	e^- tunneling in the Fowler–Nordheim regime	[62]
5.3	by calibrating the distance of gold MCBJs	[30]

Table 2.1: *Selected values of the work function of gold from the literature with references.*

4. The geometry of the tunneling tips can influence the potential profile and lead to deviations from $T \propto e^{-\frac{2s}{\hbar}\sqrt{2m\Phi}}$. This has been studied by, e.g. Keijsers et al. [56].

5. Image charges may have to be taken into account. This matter is apparently not yet settled [45], see below for more details.

Work function for gold

The work function is defined [57] as the work that has to be performed to transfer an electron from inside the bulk material to some atom layers outside of the crystal. It must not be confused with the chemical potential of the material. The topmost elementary cells of a crystal are usually deformed and thus yield a dipole field. Moving the electron through this field accounts for most of the difference between work function and chemical potential. This is also the reason, why the work function depends on the crystal orientation of the surface. In the literature, large differences can be found for the work function of gold. Some of them are listed in table 2.1. In this thesis, we will use:

$$W_{\text{gold}} = 4.8 \text{ eV} \tag{2.8}$$

Traversal time for tunneling

How long does it take an electron to tunnel? This seems at first sight to be of purely academic interest, but is also important for the question of whether image charges have to be taken into account. A formula to estimate the traversal tunneling time was derived by Büttiker in 1982 [63] and compared to other approaches. The idea is the following: in a gedankenexperiment an electron tunnels through a barrier of time-modulated height. For low frequencies, the particle sees a static barrier. For high frequencies, the particle tunnels through a time-averaged potential, but can do so inelastically, losing or gaining modulation quanta. The crossover of these regimes yields the transversal time t and is given by:

$$t = \int\limits_{\text{barrier}} dx \sqrt{\frac{m}{2\Phi(x)}} \tag{2.9}$$

For a rectangular barrier of height $\Phi = 4.8$ eV, width s, and the free electron mass $m = 9.11 \cdot 10^{-31}$ kg, we get

$$t = \begin{cases} 3.8 \cdot 10^{-16} \text{ s} & \text{, for } s = 5 \text{ Å} \\ 7.7 \cdot 10^{-16} \text{ s} & \text{, for } s = 10 \text{ Å} \end{cases} . \tag{2.10}$$

Do we have to consider image charges?

As mentioned above, the answer is not obvious. Some questions should be considered:

1. A tunneling particle is a virtual particle. Classical calculations of this clearly quantum mechanical problem must be taken cum grano salis.

2. Building up image charges is a screening effect for which electrons need a certain reaction time. This time is given by the inverse of the plasma frequency in the respective metal. For gold [64], $\omega_p = 1.36 \cdot 10^{16} \frac{1}{\text{s}}$, corresponding to a reaction time of $\tau = 4.6 \cdot 10^{-16}$ s. Looking at eq. (2.10), this is about the time the electron needs to tunnel. Thus, the metal electrons can only partly screen the field of the tunneling electron.

Luckily, the image-charge question is less important than it may seem. According to Binnig et al. [49], image charges lead to a strong increase in current but are not visible when the evolution of the conductance as a function of the barrier width is measured. This is in good agreement with STM-measurements down to 3 Å [45].

2.2.3 Fit Formulas for the Tunneling Conductance

Simmons formula

Using the WKB approximation, Simmons [65] derived a formula giving the tunneling current for all bias regimes, i.e. eV $\ll \Phi$, eV $\approx \Phi$ and eV $\gg \Phi$. Note, this is a one-dimensional formula, so as mentioned in section 2.2.1, the calculation yields a current *density*. In order to find the *current*, the cross section of the contact has to be known. Whereas this is known in some geometries, e.g. metal–insulator–metal structures, it is unknown for our setup. The conductance G_0 in approximation for low bias is given by:

$$\boxed{G_0 = A \, \frac{\sqrt{2m\Phi}}{hs} \frac{e^2}{h} \, e^{-\frac{2s}{\hbar}\sqrt{2m\Phi}}} \tag{2.11}$$

A is the cross section through which the current flows, s the barrier width, m the electron mass, and Φ the barrier height. A possible estimate for the cross section A is the area of a single gold atom which is approximately the square of the nearest neighbor distance in fcc gold: $A \approx (2.9 \text{ Å})^2 = 8.4 \text{ Å}^2$.

BDR formula

Up to now, we only considered linear transport, but in principle, higher orders in the applied voltage should be taken into account. This has been done up to third order by Brinkman, Dynes and Rowell [66]. They give a formula for the first derivative of the current dI/dV, here denoted as $G(V)$.

$$\frac{G(V)}{G_0} = 1 + \frac{s^2 e^2 m}{4\Phi\hbar^2} \cdot V^2 \tag{2.12}$$

For barriers of trapezoidal shape at zero bias, there is an additional term linear in V which is not important for us. The constants and notation are the same as in the Simmons formula, eq. (2.11). For practical applications, the following partly evaluated formula is useful:

$$\frac{dI(V)}{dV} = \frac{G(V)}{G_0} = 1 + \left(3,28 \cdot 10^{-2} \frac{\mathrm{eV}}{\mathrm{V^2 \mathring{A}^2}}\right) \cdot \frac{s^2}{\Phi} \cdot V^2 \tag{2.13}$$

2.3 Resonant Tunneling

When a voltage V is applied to a contact, the chemical potential of one lead is shifted upwards with respect to the other by eV. Hence, an energy window is opened in which the transmission properties of the contact is probed. When the energy at which a particular orbital has nonzero transmission is inside this voltage window, a current can flow. The energy at which the orbital has nonzero transmission can be depicted as energy level. The level is broadened $\propto \Gamma$ due to the coupling Γ of the orbital to the electronic states of the leads.
The coupling of the molecular orbitals to the leads also changes the electron density on the molecule and in the leads in its vicinity. As a consequence, this can involve charging the molecule. In this work, we used especially designed molecules which have sulphur anchoring groups that bind covalently to the gold leads. Because of the electronegativity of sulphur, the contacted molecule is most likely charged negatively, and the states of the coupled molecule are shifted to higher energies compared to the free molecule. The HOMO (highest occupied molecular orbital) would then lie closer to the chemical potentials of the leads than the LUMO (lowest occupied molecular orbital). Such a situation is depicted as energy alignment picture in Fig. 2.3, where the sulphur anchoring groups are interpreted as tunneling barriers. The point level with the chemical potentials of the leads, denoted by ε, will be called *energy alignment point* in this thesis. It can be used to describe the shift and alignment of the molecular orbital energies as a function of the applied voltage. In this description, the energy difference ΔE between the molecular orbital energies and the energy alignment point ε is kept fixed and ε is shifted with respect to the chemical potentials of the leads according to the assumed voltage drop which depends on the coupling.
When a voltage V is applied to the system, the chemical potentials are shifted by eV with respect to each other. How the voltage drops across the contact, depends on the polarizability of the molecule and its surroundings as well as on the coupling to either electrode. A current can flow only if (i) an orbital of the extended molecule is within the energy window eV and (ii) this orbital has a nonzero transmission. The two extreme cases of coupling are:

1. STM–like coupling: One side is very weakly coupled, the other very strongly. Then ε is more or less fixed to the chemical potential of the well coupled side. This situation is shown in Fig. 2.4.

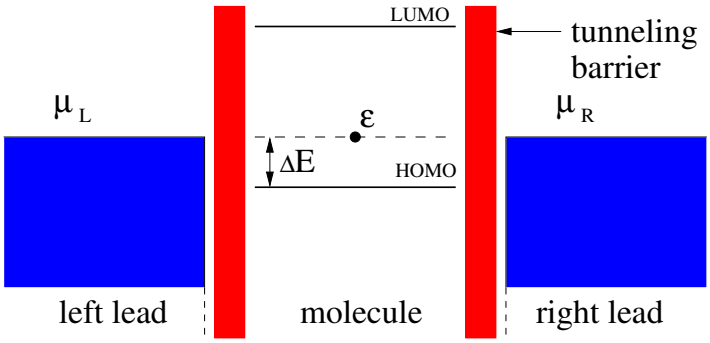

Figure 2.3: *To describe transport, it is convenient to present the energies of possibly transmitting orbitals of the coupled molecule and the chemical potentials of the leads in an energy alignment picture. The sulphur atoms, which couple the molecule to the leads, are interpreted as tunneling barriers. ε is the energy alignment point, which is in equilibrium equal to the chemical potentials μ_L and μ_R of the leads.*

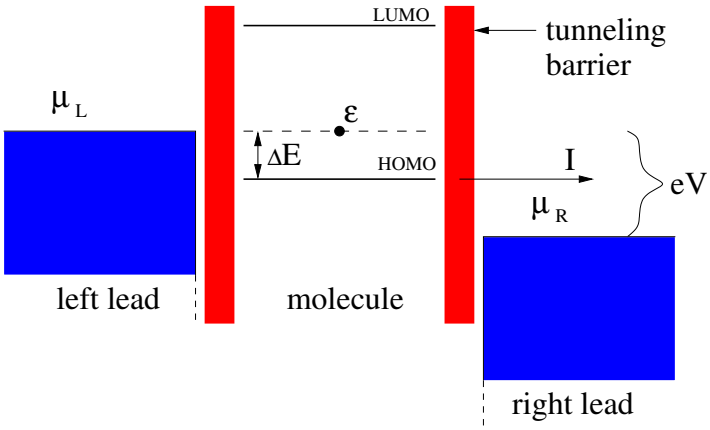

Figure 2.4: *STM–like coupling: the left electrode is strongly coupled to the molecule, thus ε and μ_L are basically at equal height while the chemical potential μ_R of the weakly coupled electrode is lowered with respect to the molecular levels. If the HOMO has a nonzero transmission and $eV > \Delta E$, a current I can flow.*

2. Symmetric coupling: In this case, ε will be located exactly halfway between the two chemical potentials of the leads, as depicted in Fig. 2.5.

In this simple picture, the movement of the molecular levels with respect to the chemical potential on each side of the contact, i.e. $\varepsilon - \mu_i$, is proportional to V. This is not entirely correct when an orbital comes into resonance with the chemical potential of a lead. In this case the occupancy of the orbital will change and the additional charge distributed on the orbital will oppose the electrical field. Thus, during the filling of a molecular orbital, the levels will "move" slower when V is changed compared to when no orbital is in resonance.

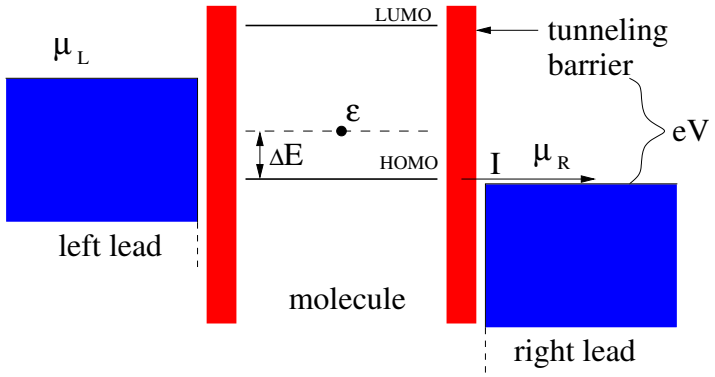

Figure 2.5: *Symmetrical coupling of the molecule to the electrodes. ε lies halfway between the chemical potentials of the leads. If the HOMO has a nonzero transmission and $eV > 2\Delta E$, a current I can flow.*

2.4 Single-Molecule Contacts

2.4.1 Ideal Molecular Current–Voltage Characteristic

An ideal molecular current–voltage characteristic (IV) of a symmetric molecular contact can be explained using the energetic picture shown in figures 2.3 and 2.5. The electronic coupling Γ due to hybridization results in a level broadening, which is at zero temperature given by $\pi\Gamma$ [36]. No current will flow for small voltages $|V| \lesssim (\frac{2\Delta E}{e} - \frac{\pi\Gamma}{2})$. Note, Γ can be different for each orbital. For higher voltages $|V| \gtrsim (\frac{2\Delta E}{e} + \frac{\pi\Gamma}{2})$, the energy dependent transmission through the orbital drops to zero, thus the current will not rise further until the next orbital with nonzero transmission, e.g. the LUMO in Fig. 2.5, comes into the voltage window. The resulting IV is displayed in Fig. 2.6. For a symmetrically coupled one level system at zero temperature, the maximum current $I_{\max}$ through this level and the coupling to the leads Γ are connected by [36]:

$$I_{\text{one level}} = \frac{2e}{h}\pi\Gamma \quad , \tag{2.14}$$

including the factor 2 for spin.

2.4.2 Additional Broadening

Often, especially at high temperatures, the peaks of the dI/dV are broader than expected from eq. (2.14). Additional broadening can stem from the following effects:

1. The IV is washed out by temperature broadening of the Fermi function. This will be about $4k_BT$, but is not enough to explain the broadening found in experiment.

2. Coupling to phonons and vibrations will broaden the dI/dV peak, but also be of the order of k_BT.

3. An asymmetrically coupled molecule, e.g. $\Gamma_L \ll \Gamma_R$ (R, L denoting the right and left lead respectively), can still lead to a symmetric IV. But the current magnitude will be determined by the weak coupling Γ_L whereas the broadening will be dominated by the strong coupling Γ_R.

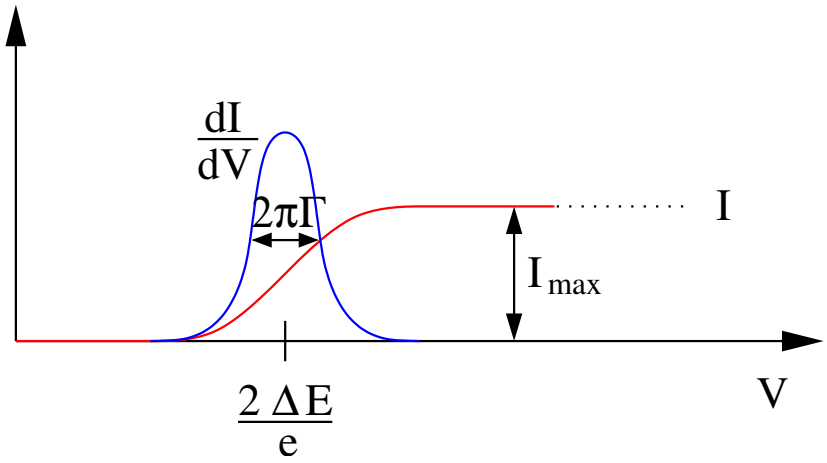

Figure 2.6: *Ideal IV of a molecular contact like the one shown in Fig. 2.5. Only the positive branch of the symmetric IV is displayed. Around $eV = 2\Delta E$ transport through the HOMO starts, reaching a constant current I_{max} for higher bias. The current is shown in red, the differential conductance dI/dV in blue. $\pi\Gamma$ is the level broadening.*

4. Due to the capacitive (polarizable) environment of a molecule, it is possible, even probable, that not the full voltage actually drops across the molecule but rather only a fraction of it: $V_{\text{real}} = \eta V_{\text{external}}$, $\eta \leq 1$. When a voltage of ΔV_{real} is necessary to sweep across a broadened molecular energy level, an external voltage of $\Delta V_{\text{external}} = \frac{1}{\eta}\Delta V_{\text{real}} \geq \Delta V_{\text{real}}$ has to be applied.

5. Inhomogeneous broadening: at room temperature, several energetically very close realizations exist of how the bond between gold and sulfur is established. Fast fluctuations between these contact configurations are possible. The energy of maximum transmission will depend on the exact contact realization, thus the dI/dV peak is actually a time average over the transmission functions of the different possible binding configurations.

   In addition, the position or angle of the molecule in the junction might change in the course of the fluctuations. This can change the local capacitive environment and influence the IV in general, and with it the peak position of the dI/dV.

2.4.3 Asymmetric Current–Voltage Characteristics of Symmetric Molecules

Theoretically, contacts with symmetric molecules should lead to symmetric molecular contacts and result in a symmetric IV. But in experiment, IVs of symmetric molecules often exhibit slight asymmetries. How can these be explained? Several models predict asymmetric IVs of contacts realized with symmetrical molecules.

1. The strongly electronegative sulfur atom might enhance the local density of electrons, leading to a local partial charge. Depending on the respective coupling and capacitive environment of the bond, the amount of charge accumulated can differ for the two bonds, leading to an initial dielectric moment of the metal–molecule–contact. An applied voltage will weaken or amplify this initial moment, and the IV is shifted on the

voltage axis. Probably the voltage drop will be different from the potential profile produced by the sulfur atoms. Then, it is not possible to compensate the initial dielectric moment and the IV will be asymmetric, even if the voltage shift is corrected for.

2. Asymmetric voltage drop. Asymmetric coupling or an asymmetric local capacitive environment can lead to an asymmetric voltage drop. If the voltage mainly drops on one contact, the center of the molecule will be at a different potential when the bias is reversed.

3. Asymmetric coupling leading to different occupancy of a level [67]. Consider an orbital coupled slightly asymmetrically to the two electrodes. The occupancy of this orbital will adjust its occupancy to be similar to the electrode, it is well coupled to. Thus in one bias direction—if the well coupled electrode is negatively biased—it will be occupied whereas it might be empty for reversed bias. The charge distribution on the molecule is then bias dependent and results in an asymmetric IV.

4. Strong asymmetric coupling (STM like). For very asymmetric coupling, reversed bias will probe the transmission of different orbitals. In Fig. 2.4, the current will pass through the HOMO. For opposite bias, the LUMO will be the first orbital in the energy window defined by eV.

2.5 Many-Molecule Contacts

2.5.1 Theory

Yaliraki et al. [68] use the scattering formalism via Green's Functions which are calculated in the tight binding approximation. The molecules are modeled by a series of electronic sites and only nearest neighbor coupling between them is considered. Non–interacting molecules and molecules interacting on one or all sites are discussed. For weakly interacting molecules far enough apart (more than 3 Å), the conductance scales linearly with the number of molecules. For smaller distances deviations from the linear relationship result from the change of the local density of states (LDOS) at the site where the molecule is coupled. Note, the molecules described in this publication are non conjugated in contrast to the molecules used in our experiments.
Lang et al. [69] studied the properties of parallel chains of carbon atoms coupled to the electrodes using the "semi–infinite uniform–background model". Note, chains of carbon atoms are not chemically stable, it is thus questionable if this approach can describe real molecules. The main conclusion is basically the same as obtained in [68]. For a molecular spacing larger than 3 Å there should be no influence. The same approach has been investigated by Lagerqvist et al. [70] and yields the same results. In addition, a further interaction mechanism is mentioned: for coherent electronic transport, there could be interference effects from transport paths through neighboring molecules.

2.5.2 Experiment

Cui et al. [7] measured IVs of octanedithiol in an octanemonothiol monolayer using an STM tip. They report IV characteristics, whose current magnitudes scale as integer multiples of up to 5 of one fundamental IV.

Kushmerick et al. [11] measured the current through a monolayer of asymmetric conjugated molecules in a crossed wire setup. The molecules are bound to one gold wire via a CN–group and there is no chemical binding to the second gold wire. As in [7], the current of the IVs can be divided by integer numbers to lie on a fundamental IV. These integer numbers range from 5 to 1119.
Xu et al. [10] measured the conductance of a solution containing $4, 4'$ bipyridine, hexanedithiol, or decanedithiol molecules by repeatedly opening and closing a nano gap between a gold STM tip and a gold sample. They measured the conductance at eight different voltages up to 0.8 V. In the conductance histograms up to three equidistant peaks are visible and are interpreted as conductance through one, two and three molecules. Note, the IVs published in [7], [10], and [11] resemble very much to IVs expected for a tunneling contact.
Ohnishi et al. [71] managed to measure the conductance through two parallel monoatomic gold chains while taking images of the contact in a UHV–TEM, and found a conductance of $2G_0$. It is not clear whether the results are influenced by carbon contamination, because in the same experiment, an unnaturally large spacing between the gold atoms was found.

In conclusion, it is not clear at present whether the conductance of many molecules in parallel will simply scale linearly with the number N of molecules, ($G_{\ N \text{ molecules}} \stackrel{?}{=} N \cdot G_{\ 1 \text{ molecule}}$). But there are theoretical and experimental indications that this might be the case, in particular for weakly interacting molecules, like alkane chains. This thesis aims at further examining this point, see chapter 4.4.

2.6 Influence of Light

In section 4.3 we will report on measurements where we applied light to the molecular and tunnel junctions. The optical properties of nanoscopic metallic samples differ to a large extent from the macroscopic properties of the material. Here, we will introduce some of the effects that lead to these differences. In general, no quantitative predictions are possible.

2.6.1 Optical Properties of Nanoscopic Metallic Structures

When the dimensions of a metallic sample are of the same order as or smaller than the light wavelength, the optical properties are influenced to a large extend by surface plasmons. Other important effects are the field enhancement and antenna effects which result from the strong curvature of nanoscopic structures.
Influence of surface plasmons: for nanoscale metal structures the influence of surface plasmons is very important. For example, the colors—i.e., their absorption spectrum—of gold colloids is almost entirely determined by their size. Similarly, the optical properties of two adjacent gold tips or an STM tip close to a metal surface will depend on the local plasmon resonance of that particular geometry. The light emission properties of STMs on metals have been extensively studied in the group of Berndt [72–74]. Surface plasmons can also strongly enhance the transmission probability through a nanoscopic hole [75, 76].
Field enhancement: Metallic nanoparticles or tips in the vicinity can increase the local electrical field of light by orders of magnitude [77]. This effect is used in surface enhanced Raman spectroscopy, see e.g. [78], and makes it possible to measure Raman spectra of single molecules.

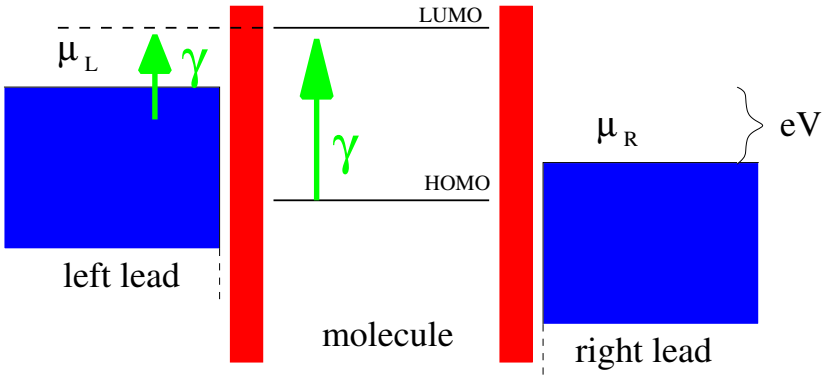

Figure 2.7: *Excitation of electrons into the LUMO by light. If the LUMO is coupled to the electronic states in the leads, electrons can be excited into the LUMO from the leads in addition to from the HOMO. The minimum energy required for this process can then be tuned by the applied voltage V.*

Antenna effects: Metal tips can act as antenna for the incoming radiation. This will amplify the electromagnetic field and is, e.g., important when working with an STM tip in a microwave field [79].

To summarize, it is difficult to predict the optical properties of a nanoscopic metal contact. The absorption resonance can be considerably different from the bulk material and the field between the metal tips may be enhanced by orders of magnitude compared to the light field when no metal tips are present.

2.6.2 Influence of Light on the Electron Transport in a Molecular Junction

The influence of light on a molecular (or tunnel) contact can be classified in more excitation like processes where photons are absorbed and more field-induced effects, where the light is described as alternating electrical field.

Excitation-like effects

- Electrons from the leads or the highest occupied molecular orbital (HOMO) might be excited into the lowest unoccupied molecular orbital (LUMO), leading to a current at a voltage where the conductance of the molecular junction is zero. This is schematically depicted in Fig. 2.7. By applying a voltage to the contact, the energy difference between the chemical potentials of the leads and the LUMO can be tuned. The excitation from the leads to the LUMO is possible if the latter is coupled to the electronic states in the metal. Photonic excitation at microwave frequencies of tunneling electrons across a gap between superconductors has been observed, e.g., by Dayem et al. [80].

- Electrons in the leads might be excited by the incident light up to photon energies $h\nu$ above the chemical potential of the lead μ. Including the applied bias V, energies up to $\mu + \frac{eV}{2} + h\nu$ can be reached on a symmetric contact. Hence, the transmission properties of molecular contacts can be probed to higher energies than precedently—in our experiments, the contacts are only stable up to voltages of approximately 1.5 V. The

excited electrons thermalize into a hot electron gas after several tens of femtoseconds and finally relax after a few picoseconds [79].

- When the molecule is excited by light, it may alter its electrical transport properties. If the excitation lifetime is high enough, this may be measured. By this, the HOMO–LUMO gap of a bound molecule could be deduced. This would also give hints about a change in the absorption cross section due to the presence of the metal tips.
- Possibly, the light excitation can couple to vibronic states of the molecule–metal complex. Surface enhanced Raman spectroscopy [78] is conceivable.
- Electron–hole pairs excited on an asymmetric contact could generate a photo-voltage or -current.

Effects described by the alternating field

- An alternating electrical field between two conducting tips will induce an alternating voltage across the contact. An alternating voltage applied to a contact exhibiting an asymmetric IV can lead to an average DC current [79].
- Quantum ratchet effect: a driving force (the light) on an asymmetric device can lead to a current [35].
- Current control by light, e.g., resonant current amplification, coherent destruction of tunneling, or current routers [35].
- Attractive electrostatic forces induced by the light field between the tips could reduce the gap width.

Thermal effects

- The junction could heat up due to the illumination and the electrodes thermally expand.
- Thermoelectric effects [81] could be studied when the electrodes are heated asymmetrically.

2.7 Heat Conduction

In mesoscopic conductors, heat is usually not dissipated on the scatterer (the molecule), but in the leads close to the contact. The heat transport away from the junction can then be described classically. In order to estimate the heating of the junction region due to illumination or the measurement current through a molecular contact, we need to know the thermal properties of the samples. A thorough introduction to heat conduction can be found, e.g., in [82] or [83].

Steady State Linear Heat Conduction

The linear, steady state heat conduction through a rod is described by:

$$\dot{q} = -\lambda \frac{\Delta T}{L} \quad , \tag{2.15}$$

where $\dot{q}$ is the heat flux (given in $\frac{\mathrm{W}}{\mathrm{m}^2}$), ΔT the temperature difference between the hot and cold ends of the rod, L the length of the rod and λ the thermal conductivity of the rod material.

Analogy to Electrical Circuits

A convenient way of describing thermal conduction is by analogy to electrical circuitry. Thermal resistances correspond to electrical resistances, heat transfer rates to electrical currents, and temperature differences to applied voltages.

$$\begin{array}{llcll} \text{electrical resistance} & R_{\mathrm{el}} & \hat{=} & R_{\mathrm{th}} & \text{thermal resistance}, \quad [R_{\mathrm{th}}] = \frac{\mathrm{K}}{\mathrm{W}} \\ \text{current} & I & \hat{=} & \dot{Q} & \text{heat transfer rate}, \quad [\dot{Q}] = \mathrm{W} \\ \text{current density} & j & \hat{=} & \dot{q} & \text{heat flux}, \quad [\dot{q}] = \frac{\mathrm{W}}{\mathrm{m}^2} \\ \text{voltage} & V & \hat{=} & \Delta T & \text{temperature difference}, \quad [\Delta T] = \mathrm{K} \end{array} \tag{2.16}$$

With these thermal quantities calculations of heat resistance networks can be performed just like for electrical circuits. The thermal resistance[3] is given by:

$$\boxed{R_{\mathrm{th}} = \frac{L}{\lambda \cdot A}} \tag{2.17}$$

Transport Across Interfaces

The thermal resistance $R_{\mathrm{th,\ interface}}$ of an interface of cross-section A can be calculated from the specific thermal contact resistance $\hat{R}$ (in units of $\frac{\mathrm{Km}^2}{\mathrm{W}}$) which is characteristic for each interface.

$$R_{\mathrm{th,\ interface}} = \frac{\hat{R}}{A} \tag{2.18}$$

The thermal contact resistance across an interface of joint substances is very difficult to estimate because it depends very sensitively on the contact details such as defects, impurities, and surface roughness [83]. This is especially true at room temperature. The best way to estimate a thermal contact resistance is to find a similar interface of which the resistance has been measured.

2.8 Thermal Expansion

When the samples are heated up, they will in general expand thermally. The linear thermal expansion coefficient α is defined as [57]:

$$\alpha = \frac{1}{L} \left(\frac{\partial L}{\partial T} \right)_p \tag{2.19}$$

In linear approximation, we can use

$$\frac{\Delta L}{L} = \alpha \Delta T \tag{2.20}$$

[3] In this thesis, the index discerning between thermal and electrical resistances is usually omitted. In most cases, it is clear from the context which resistance is addressed.

to calculate the change of the length ΔL of a sample of total length L when its temperature is changed by ΔT.

Chapter 3

Experimental

For our experiments, we used mechanically-controlled break-junctions (MCBJs), in a version where the sample is manufactured by electron-beam (e-beam) lithography [13, 27]. This technique provides a gold electrode pair, whose respective distance can be controlled with an extremely high distance resolution — much better than atomic length scales. The distance is mechanically tuned by a step motor, the movement of which is enormously reduced by the specially chosen geometry. The technique was invented in the 1990s for the investigation of single-atom contacts. In the following section 3.1 we will introduce how the samples were produced and describe their properties. The molecules which were investigated in this thesis are described in section 3.2. Then, in section 3.3 we describe in detail the measurement setup we employ to build metal–molecule–metal contacts. The optical setup for applying light to the contacts is described in section 3.4. Finally, we describe how the molecules are contacted in section 3.5.

3.1 Samples

3.1.1 Sample Preparation

The starting material for a MCBJ is a highly flexible substrate. We use spring steel[1] (0.2 mm thick) and phosphor bronze[2] (0.3 mm tick) for this purpose. As first step, a wafer with 8 cm diameter of a metal sheet was prepared and later the samples were cut from this wafer prior to lithography. First, the wafers were polished down to grain sizes of 1 μm or less. On these, polyimide[3] (PI) was applied by spin coating and pre-baked for 30–45 min at 250°C. Then the wafers are — within 4 hours — hard-baked in a vacuum oven at 400°C for half an hour. The thickness of the PI layer amounts to 4 μm, measured by ellipsometry in our institute.

E-beam lithography

In this work we will only briefly describe electron-beam (e-beam) lithographic structuring. The reader is referred to the literature, where lithography is described in detail, see e.g. [85].

[1] 0.1 % C, 1.1 % Si, 1.1 % Mn, 16.5 % Cr, 6.5 % Ni, Güte: 1.4310, obtained from [84].
[2] 96 % Cu, 4 % Sn.
[3] In literature often referred to as Capton®.

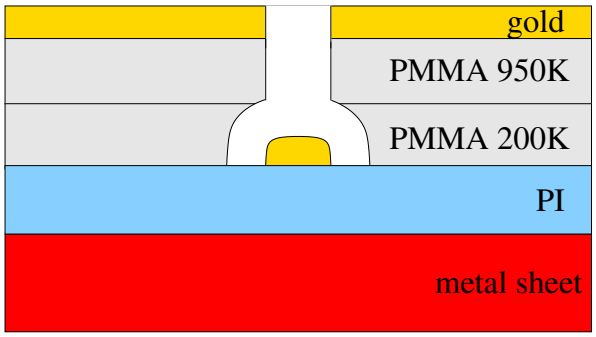

Figure 3.1: *Scheme of the cross section of a sample after electron-beam exposure, developing, and evaporating gold. The sensitivity of the lower PMMA layer is higher than that of the upper layer which leads to an undercut. Thus the upper layer defines the form of the gold structure evaporated onto the sample, while the lower layer acts as support for the upper layer and is not touched by the gold. Distances in this figure are not to scale.*

As e-beam lithography resist, two layers of PMMA[4] are spin cast on the PI layer. In our case, the lower layer consisted of 200 K[5] PMMA, the top layer of 950 K PMMA. By irradiation of electrons the long PMMA molecules are dissected into smaller pieces.
The irradiated sample is then immersed into a solvent which dissolves the shorter molecule fragments much faster than the long intact molecules. The irradiated parts of the sample then appear as "trench" in the PMMA mask. This way, any structure can be "written" into the resist.
Next, gold is evaporated on the structure at a chamber pressure below 10^{-8} mbar. The sensitivity of the lower PMMA layer is higher, hence the lithographic structures are wider in the lower PMMA leading to an undercut. This ensures that there is no contact between the actual structure on the substrate and the excess gold on the PMMA. A schematic cross section of the sample after evaporation is shown in Fig. 3.1.
Both unexposed PMMA layers as well as the gold layer on top of them are removed by immersing the sample in acetone for a few hours. This *lift–off* process can be assisted by briefly dipping it into an ultrasonic bath. What remains is the gold structure deposited in the trenches.

Steps of sample preparation

The whole procedure consists of the following steps:

- Cutting a 7×17 mm chip from the wafer.
- Writing with the e-beam of a scanning electron microscope (SEM) equipped for e-beam lithography at 10 kV acceleration voltage. For redundancy reasons, two entire structures are written on each chip. Only one of them is later used for the experiments.

[4] PMMA is short for "poly(methyl methacrylate)".
[5] The "K"-numbers are a measure of the average molecular mass. 200 K corresponds to 200 000 u. For more details see [86].

- Development in a solution of (MIBK[6]:isopropanol 1:3) for seven seconds. The development is stopped in pure isopropanol.
- Evaporating 40–60 nm of gold normal to the sample surface. *No* titanium adhesion layer is used for purity reasons. Titanium may react with organic substances [87].
- Performing the lift–off in acetone
- Rinsing in isopropanol
- Applying conductive silver to the pads on the outer parts of the sample. Later, these are used to electrically contact the sample. The conductive silver is dried for about half an hour in an oven at 70°C.
- Isotropically etching a few 100 nm deep into the PI by reactive ion etching (RIE) using the following parameters and gases:
  - 50 sccm O_2
  - 2 sccm SF_6
  - Forward power: 50 W *or*[7] DC–bias: 114 V
  - Pressure: 130 mTorr
  - Etching time: 3.5 min.

  After etching, the bridge is suspended as the isotropic etching process has removed the PI from underneath the narrowest part of the structure.
- Looking at the structure in the SEM—images were taken quickly and in low quality (i.e. low current) to keep the contamination by carbon low. These images were used for statistical analysis.

Each chip has a unique sample–id indicating the wafer ('W') from which it was cut and a serial chip number ('C'). The two junctions are addressed by 'S1' and 'S2'. For example, the full sample–id of the first bridge of the seventh chip cut from wafer N° 106 would be W106C07S2. The sample number will be given for all measurements to clarify which measurements were performed on the same sample or on samples originating from the same wafer.

3.1.2 Sample Geometry

A sketch of the top view of the bridge is shown in Fig. 3.2. The opening angle is $\alpha = (67 \pm 2)°$. The length of the freestanding bridge cannot be directly measured in the SEM images. It is needed to calibrate the distance of the broken tips of the MCBJs and estimated as follows: In Fig. 3.3 an SEM image of a bridge viewed under an angle of 45° is shown. The funnel shaped ridge in the polyimide (PI) indicates that the bridge is freestanding. It can be prolonged until it crosses an imaginary horizontal line going through the center of the junction as indicated by the white lines in the figure. Evidently this method is not very accurate, hence a measurement error of ~ 250 nm is assumed.

[6] methylisobutylketone

[7] Either one of these can be used as control parameter for RIE—most reproducible results are achieved when the DC–bias is controlled. Note, a deviation of only 4 % of the DC–bias already leads to differences in the etching process that can be seen in the SEM images of the samples.

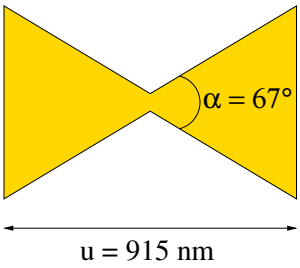

Figure 3.2: *Geometry of the bridge, top view. The opening angle of the tips is* $\alpha = (67 \pm 2)°$ *and the freestanding length of the bridge is* $u \approx (915 \pm 300)$ *nm.*

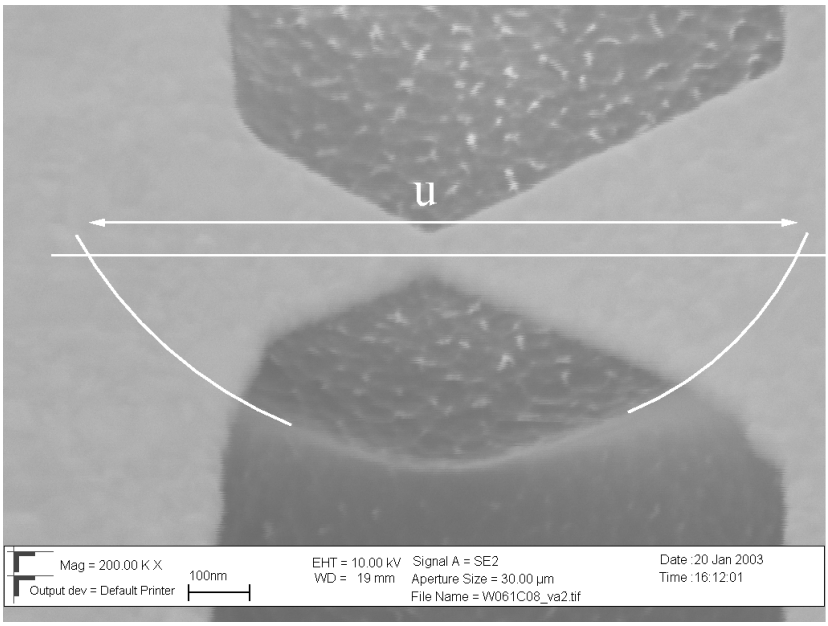

Figure 3.3: *Measuring the length of the bridge. This is an SEM image viewed under an angle of 45°. Horizontal distances can be measured directly. The funnel shaped ridge of the PI underneath the bridge is prolonged by visual judgment until it intersects a horizontal line going through the center of the bridge.*

There are indications that the bridge is actually longer than measured in this way. In rare cases, the gold is totally removed from the bridge region by a strong static discharge. An SEM image of such a bridge is shown in Fig. 3.4. By applying the same measurement algorithm to the remains of such a sample, it can be estimated that the bridge is about 1.3 times longer than the value measured by our standard technique. This has been performed for only two samples, thus the result must be taken cum grano salis. In our calculations we will use the bridge length evaluated as described in Fig. 3.3 times 1.3. An evaluation of 20 samples yields (including the factor of 1.3) a freestanding length of the bridge of $u \approx (915 \pm 300)$ nm. The thickness of the gold layer is (50 ± 15) nm.

The dimensions of the leads are needed to calculate the thermal properties of the samples. They can be divided into three parts, according to their width, and the pads which are located near the edge of the sample:

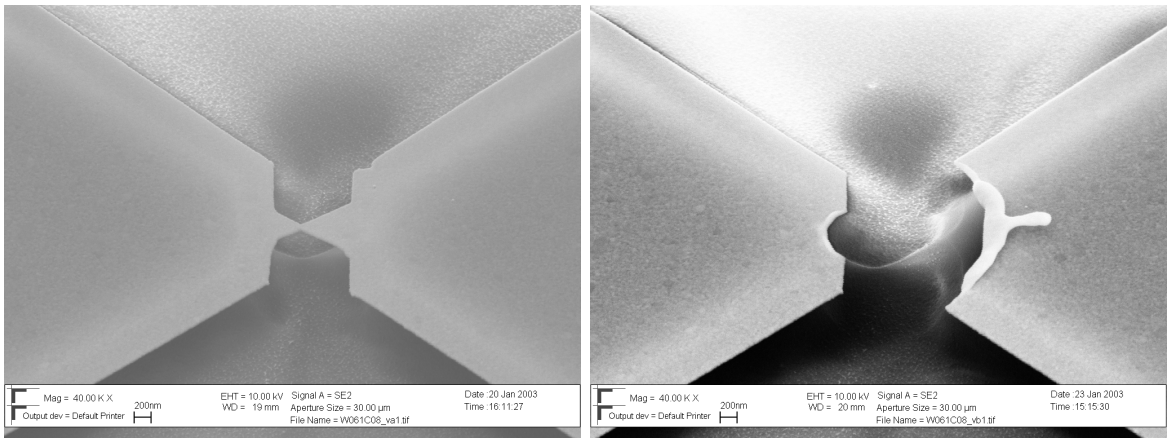

Figure 3.4: *Two SEM images of the same junction before (left) and after (right) a static discharge. In the right hand side image, the bare PI is visible. Assuming, that its form has not changed during the discharge process, this image can be used to estimate if the measurement procedure applied in fig 3.3 yields correct results.*

1. inner part, 10 μm wide, 100 μm long in total.
2. middle part, 20 μm wide, 2 mm long on each side.
3. outer part, 100 μm wide, 10 mm long on each side.
4. pads. Each pad has a surface of roughly 1 mm^2.

SEM images of the leads are presented in Figs. 3.5 and 3.6.

3.1.3 Electrical Resistance

The electrical resistance of the constriction can be estimated according to Maxwell's Formula [88] if the mean free path l for electrons is smaller than the radius a of the constriction. For our samples, $a \approx 30$ nm and according to Erts et al. [88], $l \approx 4$ nm, much less than the room temperature bulk gold value of 37 nm. Hence, Maxwell's formula can be used as approximation to calculate the resistance of the constriction:

$$R_{\text{constriction}} = \frac{\rho}{2a} = \frac{2.2 \cdot 10^{-8}}{2 \cdot 30 \cdot 10^{-9}}\ \Omega \approx 0,4\ \Omega \quad , \tag{3.1}$$

where $\rho = 2,2 \cdot 10^{-8}$ Ωm is the electrical resistivity of gold [89]. $R_{\text{constriction}}$ is much smaller than the electrical resistance of the entire sample $R = 230 \pm 50\ \Omega$, evaluated from 20 samples.

3.1.4 Thermal Resistance

By applying light to the contact or simply by Joule heating of the measuring current, the junction will heat up. To estimate how much the temperature rises, we now estimate the thermal resistance from the bridge to the steel plate. The latter will later be treated as cold heat reservoir because it is too large to be heated up by the weak heating power in our experiments. The heat flow will take place parallelly to the sample surface along the gold

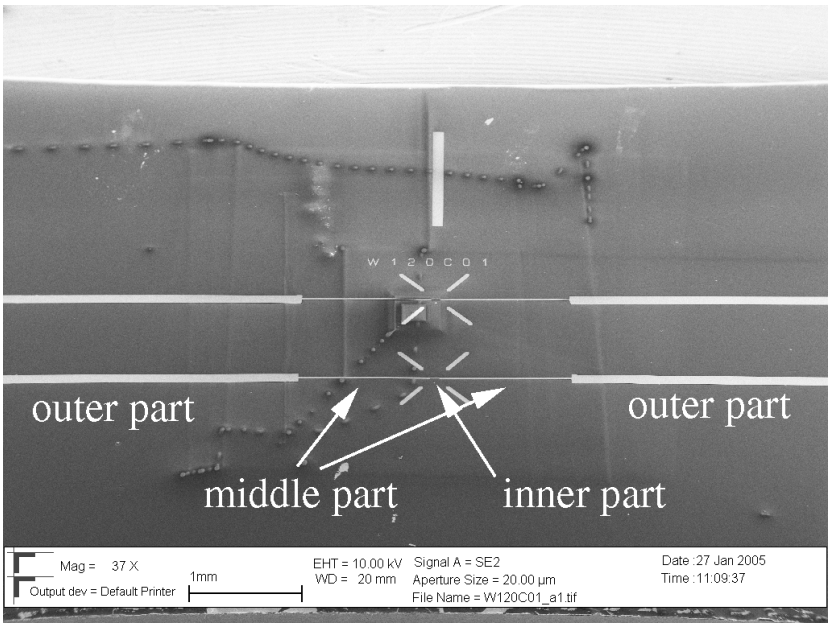

Figure 3.5: *Overview SEM image of a break junction sample. The outer, middle, and inner parts of the leads are indicated. The four lines building a cross are used for aiming when the junction is exposed to light. On each sample, two junctions are structured for redundancy purposes. Only one of them is used during measurement. The number (W120C01) indicates the sample–id.*

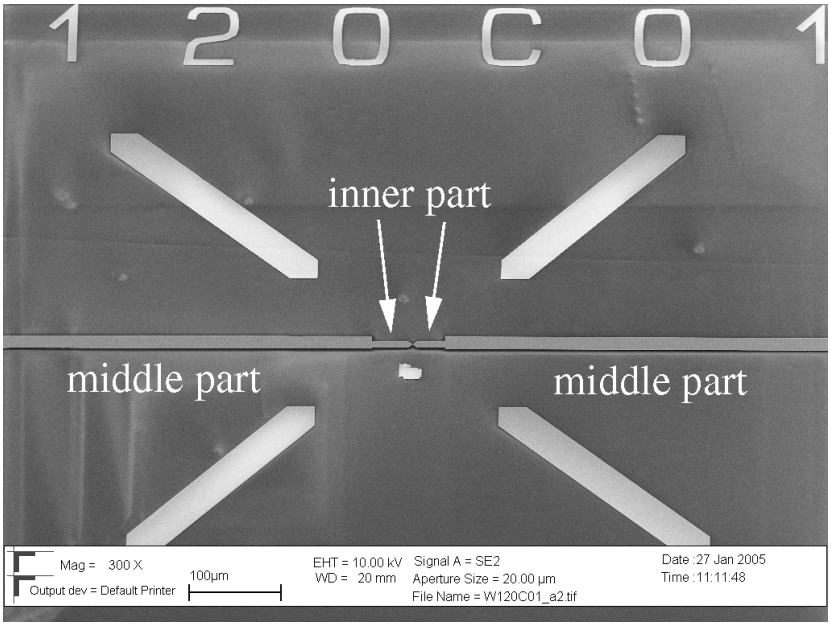

Figure 3.6: *Closer view at the center of Fig. 3.5. The dark line beneath the lead is a shadow from the underetched gold.*

leads and at the same time perpendicularly down to the substrate, see Fig. 3.7. The thermal

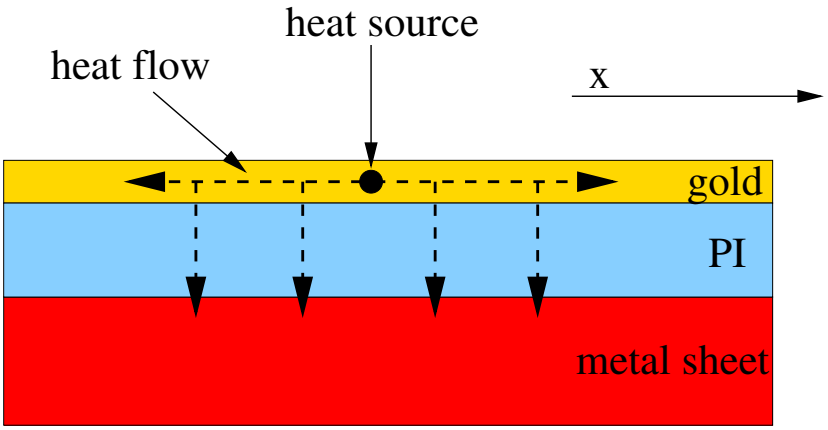

Figure 3.7: *Heat transport on a MCBJ sample. Heat generated in the gold lead will flow via the gold and at the same time downwards to the substrate.*

resistance of the gold lead increases with the transport distance Δx, while the contact area between gold and the substrate increases. Hence, the thermal resistance to the substrate decreases with Δx. There will be a transport distance x_0 for which the thermal resistance along the gold lead and perpendicular to it will be equal. We denote x_0 by *parallel heat transport length*. At distances $x \gg x_0$ from the heat source, the temperature of the gold and the substrate will be approximately equal.
To estimate the thermal resistance we have to discern between two possible approximations according to the lateral dimension D of the heat source.

1. *Local heating:* the heat source is well localized ($D \ll x_0$), for example, by Joule heating of the measuring current. Heat will flow away from the heated spot in all directions.

2. *Heating over a very broad region:* When a very large area is heated ($D \gg x_0$), there will be almost no lateral variation of temperature for $|x| < \frac{D}{2}$ and heat flow will predominantly take place perpendicular to the surface. This applies when illuminating the junction with a large focus.

Case 1: the bridge is locally heated

When the heated region is small compared to the parallel heat transport length ($D \ll x_0$), the heat will flow parallelly along the gold lead and perpendicularly down to the substrate. As a simplified model, the heat transport can be described by the equivalent circuit diagram depicted in Fig. 3.8. For a given lateral distance Δx, the parallel resistance is given by (cf. eq. (2.17) on page 19)

$$R_{\parallel} = \frac{\Delta x}{\lambda_{\text{gold}} \cdot w \cdot h} \quad , \tag{3.2}$$

where $\lambda_{\text{gold}} = 400\ \frac{\text{W}}{\text{K}}$ is the thermal conductivity of gold, w the width of the leads, and h their thickness. The contact area to the substrate is $A = w \cdot \Delta x$. The perpendicular resistance is given by the sum of the contact resistance and the resistance of the PI layer.

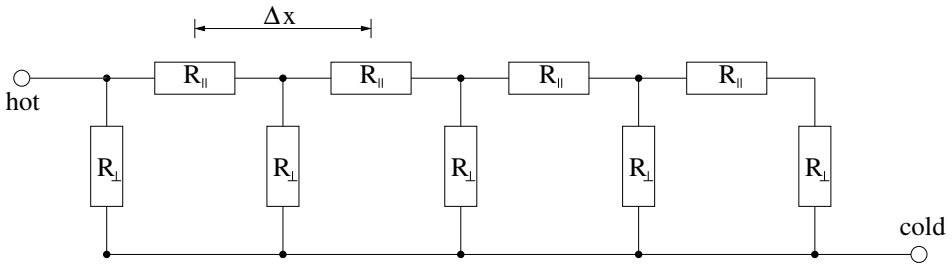

Figure 3.8: *Network of thermal resistances describing the thermal conduction from the heat source (hot) to the cold substrate. $R_\parallel$ symbolizes parallel, $R_\perp$ perpendicular thermal resistance. The sample is divided into several sections of length Δx. In the limit of small Δx, the total thermal resistance can be calculated recursively.*

$$\begin{aligned} R_\perp &= \frac{\hat{R}}{w\cdot\Delta x} + \frac{d}{\lambda_{\mathrm{PI}}\cdot w\cdot\Delta x} \\ &= \frac{1}{w\cdot\Delta x}\cdot(\hat{R} + \frac{d}{\lambda_{\mathrm{PI}}}) \end{aligned} \tag{3.3}$$

$d \approx 4\ \mu$m is the thickness of the PI layer and $\lambda_{\mathrm{PI}} = 0.22\ \frac{\mathrm{W}}{\mathrm{K}}$ the thermal conductivity, hence $\frac{d}{\lambda_{\mathrm{PI}}} = 1.8\cdot 10^{-5}\ \frac{\mathrm{K\cdot m^2}}{\mathrm{W}}$. The specific thermal contact resistance $\hat{R}$ from the gold to the PI and then to the substrate is difficult to predict. Instead, it is best to find a similar structure of which the specific resistance has been measured. In [83], a value for a [Si / 20 μm Epoxy / AL] structure is given: $5\cdot 10^{-5}\ \frac{\mathrm{K\cdot m^2}}{\mathrm{W}}$. This value was obtained from an industrially produced sample where heat transport was an important issue. We assume that the specific resistance of our sample is larger but of similar magnitude, hence we will use $\hat{R} = 5\cdot 10^{-5}\ \frac{\mathrm{K\cdot m^2}}{\mathrm{W}}$ in our calculations and interpret the results as lower bound. The thermal resistance perpendicular to the sample is then given by

$$R_\perp \approx \frac{1}{w\cdot\Delta x}\cdot(5\cdot 10^{-5}\ \frac{\mathrm{K\cdot m^2}}{\mathrm{W}}) \quad . \tag{3.4}$$

By setting $R_\perp = R_\parallel$ from eq. (3.4) and eq. (3.2) we can deduce x_0

$$x_0 = \sqrt{\lambda_{\mathrm{gold}}\cdot h\cdot\hat{R}} \tag{3.5}$$

and calculate a first estimate of the thermal resistance

$$R \approx \frac{1}{2}\cdot\frac{1}{2}R_\perp(x_0) = \frac{1}{4w}\cdot\sqrt{\frac{\hat{R}}{\lambda_{\mathrm{gold}}\cdot h}} \quad , \tag{3.6}$$

where the first factor of $\frac{1}{2}$ reflects the parallel transport through $R_\parallel$ and $R_\perp$ and the second factor of $\frac{1}{2}$ reflects that the heat can flow in positive and negative x-direction. For the inner part of the leads ($w = 10\ \mu$m) and $\hat{R} = 5\cdot 10^{-5}\ \frac{\mathrm{K\cdot m^2}}{\mathrm{W}}$ we obtain for x_0 and R:

$$x_0 \approx 32\ \mu\mathrm{m} \qquad \text{and} \qquad R \approx 4.0\cdot 10^4\ \frac{\mathrm{K}}{\mathrm{W}} \quad . \tag{3.7}$$

A more accurate value for R can be calculated recursively for $\Delta x \ll x_0$ using the equivalent circuit diagram shown in Fig. 3.8 but differs only by a few percent from the value given in eq. (3.7).

Case 2: the sample is heated over a very broad region

When the lateral dimension of the heat source is larger than the parallel heat transport length ($D \gg x_0$), the lateral heat distribution along the sample surface will be relatively homogeneous. Heat will predominantly be transported downwards through the PI but not in parallel along the gold lead. The thermal resistance R for a contact area A is then given by

$$R \approx \frac{\hat{R}}{A} \tag{3.8}$$

with $\hat{R} \approx 5 \cdot 10^{-5}\ \frac{\mathrm{K \cdot m^2}}{\mathrm{W}}$ as above.

3.2 Molecules

The molecules used for our experiments are specially designed to meet the requirements for the MCBJ technique. All molecules are rod-like acetyl protected dithiols:

$$\underbrace{\mathrm{H_3COC}}_{\text{acetyl group}} - \mathrm{S} - \mathrm{R} - \mathrm{S} - \underbrace{\mathrm{COCH_3}}_{\text{acetyl group}}$$

having different central parts R.

Principle to build the molecular contact

We want to measure the electron transport properties of a metal–molecule–metal contact comprising a few or at best only a single molecule. For this task we need metal electrodes which do not rapidly oxidize and molecules which can be attached to these in a stable manner. We chose gold as electrode material and acetyl protected sulfur groups as molecular end groups. The acetyl group is cleaved in situ upon contact with the gold surface and replaced with a stable covalent bond between the sulfur atom and the gold. With this type of molecules, self-assembled monolayers (SAMs) on gold can be obtained [90–92].
The reaction to form the S–Au bond from the acetyl protected thiol is believed to require traces of water [91]. These are always present even in vacuum except if great care is taken to remove them [93, 94]. In contrast to the direct reaction of free thiols (SH terminal groups), the bond formation from the acetyl protected sulfur groups is very slow. Hence, to obtain a relatively low coverage of molecules on the gold surface, we (i) use a very dilute molecule solution, and (ii) keep the reaction time very short and thoroughly rinse the sample to remove unbound molecules. This procedure is described in further detail below in section 3.5. The acetyl protection groups have an additional advantage: Free thiols are prone to oxidation forming disulfides in the presence of even traces of oxygen. In contrast, acetyl-protected thiols are stable, facilitating their handling.

3.2.1 Tunneling Barrier Molecule

In preceeding experiments, it has been noted [8,28,87] that the contacts between the molecule and the metal electrodes, which presumably act as the main barrier for electronic transport, significantly influence the electronic transport properties of the metal–molecule–metal junction. Hence, it was sought to design a molecule where the barrier governing electronic transport lies within the molecule. This can be achieved by reducing the electronic overlap between

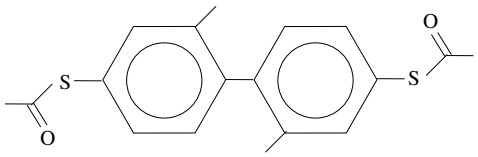

Figure 3.9: *4,4-Bis(acetylsulfanyl)-2,2'-dimethyl-biphenyl. This molecule and its derivative without acetyl protection groups will be abbreviated as* "biphenyl molecule".

neighboring phenyl-rings in the molecule. An example of such a molecule, synthesized by M. Elbing (INT[8]) [2, 95] in the group of M. Mayor, is shown in Fig. 3.9. Here, the phenyl-rings are tilted out of the plane due to steric strain induced by the methyl-groups in position 2 of the phenyl-rings decreasing the overlap between their p_z-orbitals. In this work, this molecule and its derivatives without acetyl groups will be addressed as *biphenyl molecule*.

Single crystals of the biphenyl molecule that were suitable for X-ray analysis were grown by slow diffusion of hexane into a solution of diethylether. From the crystal structure the angle between the two phenyl-rings was determined to $(79.7 \pm 0.2)°$. The length along the molecular axis as defined by the distance between the two sulfur atoms was measured to (1.06 ± 0.02) nm.

A contact comprising the biphenyl molecule will probably have three weak links: the S–Au contacts on either side and the barrier in the middle of the molecule due to the weak overlap of the π-electron systems of the phenyl-rings. If the central barrier dominates the transport properties of the metal–molecule–metal contact, then its current–voltage characteristic (IV) should resemble that expected for a tunneling contact. This behavior has actually been observed in measurements done by M. Di Leo [96] at low and room temperatures. Room temperature data recorded in this work confirm these results. This is an indication that the idea to position the "main" barrier inside the molecule seems to work.

3.2.2 Anthracene Island Molecule

To study the influence of light on the electron transport properties, a molecule bearing a central anthracene moiety as chromophore has been designed and synthesized by M. Elbing and M. Mayor at the INT (Fig. 3.10). The anthracene ring is substituted symmetrically in position 9 and 10 by a phenyl-ring having a methyl-group in ortho-position and an acetyl-protected sulphur in position 4. In similarity to the biphenyl molecule steric hindrance will result in a tilt of the phenyl-rings out of the plane of the anthracene core. Thereby, the chromophore will be decoupled electronically from the outer parts of the molecule. Since the sulfur-groups on both outer parts are used to bind to the gold electrodes in the MCBJ, the anthracene will be decoupled from the electrodes as well. We will address this molecule and its derivative without protection groups as the *anthracene molecule*.

Fig. 3.11 shows the absorption spectrum of the anthracene molecule recorded at room temperature ($5 \cdot 10^{-6}$ M solution in hexane). The longest wavelength absorption in the visible region slightly below 400 nm can be attributed to the anthracene moiety [2].

[8]Institute of Nanotechnology

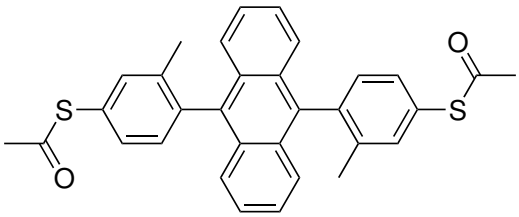

Figure 3.10: *9,10-Bis(4-(acetylsulfanyl)2-methyl-phenyl)-anthracene. The optical absorption spectrum of the molecule in solution is shown in Fig. 3.11. This molecule and its derivative without acetyl protection groups will be abbreviated as* "anthracene molecule"*.*

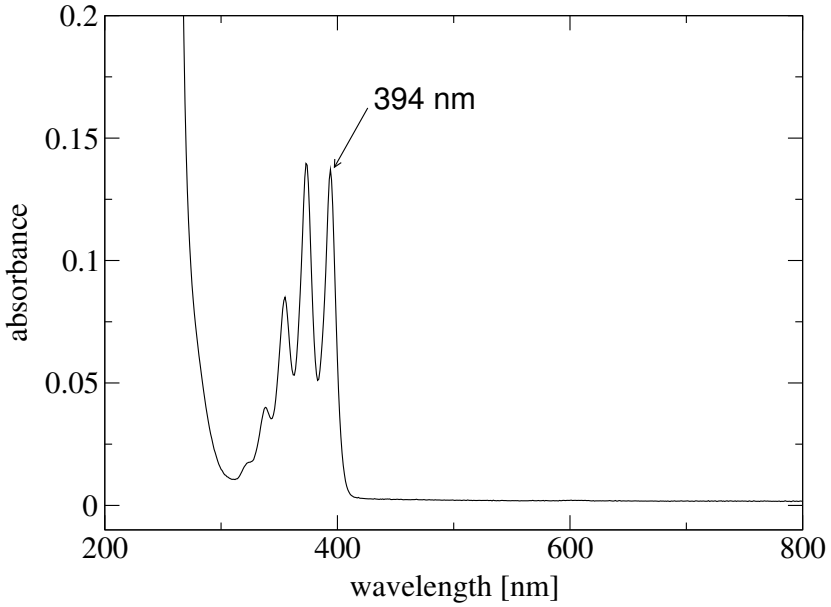

Figure 3.11: *Absorption spectrum of 9,10-Bis(4-(acetylsulfanyl)2-methyl-phenyl)-anthracene ($5 \cdot 10^{-6}$ M solution in hexane at room temperature). The absorbance A is defined as $A = \log_{10} \frac{I_0}{I}$, where I_0 is the intensity after transmission through pure solvent and I the intensity after transmitting the solution containing the molecule.*

Up to now, no single crystal of this compound suitable for X-ray analysis could be obtained. By comparing the molecule with other molecules where X-ray data from single crystals was accessible[9], we assume a distance between the sulphur atoms of 1.5 nm.

3.2.3 Asymmetric Molecule

The asymmetric molecule has been designed based on a concept for a molecular diode proposed by Aviram and Ratner in 1974 [97]. This molecular diode consists of an electron donor, an electron acceptor, and in a tunneling barrier between them. The onset of the current of an Aviram–Ratner diode depends strongly on the bias direction.
The structure of the asymmetric molecule is presented in Fig. 3.12. The internal tunneling barrier is again realized by steric hindrance, leading to a strong reduction of the coupling

[9]These are similar molecules where the central moiety are one or two phenyl-rings [2].

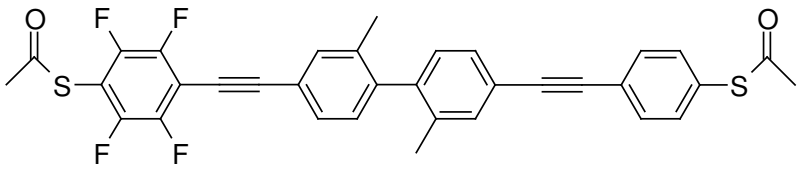

Figure 3.12: *Molecular structure of 4'-(4-Acetylsulfanyl-phenylethynyl)-4-(4-acetylsulfanyl-2,3,5,6-tetrafluoro-phenylethynyl)-2,2'-dimethyl-biphenyl. An internal tunneling barrier is realized by steric hindrance dividing the molecule in two electronically different parts. Due to the fluoro-substituents, the energy levels of the electronic orbitals of the left-hand side lie lower than on the right-hand side [43, 98]. In this work, we will address this molecule and its derivative without acetyl groups by the abbreviation* "asymmetric molecule".

between π-electron systems left and right of the barrier. We will address this molecule and its derivative without protection groups by the abbreviation *"asymmetric molecule"*. Current–voltage characteristics of the asymmetric molecule recorded in this work and by R. Ochs [2, 43, 98, 99] are always asymmetric with respect to voltage inversion.

It was possible to obtain single crystals of a derivative of the asymmetric molecule bearing different protection groups on the sulphur. The tilt angle between the central phenyl-rings in the solid state was measured to $(75.0 \pm 0.8)^\circ$ nm, while the two different phenyl-ethinyl subunits on either side are almost coplanar. The distance from sulphur to sulphur atom is (2.43 ± 0.04) nm. The main feature of this molecule used in this work was its ability to lead to asymmetric IVs when contacted by mechanically-controlled break-junctions.

3.2.4 Ruthenium Complex Molecule

This molecule was synthesized by A. Landa in the group of M. Ruben at the INT. In this species Ru(II)[10] is surrounded by two terpyridine units forming an organo–metallic complex. The central ring of both terpyridines is substituted further in position 4' by a phenyl-ethinyl-subunit bearing an acetyl-protected sulphur group in position 4 of the phenyl-ring. Hence, this complex consists of two conjugated π-systems that are separated by the Ru-ion. Again the sulphur will be used to bind the molecule to the gold leads.

The structure of this compound as it is found in a single crystal is shown in fig 3.13. The nitrogen atoms are depicted in blue, the sulfur atoms in yellow and the Ru as well as the oxygen in red. The apparent bending of the molecule presumably results from packing effects in the solid state. We assume that the molecule does not exhibit this bend in solution. The length of the molecule defined by the sulfur–sulfur distance was determined to 2.7 nm. As the complex is charged, in solution the counter-ion PF_6^- is present. In this work, we will address the molecule and its derivative without acetyl protection groups as *"Ru–complex"*. It was designed for optical experiments and absorbs light in the visible region. In solution, it shows an absorbance peak at 499 nm with a FWHM[11] of 20 nm. Electronic transport measurements of such a type of molecule (ionic metal-organic complex) in a MCBJ setup have not been carried out so far.

[10] This denotes a twice positively charged Ru-ion in embedded a molecular complex.
[11] full width at half maximum

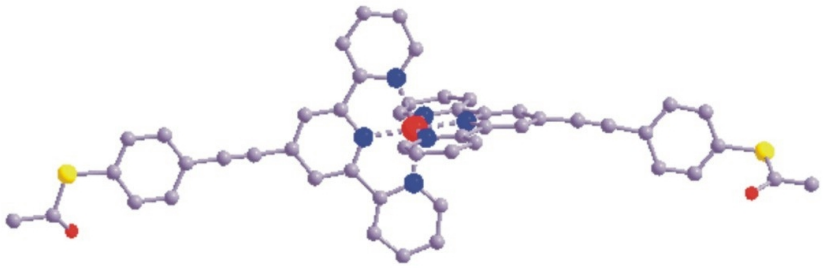

Figure 3.13: *Molecular structure of Bis-[(thioacetic acid S-(4-[2,2';6',2"]terpyridin-4'-ylethynyl-phenyl) ester]-Ruthenium (II) dihexaflouro phosphate obtained by X-ray analysis. The nitrogen atoms are depicted in blue, the sulfur atoms in yellow and the Ru as well as the oxygen in red. In this work, we will address this molecule and its derivative without acetyl protection groups as* "Ru-complex".

3.3 Measurement Setup

3.3.1 General Description

A photograph of the (closed) vacuum chamber is shown in Fig. 3.14: a suspended hollow steel cube with a glass viewport placed on top to illuminate the sample from above. The turbopump is directly attached to the right-hand side of the vacuum chamber to minimize the attainable base pressure. The pressure is measured on the opposite side to ensure the chamber pressure is not higher than the measured value. Below the chamber are the feed-throughs for the electrical cables and the turning axis of the motor which was used to bend the sample. The base pressure of the vacuum chamber was below $5 \cdot 10^{-7}$ mbar for experiments performed in Karlsruhe and in the upper 10^{-6} mbar range during the optical experiments in Würzburg. A close-up of the bending mechanics is shown in Fig. 3.15. The photograph shows an apparatus which is identical to the one used in this work, except that it is not equipped with a copper strand as a thermal conductor.

Electrical circuitry

The electrical contact to the MCBJ is mediated by narrow strips of copper adhesive tape which are wrapped around the counter supports. These are pressed against contact pads on the sample by the pressure exerted when the MCBJ is bent. The copper tape is indicated ("contacts") in Fig. 3.15. A resistance in series (1 kΩ, also annotated in the figure) reduces the current through the sample ($R_{\text{sample}} \approx 230\ \Omega$) prior to breaking. To apply a bias voltage and to measure the current, we use a Keithley 6430 Sub-Femtoamp SourceMeter.

Bending the sample: the stepping motor

To bend the sample, the pushing rod must be moved upwards with respect to the counter supports. This movement is performed via a long differential threaded rod[12] which is turned by a stepping motor mounted below the vacuum chamber. The pushing rod is firmly attached to a copper block (the "lower copper block") which itself is fixedly mounted in the vacuum chamber. The counter supports are fixed to the upper copper block (seen in Fig. 3.15) which

[12]The upper and lower part of the threaded rod have different threads.

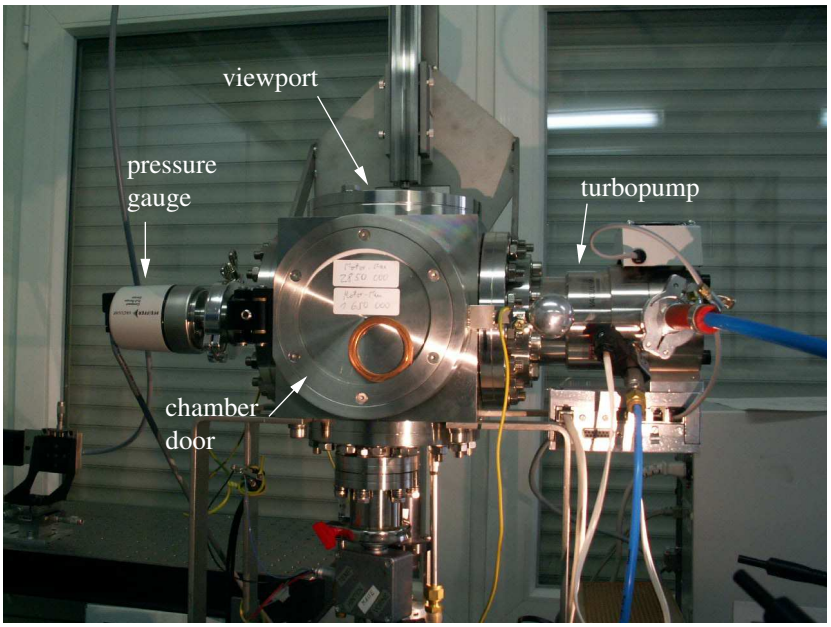

Figure 3.14: *Photograph of the vacuum chamber in which the molecules are contacted. The chamber is a hollow steel cube with the turbopump directly attached to achieve a low base pressure. The pressure gauge is situated on the opposite side to ensure the chamber pressure to be lower than the measured value. The top flange of the cube is a viewport to allow illumination of the sample.*

is mounted on three gliding poles and can move up and down. The threaded rod connects the two blocks. The thread in the upper block is M 3.5 (slope: 0.6 mm) while in the lower block it is only M 3 (slope: 0.5 mm). When the threaded rod is turned, the upper copper block moves with respect to the lower copper block by the difference of the slopes of the two threads, i.e. 0.1 mm per turn. In addition, the entire threaded rod moves up or down when turned (by the slope of the M 3 thread), thus it cannot be firmly attached to the motor axis. Instead, there must be a gliding connection between the motor axis and the threaded rod. This is provided by a metal transmission sheet which can glide up and down along the tips of a two-tip turning fork. The turning fork is fixed to the motor axis while the metal transmission sheet is fixed to the threaded rod. A schema of the mechanical transmission is presented in Fig. 3.16 and a photograph of the setup in Fig. 3.17. The angular resolution of the motor is 0.006°. Its actual position is denoted by *motor positions* and measured in "steps". Hence, one turn corresponds to approximately $\frac{360}{0.006} = 60\ 000$ steps. The exact value was measured to be (59652 ± 30) steps.

The movement of the counter supports ΔX is proportional to the motor movement ΔM. We define the proportionality factor ξ as: $\Delta X = \xi \cdot \Delta M$. Turning the threaded rod by 360° corresponds to moving the counter supports by $\Delta X = 0.1$ mm. Hence,

$$\xi = \frac{0.1 \text{ mm}}{59652 \text{ steps}} = (1.6764 \pm 0.0008) \cdot 10^{-9} \frac{\text{m}}{\text{step}} \tag{3.9}$$

The zero position $M = 0$ of the motor is defined as the position of maximum bending of the setup. When a sample is mounted, the motor position has to be *reduced* ($\Delta M < 0$) to increase

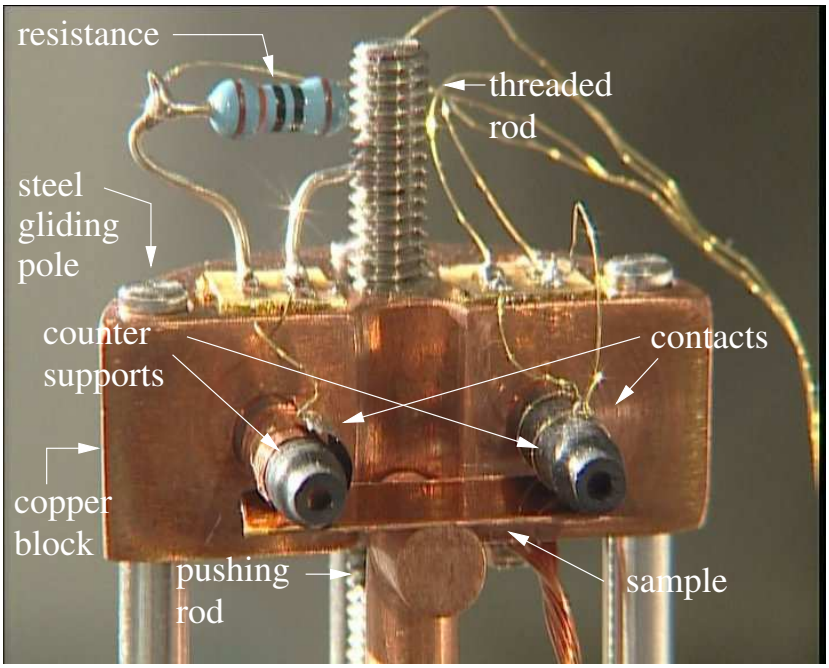

Figure 3.15: *Photograph of the three-point bending mechanism (close-up view). Turning the threaded rod moves the whole copper block including the counter supports downwards. The pushing rod is fixed on the lower copper block, thus the sample is bent. The bending mechanism shown is identical to the one used in this thesis without copper strand. The series resistance (1 kΩ in this work) is to protect the sample from currents that are too high, prior to breaking. The contacts are made of copper adhesive tape. Heat shrinkable tubing electrically isolates them from the upper copper block. In this work only one contact on the right-hand side is used, because only one junction on the sample is contacted.*

the bending angle of the sample and *increased* ($\Delta M > 0$) to reduce the bending angle. Hence $\Delta M < 0$ corresponds to *enlarging the gap* between the break-junction electrodes and $\Delta M > 0$ to *narrowing the gap*. Due to the definition of the zero position, the motor position values M are always positive.

3.3.2 Mechanical Hysteresis

Hysteresis effects of the mechanical turning setup prevent a one-to-one correspondence between the motor position readout and the movement of the counter supports. In order to interpret data measured as function of the electrode spacing, it is favorable to quantify the amplitude of this hysteresis. In addition, the question is important whether the hysteresis can be corrected for.

How the hysteresis can be measured

Consider a given distance of the break junction tips at a motor position M_1. This distance corresponds to a fixed tunnel conductance G_0 of the junction. Now, the electrode distance can be reduced while measuring the conductance of the junction. When a pre-defined maximum conductance is reached, the motor motion is reversed. The electrode gap will enlarge, reducing

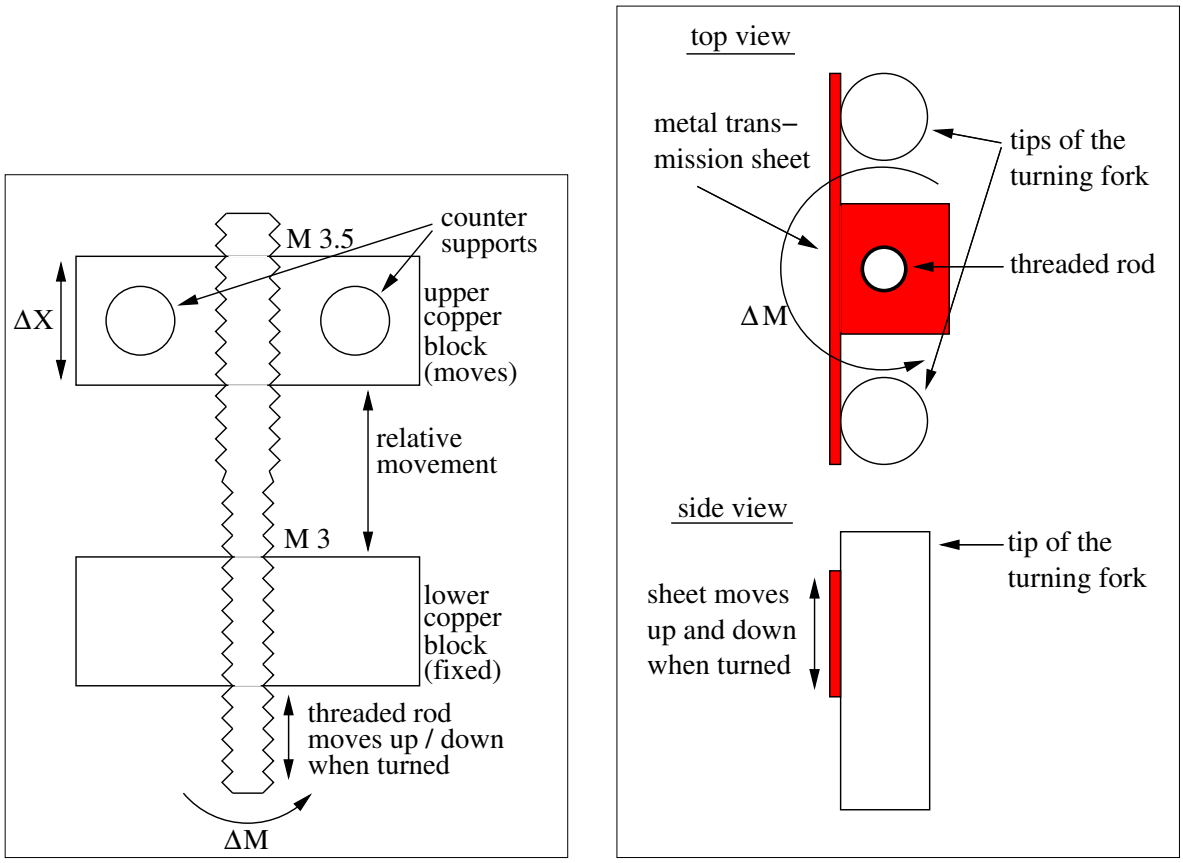

principle of the differential thread | metal transmission sheet

Figure 3.16: *Transmission of the motor movement into the movement of the counter supports. Left-hand side: a long threaded rod connects the upper with the lower (fixed) copper block. The thread in the upper block is M 3.5 (slope: 0.6 mm) while in the lower block it is only M 3 (slope: 0.5 mm). When the threaded rod is turned (denoted by ΔM), the upper copper block moves with respect to the lower copper block by the difference of the slopes of the two threads, i.e. 0.1 mm per turn (denoted by ΔX). When turned, the entire rod moves up or down, thus there has to be a gliding element in the transmission of the rotation motion from the motor to the threaded rod (see right-hand side). This is provided by a metal transmission sheet which can glide up an down along the tips of a turning fork. The turning fork is fixed to the motor axis while the metal transmission sheet is fixed to the threaded rod. A photograph of the entire setup, where the turning fork and the metal transmission sheet are visible, is shown in Fig. 3.17*

the conductance until again the conductance G_0 is reached at a motor position M_2. The difference between the motor positions M_2 and M_1 is—in this work—denoted as *mechanical hysteresis*, see Fig. 3.18. The cycle just described is measured consecutively several times for each sample. An example for measuring the mechanical hysteresis using tunnel currents is shown in Fig. 3.19. The mechanical hysteresis of 13 samples measured by this method is presented as black circles in Fig. 3.20.
The contributions to the mechanical hysteresis stemming from the bending mechanics alone can be measured visually by reversing the motion of the motor and measuring the number

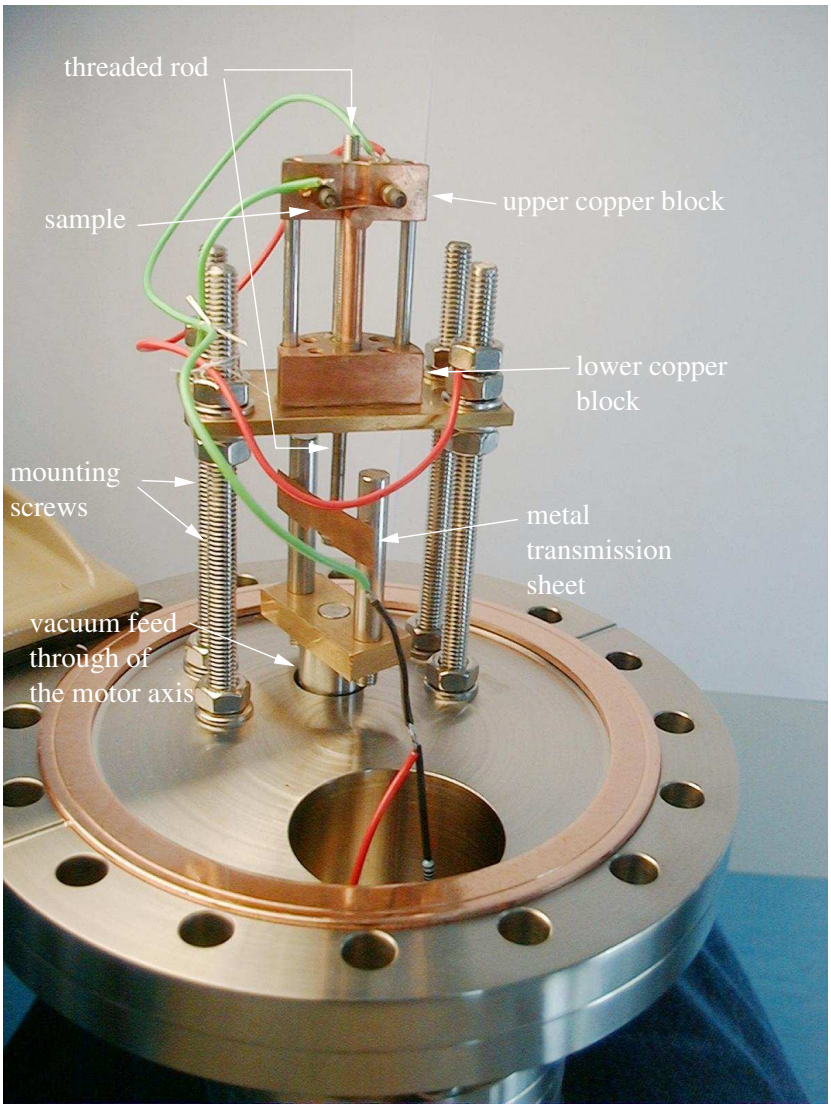

Figure 3.17: *Photograph of the entire bending mechanism. The lower copper block is fixed to a brass plate which is mounted on four screws emanating from the flange. The space below the brass plate is needed by the metal transmission sheet which moves up and down when the threaded rod is turned. The flange is mounted from below into the vacuum chamber shown in fig 3.14. This photograph was taken before the cooling mechanism described in section 3.3.3 was installed.*

of steps until the threaded rod begins to turn again. This measurement as a function of the turning angle of the rod is presented in Fig. 3.20, denoted by "visual gaging". This contribution is independent of the tension in the mechanical setup as it does not depend on the total motor position M at which it was measured, see Fig. 3.21. As can be seen in Fig. 3.20, there are additional contributions to the total mechanical hysteresis.

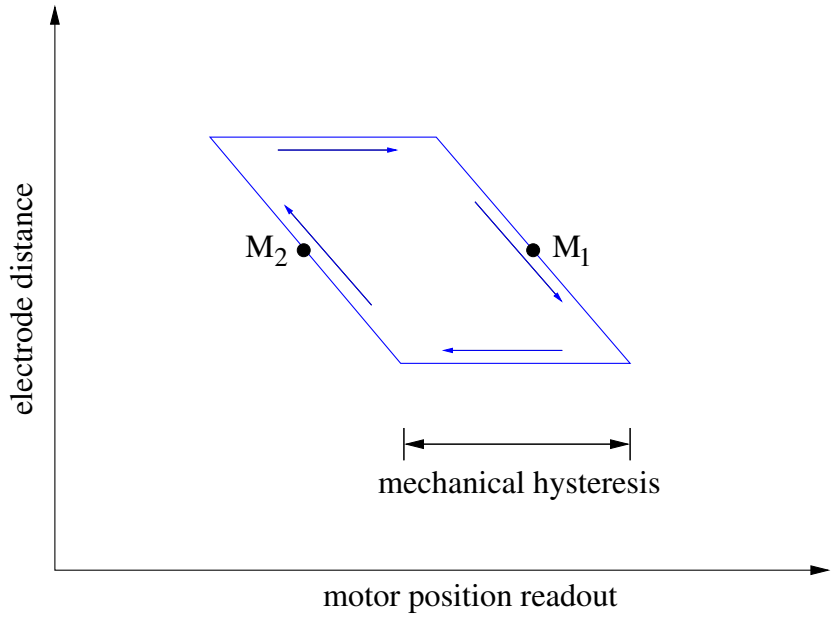

Figure 3.18: *The cycle to measure the mechanical hysteresis. The junction is repeatedly closed and opened while measuring the junction conductance at small bias. The backlash of the motor, the mechanics and the sample lead to a hysteresis which can be clearly seen in the conductance curves. This type of measurement was performed for all samples.*

Can the mechanical hysteresis be corrected?

An important contribution to the mechanical hysteresis stems from the backlash of the metal transmission sheet originating from a respective shift between the axes of the threaded rod and the turning fork, see Fig. 3.22. This leads to a gap between the fork and the transmission sheet and is confirmed by fitting the visually measured data in Fig. 3.20. The fitted dependence is:

$$\Delta M(\varphi) = 1.97 + 1.28 \cdot \sin(2.95 + \varphi) \quad , \tag{3.10}$$

where φ is the angle of the transmission sheet (see Fig. 3.22) and ΔM is the backlash at this angle. Hence, the mechanical hysteresis can partially be corrected using eq. (3.10).

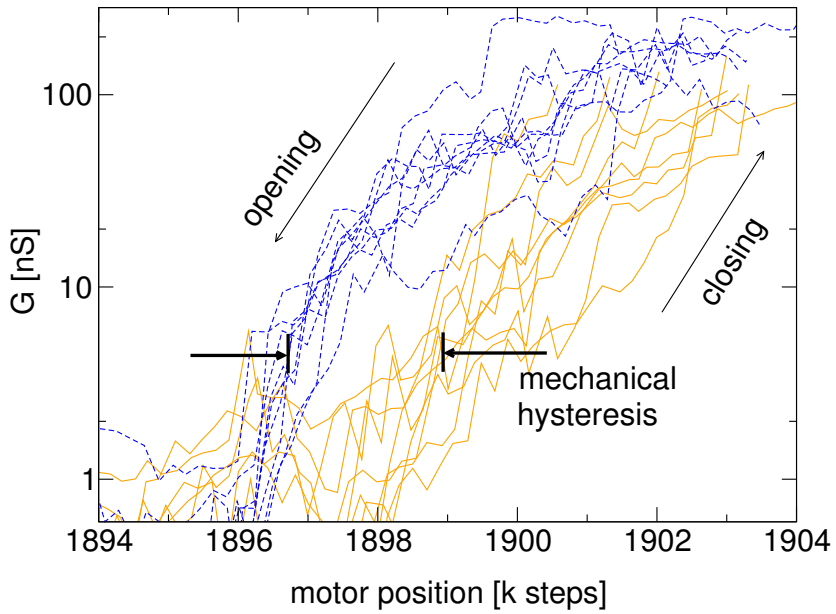

Figure 3.19: *Tunnel conductance measurement to evaluate the mechanical hysteresis. At a bias of 10 mV the junction is closed (solid orange lines) until a maximum current is reached and then opened (dashed blue lines) until no current is detectable. This cycle is repeated many times. Here, nine consecutive sweeps are displayed. The shift between the conductance curves measured while opening or closing the junction is the mechanical hysteresis of the junction. Sample-id: W132C27S2.*

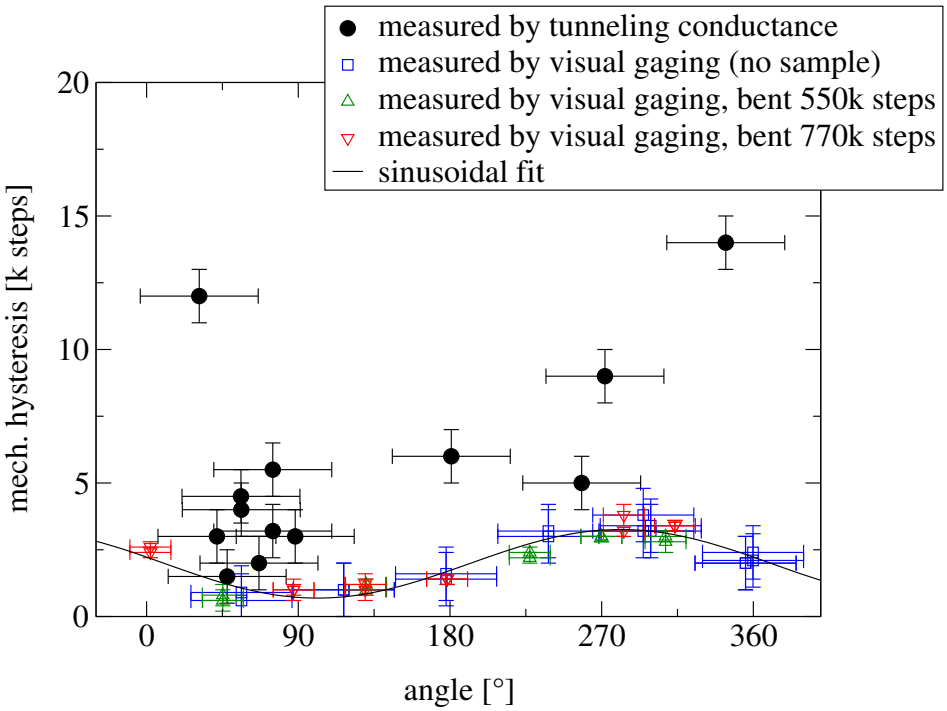

Figure 3.20: *Mechanical hysteresis of 13 samples measured using tunneling conductance curves (black dots). The backlash of the metal transmission sheet measured by visual gaging for no, weak, and strong tension in the setup is also presented. The backlash can be fitted by a sinusoidal curve, presented as black line:* $\Delta M(\varphi) = 1.97 + 1.28 \cdot \sin(2.95 + \varphi)$.

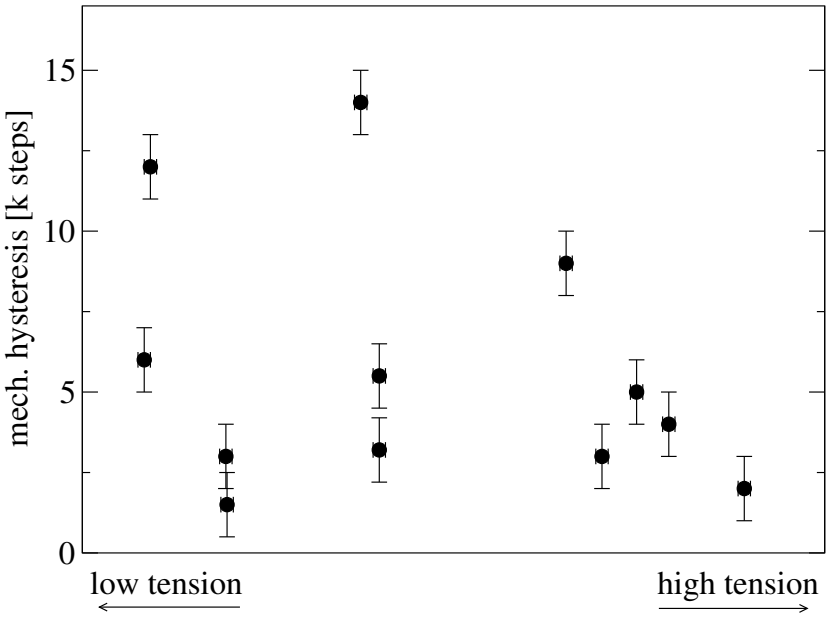

Figure 3.21: *Mechanical hysteresis of 12 samples as a function of the tension in the mechanical setup. The mechanical hysteresis was measured using tunneling currents. The hysteresis apparently does not depend on how much the junction was opened to break the junction, i.e. the mechanical hysteresis shows no clear dependence on the stress in the bending mechanics.*

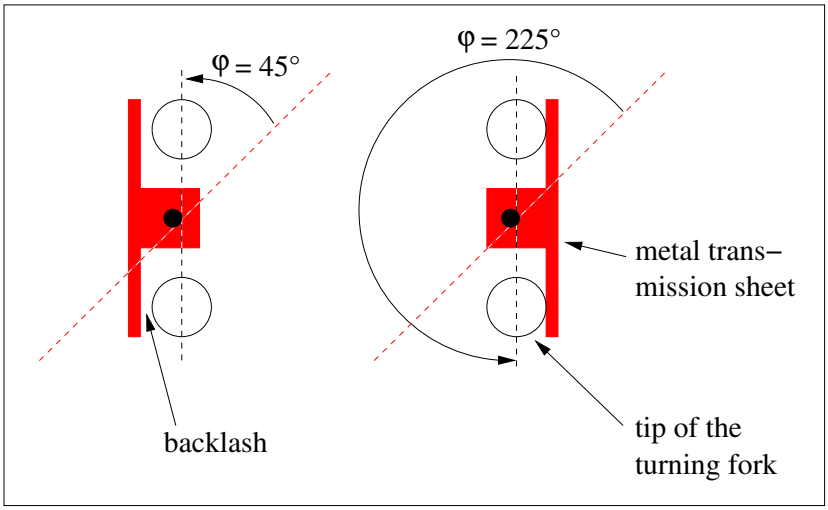

Figure 3.22: *Backlash of the metal transmission sheet. The axes of the turning fork and the threaded rod are slightly shifted. This leads to a backlash of the turning transmission between the fork and the transmission sheet which depends on the turning angle of the axis. The positions for* $\varphi = 45°$ *and* $\varphi = 225°$ *are shown,* $\varphi = 0$ *is the same angle as at zero motor position* $M \equiv 0$.

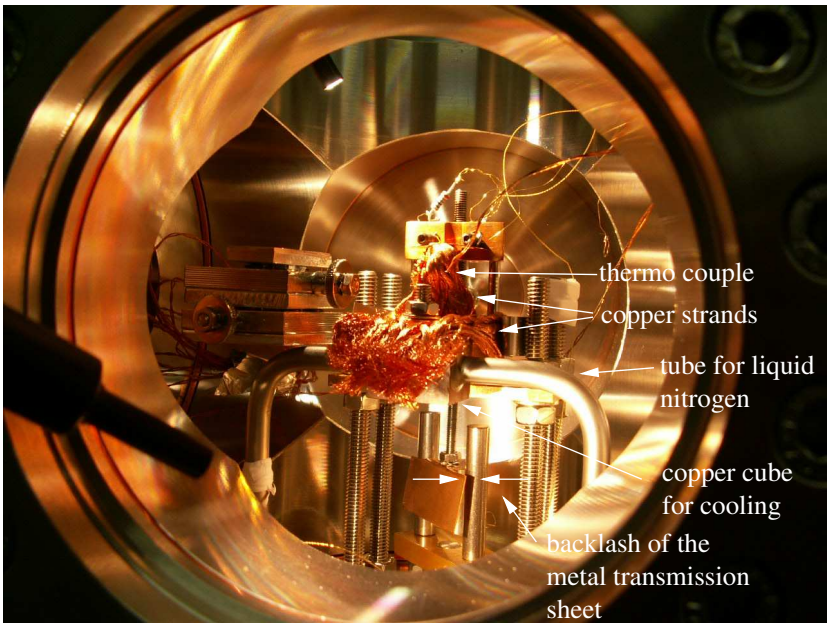

Figure 3.23: *Photograph of the bending mechanism used in this work. Between the turning fork from the vacuum feed-through of the motor and the metal transmission sheet, a small gap is visible. When the motor motion is reversed, this backlash contributes to the mechanical hysteresis but can be corrected by the formula given in eq. (3.10). The copper strands provide the thermal contact to a copper cube which can be cooled by a liquid nitrogen flow.*

3.3.3 Cooling Mechanism

The vacuum chamber is equipped with a crude cooling mechanism which is not intended for extensive use but rather to make preliminary cooling experiments. It consists of a copper cube of about $2 \times 2 \times 2$ cm^3 mounted inside the vacuum chamber which can be cooled by a liquid nitrogen flow, thereby providing a cold heat reservoir at a temperature of approximately 77 K. This cold spot is connected to the sample and to the *lower* copper block of the bending mechanism by two copper strands. They are indicated in Fig. 3.23. During the cooling, heat is transported into the system via the four threaded rods onto which the mechanical setup is mounted. In addition, the entire system reacts very slowly to temperature changes. Hence, it is difficult to accurately measure the sample temperature. The attainable sample temperature is roughly 140 K.

3.4 Optical Setup

In this section, we describe the setup used in this work to illuminate mechanically-controlled break-junctions. These experiments were conducted in collaboration with the group of Dr. Walter Pfeiffer in Würzburg[13] with a home-built Ti:sapphire ultrashort pulse laser system.

3.4.1 General Setup

For the optical measurements we illuminated MCBJs with laser light and recorded the current response of the junction. Several different light modes were available: ultrashort light pulses of 800 and 400 nm wavelength or 800 nm continuous wave (CW). For these measurements, the entire MCBJ apparatus was moved to Würzburg and attached to the laser table there. This way, the light could be guided accurately onto the MCBJ samples. The setup is schematically shown in Fig 3.24 and somewhat differs from the one used at the INT. The bias voltage was applied using a DAC-card of a computer and the current was measured using a current–voltage converter. This signal could directly be evaluated using a digital oscilloscope[14] or separated into a direct current (DC) and alternating current (AC) contribution using a lock–in amplifier[15]. In order to reduce vibrations to the point where the spot can be focused on the sample without any jitter interfering, the pump of the vacuum chamber was not fixed to the laser table. Instead, it was connected to the vacuum chamber by a one meter long tube. Thus the pressure for the optical measurements was only in the upper 10^{-6} mbar range.
To verify that we indeed illuminate the junction and not some other part of the sample, we looked at the diffraction pattern of the gold leads. This pattern can easily be seen on a piece of paper held above the window of the vacuum chamber. The spacing between the maxima of the pattern increases as the leads become thinner near the center of the sample. When the spot reaches the reticule (a cross like structure centered at the junction), the diffraction pattern changes completely. The reticule was structured onto the sample especially for this alignment process and can be seen in Fig. 3.5 on page 26. In this way we could also verify that the light-induced signal is only present when the junction itself is illuminated. No signals are found when the focus is aimed at the leads or any other part of the sample. The inclination angle of the light against the surface normal of the sample was 5°.

3.4.2 Illumination Parameters

The incident light power was controlled with a Pockels cell and chopped using an acousto–optical modulator (AOM) or a mechanical chopper wheel.
System parameters:

- Ti:sapphire laser, red: 800 nm (pulsed or CW) or blue: 400 nm (pulsed)
- pulse duration (FWHM, red): 50 fs
- repetition rate: 80 MHz
- average power during light-on periods: up to 20 mW (red) and 5 mW (blue).

[13] Physikalisches Institut, EP 1; Universität Würzburg; Am Hubland; D-97074 Würzburg
[14] LeCroy 9374 M, 500 MHz sampling rate.
[15] Stanford Research Systems, model SR830 DSP lock–in amplifier.

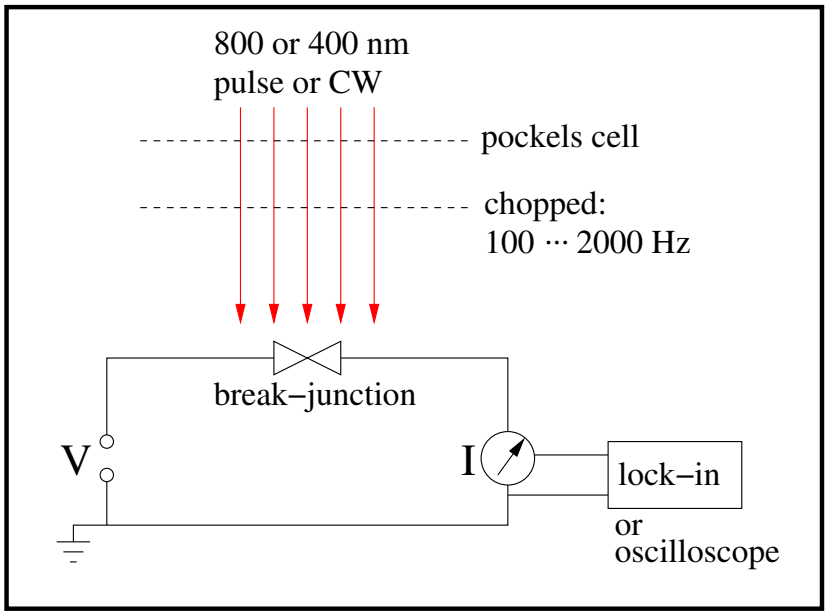

Figure 3.24: *Detection scheme of the setup used for the optical experiments. An DAC–card of a computer is used to apply the voltage to the contact and the current is measured with a current–voltage converter (IVC). The output of the IVC is optionally coupled into a lock–in amplifier or a digital oscilloscope. A titanium–sapphire laser was used as light source, supplying blue or red short light pulses or red CW light. The light intensity was controlled by a Pockels cell and modulated using either a mechanical chopper or an acousto–optical modulator (AOM).*

- diameter of the light focus (FWHM) determined by the knife-edge method: 110 μm (red) and 95 μm (blue)
- time averaged intensity during light-on periods of the chopper in the center of the focus, assuming a Gaussian beam profile: $4 \cdot 10^9 \ \frac{\mathrm{W}}{\mathrm{cm}^2}$ (red) and $1 \cdot 10^9 \ \frac{\mathrm{W}}{\mathrm{cm}^2}$ (blue)
- maximum intensity of a single pulse (red) assuming a Gaussian pulse envelope in time: $3 \cdot 10^{14} \ \frac{\mathrm{W}}{\mathrm{cm}^2}$
- chopper frequency: from 100 up to roughly 2000 Hz, most experiments at 314 Hz.
- DC current + lock-in amplifier $\Rightarrow$ we measured the DC current I and the light induced current change ΔI simultaneously.
- time constant of the lock–in amplifier: usually 5 to 10 times the period of the chopper frequency.

Note, the pulse duration did not change noticeably after passing through the viewport of the vacuum chamber.

Intensity in the center of a Gaussian beam profile

In the interpretation of our measurements, we assume a Gaussian beam profile of the light focus on the sample. We will now calculate the intensity N (given in $\frac{\mathrm{W}}{\mathrm{cm}^2}$ or $\frac{\mathrm{W}}{\mathrm{m}^2}$) in the

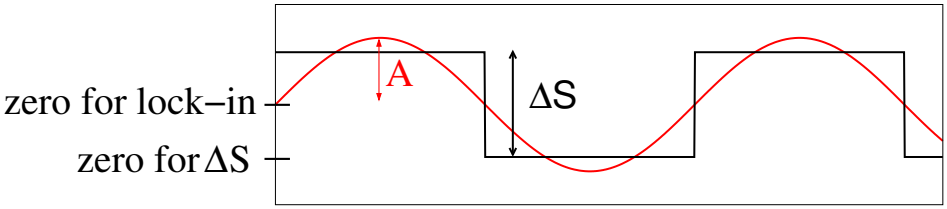

Figure 3.25: *Rectangular signal S (black) and its fundamental Fourier component (red). ΔS is the quantity to be measured, the RMS average of the amplitude A of the sinus wave is the output of the lock–in amplifier.*

center of the spot as a function of the illumination power. The integrated power P of a two-dimensional Gaussian beam profile in central coordinates is

$$P = N \int_0^\infty 2\pi r \, e^{-\frac{r^2}{\sigma^2}} \, dr \quad , \tag{3.11}$$

where r denotes the distance from the center of the focus and σ the standard deviation. Using the relation between σ and the FWHM d_0 of the focus, $\sigma = \frac{d_0}{\sqrt{\ln 2}}$, we obtain

$$N = \frac{P}{\pi\sigma^2} = \frac{P \ln 2}{\pi \, d_0^2} \tag{3.12}$$

Interpreting a rectangular current signal with a lock–in amplifier

The chopper leads to a light signal of rectangular form in time. For the light-induced current change, the same was true as verified with the digital oscilloscope. For most measurements, the lock–in amplifier signal was used to interpret the data. Thus, we need to know the lock–in amplifier readout of a rectangular input signal. A lock–in amplifier measures the root mean square (RMS) average of its input signal. Thus, for a sinusoidal signal $S(t) = A\sin(\omega t)$, the lock–in output will read $\frac{A}{\sqrt{2}}$. For a rectangular input signal, the lock–in amplifier will measure the RMS average of the amplitude of the fundamental Fourier component of the signal. The component is given by

$$A = \frac{1}{\pi} \int_{1 \text{ period}} S(\alpha) \sin\alpha \, d\alpha \tag{3.13}$$

A sketch of the signal is depicted in Fig. 3.25. We are interested in the peak-to-peak amplitude ΔS of the square signal. Hence, the rectangular signal is $S(\alpha) = \frac{\Delta S}{2} \cdot \text{sign}(\sin\alpha)$.
The integral eq. (3.13) for this signal gives

$$A = 0.637 \cdot \Delta S \quad . \tag{3.14}$$

Thus, the relation between the peak-to-peak amplitude ΔS (the quantity of interest) of the rectangular signal and the readout of the lock–in amplifier is:

$$\Delta S = 2.22 \ \cdot \ [\text{lock–in readout}] \tag{3.15}$$

3.5 Measurement Protocol

In this section, we will describe the protocol followed to achieve molecular junctions. After mounting the sample into the bending mechanism, the chamber is pumped until a pressure below $\sim 10^{-6}$ mbar (in Karlsruhe) or $\sim 10^{-5}$ mbar (in Würzburg) is reached. Then a voltage of 1 mV is applied and the current monitored while bending the sample at a speed[16]. of 5000 or 10 000 $\frac{\text{steps}}{\text{s}}$. When the contact is opened, the current drops to zero. By measuring the tunneling current across the break junction while repeatedly narrowing and enlarging the gap, the distance of the tips can be calibrated and the mechanical hysteresis determined. The distance calibration will be thoroughly discussed in section 4.1. The junction is not closed up to metallic contact in this procedure.
To form the tips, the junction is repeatedly opened and closed up to full metallic contact, i.e. up to about 90 % of the conductance of the junction when it was first mounted into the bending mechanism. In most cases, after some 10 cycles, conductance quantization can be seen down to a single conductance quantum $G_0 = \frac{2e^2}{h} \approx 77.5\ \mu\text{S}$. Thus, the tips are atomically sharp at this stage.
After forming the tips, the junction is opened about 50 000 steps[17] and the vacuum chamber vented with nitrogen to ambient pressure. To reduce contamination, the nitrogen flow is sustained during the following procedure. About 15 droplets of $5 \cdot 10^{-4}$ M solution of the molecule are applied to the junction with a pipette. At this stage some of the molecules can split off one of their acetyl protection groups and covalently bond to the gold. Subsequently, the sample is thoroughly rinsed with pure solvent in order to remove small molecular crystals and molecules not chemically bound to the gold. The biphenyl molecule, the anthracene molecule, and the asymmetric molecule are dissolved in tetrahydrofurane (THF), the Ru–complex in acetonitrile. After rinsing, the sample is left to dry in the nitrogen flow for 10–20 min, then the vacuum chamber is pumped until the base pressure is reached. At this stage none of the molecules bridge the gap.

Initial molecular contact

To build the molecular contact, a bias is applied to the open junction. In most cases, we apply 1 V to ensure the molecule is not in a current blocking state, and slowly close the junction while monitoring the current. One Volt leads to a very strong electrical field between the tips of the order of $\frac{1\ \text{V}}{1\ \text{nm}} = 10^9 \frac{\text{V}}{\text{m}}$. The rod-like molecules align in this field and we assume—by surface diffusion—they are pulled into the middle of the gap. Thus, we expect to have one or more molecules in the center of the gap when we narrow the junction at applied bias. This situation is schematically presented in fig 3.26.
A particular molecule will be the first to touch the opposite electrode where it can split off its second acetyl protection group and covalently bond to the gold. This way a covalently bound structure gold–molecule–gold is established. We expect these covalent bonds to be more stable against stress in the junction than the gold leads. Thus, when a gold–molecule–gold contact is further narrowed, we expect the deformation to take place in the leads and not at the molecular contact. This implies that the current stays approximately constant when narrowing the gap at this stage. This behavior was observed by Rubio et al. [100] for

[16] 10 000 $\frac{\text{steps}}{\text{s}}$ corresponds roughly to $(3 \pm 2)\ \frac{\text{Å}}{\text{s}}$
[17] This corresponds roughly to (1.5 ± 1) nm.

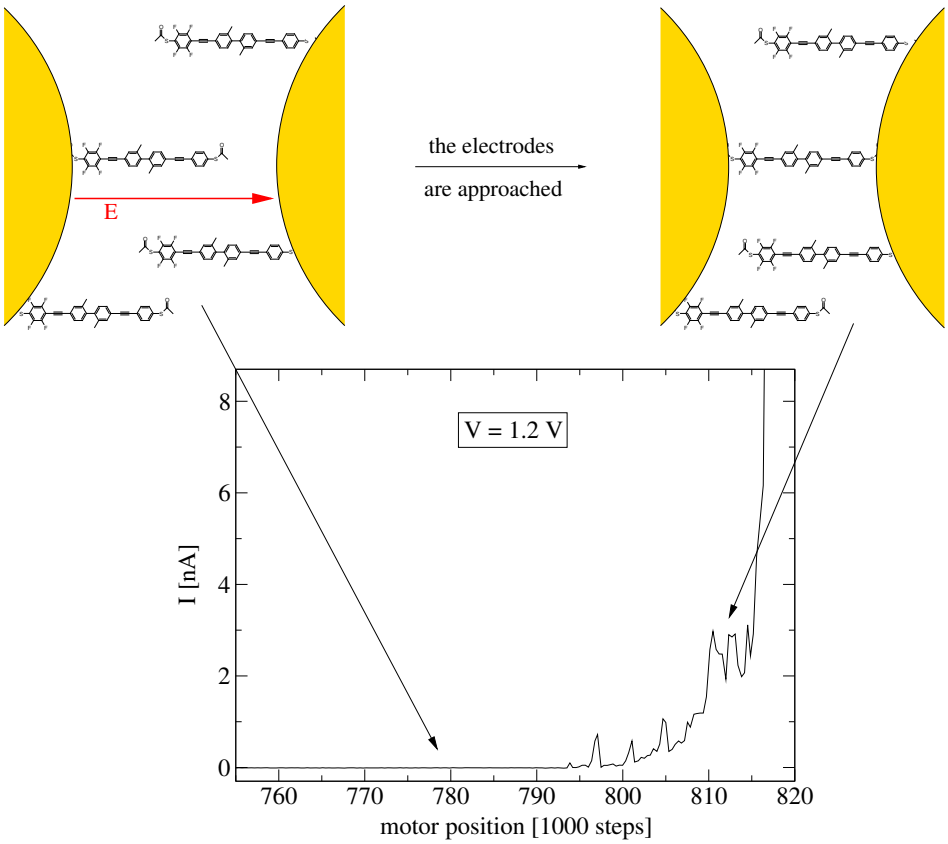

Figure 3.26: *Schematic view of building the first molecular contact. After having applied the molecules and pumped for several hours (usually overnight), a voltage of approximately 1 V (1.2 V in this figure) is applied to the open junction. Presumably, the rodlike molecules align in the very strong electrical field ($\approx 10^9 \frac{V}{m}$) and are pulled into the center of the gap by surface diffusion. Then, the junction is slowly closed while the current across the electrodes is measured. For the open junction (left), no current is detectable. When the gap is very narrow, a noisy tunnel-current with a steep increase sets in. Often, this is followed by a current-plateau which we interprete as molecular contact. Sample–id: W107C24S2.*

pure gold contacts simultaneously measuring the force and conductance while opening a gold junction at room temperature.

We observe this behavior in molecular contacts: When the tips have approached each other close enough, we note a very strong increase of the current which can roughly described as noisy exponential function. In most cases, this exponential increase stops at some point, and the current stays constant although the junction is further closed. This "plateau" is typically 500–5000 steps wide and is seen in about 50 % of the samples when closing a contact for the first time. If no plateau is visible, the junction is fully opened and the whole procedure repeated. When a current plateau is reached, the motor movement can be stopped and molecular IVs be recorded. In this work, the technique to establish the molecular contact was refined. The idea is to first characterize the junction by repeatedly opening and closing the contact and then to decide at which electrode distance IVs are to be measured.

Distance sweeps

The characterization of the molecular junction is performed by closing the open junction under bias until a maximum current $I_{\max}$ is reached. The motion of the motor is then reversed and the junction opened until no current is detectable. This cycle is repeated 5–10 times. These *distance sweeps* can be analyzed for current plateaus.
The first distance sweeps after molecule deposition are performed at comparatively high voltage (1 V) while closing the contact, and at low voltage (10 mV) while it was consecutively opened. This was chosen following a contact protocol used in earlier experiments in our group [28, 29, 95, 98, 101]. After having successfully recorded molecular IVs on a contact, the distance sweeps were usually performed at low voltage for closing and opening. This way, the junction was exposed to weaker electrical fields reducing contamination and degradation of the junction with time.
To record molecular IVs, the motor motion is stopped on a plateau either during closing or opening the junction. The turning direction is *not* reversed prior to recording IVs, hence hysteresis effects of the mechanical setup can be excluded. It turned out that it was favorable for obtaining stable IVs if the motor was stopped in the process of opening the junction as opposed to closing. Distance sweeps will be discussed in more detail in section 4.2.

Characteristics of molecular IVs

In STM experiments and conductance measurements on planar SAM devices, it was found that stable metal–molecule–metal contacts can only be obtained when the molecule is chemically bound to the electrodes [7, 8, 12, 87]. The molecules applied in this work can covalently bind to the gold electrodes. Hence, the stability of the IVs obtained is the main criteria to identify a molecular contact. The "stability" is quantified by repeatedly recording IVs in the range $\sim \pm 1 \cdots 1.2$ V. An example of such a stable IV is presented in Fig. 3.27. A stable molecular contact will repeatedly display the same IV. In most cases, up to approximately 1.5 V can be applied to a molecular junction without altering its IV. The ability to apply such high voltages to a molecular contact alone is already an indication for the stability of the junction. This is not possible for gold tunnel junctions at room temperature for a similar junction conductance. A second criterion for molecular contacts is the form of the molecular IV. The energy-dependent transmission through metal–molecule–metal contacts leads to features in the IVs, while the current–voltage characteristics of contamination is usually ohmic. To summarize: A molecular IV is recorded at or near a current plateau, can be repeatedly measured, and differs from an ohmic contact.

Deformation of the tips during molecule deposition

A quick calculation reveals that we apparently deposit molecules of up to 2.7 nm length in a gap of roughly 1.5 nm. In addition, after molecule deposition, the contact usually has to be closed several 100 000 steps before a molecular contact is detected. We attribute this behavior to the geometry of the tips that apparently has changed during solvent application. This can be for two reasons:

1. Forces of the retracting liquid during the drying process might pull the gold electrodes closer to the substrate. This is supported by SEM images taken after molecular measurements. Often the tips seem lowered after molecular deposition.

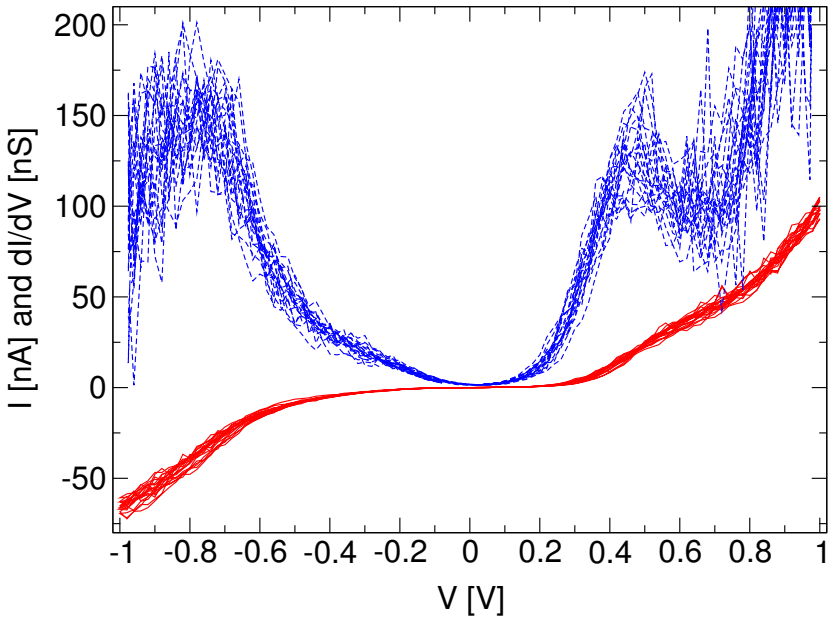

Figure 3.27: *Current–voltage characteristic of a contact to which the asymmetric molecule was applied. The current I (solid red lines) has been repeatedly measured nine times. The differential conductance* $\frac{dI}{dV}$ *has been obtained by numerically derivating the IV and applying a running average over 5 points. The zero-bias conductance in this measurement is 1.6 nS. Sample–id: W107C24S2.*

2. Rearrangement of the gold atoms on the tips of the junction in solution. Thiols are known to alter the form of gold layers [102, 103].

Yield

- On approximately 50 % of the samples, molecular IVs can be recorded after the first molecular deposition.
- On roughly 10–20 % of the samples, molecular IVs can be recorded after applying the molecular solution a second time.
- Approximately 30-40 % of the samples cannot be closed after molecular deposition, i.e. no current can be detected for the entire accessible mechanical bending range of the setup. Roughly $\frac{1}{4}$ of these junctions could be closed by electromigration [104]. Electromigration after molecule deposition is also applied by other groups, e.g. by Park et al. [24].

Hence, the overall yield of molecule deposition is about 70 %.

Chapter 4

Results and Discussion

In this chapter we will present the results obtained in this work. In the first section we will describe our efforts to deduce the correct calibration of the distance of the electrode separation as a function of the motor movement. In section 4.2 we report on measurements that can be used to characterize molecular break-junctions: the conductance of the junction as a function of the electrode separation. In section 4.3 we describe and interpret the measurements performed by shining light on tunneling and molecular mechanically-controlled break-junctions. In further experiments, without illumination, we found discrete switching of the conductance of molecular contacts. This is presented in section 4.4. Finally, in section 4.5 we address the question whether we can be sure that we are actually measuring the properties of the molecule rather than artifacts from, e.g., contamination.

4.1 Distance Calibration

For several questions it would be convenient to know the absolute movement of the metal tips of the break-junction. For example:

- To predict and interpret the thermal expansion of the leads when they are heated either by Joule heating due to the measurement current or due to illumination. This may open the possibility to use the break-junction as a very local temperature probe. The temperature change of the bridge itself is measured.
- To learn how much the gold bridge is stretched before it breaks. This can, e.g., be used to estimate the form of the tips, which is of importance to model the optical near field for an illuminated junction.
- To measure the length of the conductance plateaus of the distance sweeps.
- To interpret the distance sweeps. Is the length of the molecules reflected in the sweeps?
- To predict the movement of the tips when cooling down in order to measure *the same molecular contact configuration* at different temperatures.

The distance calibration of mechanically-controlled gold break-junctions (MCBJs) at room temperature has up to now not been possible to a satisfying degree of accuracy. The established methods enabling a distance calibration such as studying Gundlach oscillations

[30, 105, 106] or the current–voltage (IV) characteristic in the Fowler–Nordheim regime [107] all operate at voltages well above the work function of gold $W \approx 4.8$ eV. But due to the high surface diffusion, only voltages up to roughly 1 V can be applied to gold tunnel junctions at room temperature. Hence, one is left with the low-bias conductance of the junction and geometrical considerations concerning the MCBJ.
To bend the sample, i.e. to change the width of the gap between the gold electrodes of the break-junction, we use a motor. The motor movement M is measured in steps, the respective movement s of the electrode tips in Ångströms. If we neglect hysteresis effects (discussed in section 3.3.2 on page 35), the two quantities are proportional:

$$s = R \cdot M \tag{4.1}$$

This section aims at finding the proportionality factor R of this equation. R will be called *distance calibration factor*. We now introduce the two commonly used methods [108] to calibrate the distance of MCBJs: (i) analyzing the geometry of the sample and the bending mechanism and (ii) measuring the low-bias conductance of the junction.

4.1.1 Two Methods to Calibrate the Tip-Distance of Mechanically-Controlled Break-Junctions

By geometrical considerations

The geometry of the substrate in an MCBJ experiment is the same as that of a "bending beam". Bending beams are used in technical mechanics to measure the Young's Modulus of the beam material. The upper side of the bent sample is stretched, the lower side compressed. For MCBJ samples, the substrate, the polyimide (PI), and the gold layer are all firmly connected (otherwise they would peel off when bending the sample). Both the thickness of the gold (50 nm) and the PI (4 μm) are much smaller than the thickness of the substrate (0.2 or 0.3 mm). Hence, the strain in the gold, PI and the uppermost layer of the steel are to a good approximation equal. Only the suspended part of the gold, the bridge, is not stretched in contrast to the PI layer below it. Thus, the tips of the break-junction are pulled apart by bending the sample.
The formula describing the stretching of the upper side of a bending beam can be adapted to the geometry of the three point bending mechanism of MCBJs. In this geometry, see Fig. 4.1, the strain ε is given by [56]:

$$\varepsilon = \frac{3h}{L^2} \cdot \Delta X \quad , \tag{4.2}$$

where L is the distance between the counter supports, h the thickness of the sample, and ΔX is the Distance the counter supports have been lowered to bend the sample.
The distance between the electrodes Δs is obtained by multiplying the strain ε with the length of the free standing gold bridge u. Then, we can define the displacement ratio r_d as the ratio of Δs over the vertical motion of the pushing rod ΔX, given by:

$$r_d = \frac{\Delta s}{\Delta X} = \frac{3h}{L^2} \cdot u \quad . \tag{4.3}$$

Using the conversion between the pushing rod movement ΔX and the motor movement ΔM, $\Delta X = \xi \Delta M$, with $\xi = 1.6764 \cdot 10^{-9} \, \frac{\mathrm{m}}{\mathrm{step}}$ (see section 3.3.1), we obtain the distance calibration factor R introduced in eq. (4.1):

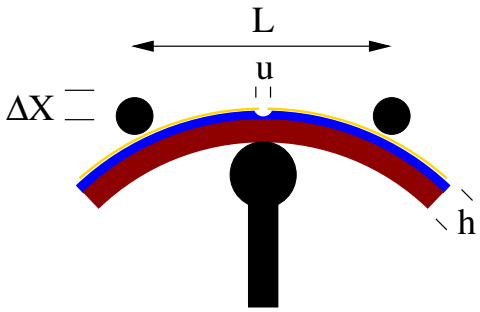

Figure 4.1: *Geometry of the sample in the bending mechanism. L is the distance between the counter supports, u the length of the bridge, and h the thickness of the sample. The shape of the sample is completely controlled by the two counter supports and the pushing rod. While the sample is bent, the sample slips at the points where it touches the counter supports. By bending the sample, the upper side is stretched while the lower side is compressed. In this figure, the counter supports have been lowered by the distance ΔX to bend the sample.*

$$\boxed{R = \frac{\Delta s}{\Delta M} = \xi \cdot \frac{3h}{L^2} \cdot u \approx u \cdot 6.9 \cdot 10^{-9} \, \frac{1}{\text{step}}} \quad . \tag{4.4}$$

Eq. (4.4) will be addressed as the *geometrical formula*. The measurement error stems basically from measuring the length of the bridge u and is assumed to be ± 30 %.[1] The high resolution of the electrode spacing of MCBJs is achieved by the high reduction $\frac{\Delta s}{\Delta X} = r_d \approx 10^{-5}$. In addition, the electrode spacing is extremely stable against vibrations because of the small mechanical path $u \approx 1$ μm.

By tunneling conductance

Simmons' formula, eq. (2.11), yields the conductance of an idealized tunneling contact and depends exponentially on the width of the tunneling gap s. The correction due to s in the prefactor is weak, thus we can use

$$G \propto e^{-\frac{2s}{\hbar}\sqrt{2m\Phi}} \quad . \tag{4.5}$$

The conductance $G(s)$ as a function of the gap width s can be measured at small bias—typically 10 mV. For roughly 75 % of the samples, the expected exponential dependence is well reflected over 2–3 orders of magnitude. In a logarithmic plot, as shown in Fig. 4.2, we have the exponential factor as ordinate y. Using $s = R \cdot M$

$$y = -\frac{2s}{\hbar}\sqrt{2m\Phi} = -M \cdot \underbrace{\frac{2R}{\hbar}\sqrt{2m\Phi}}_{=:F} \quad . \tag{4.6}$$

Then, exponential functions can be fitted to the data and the exponential factors extracted. For each fitted curve $G_i(s)$, we obtain $F_i = \frac{dy_i}{dM}$. An example for this fitting procedure is presented in Fig. 4.3. Using eq. (4.6), we then can deduce R_i for each F_i:

[1] The measurement error of u, see section 3.1.2, is roughly 250 nm, corresponding to 30 % of the bridge length of ∼915 nm.

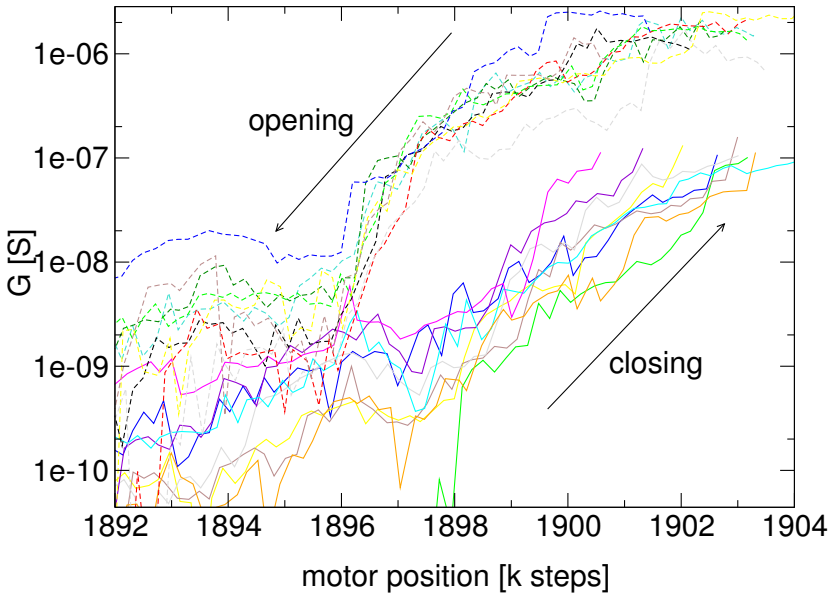

Figure 4.2: *Conductance of a MCBJ in the tunneling regime on a logarithmic scale. The gap width is changed via the motor, hence the x–axis is labeled in steps. Several consecutive measurements are shown in different colors. The gap is narrowed (solid) until a maximum conductance is reached and then opened (dashed) until no current is measurable. The opening curves have been moved up one decade for clarity. Above 1897 k steps the expected exponential behavior of the conductance as a function of the gap width is clearly visible. Note the shift between opening and closing curves as well as the flat part of the opening curves between 1901 k and 1903 k steps: the mechanical hysteresis. Sample-id: W132C27S2.*

$$\boxed{R_i = \frac{F_i \cdot \hbar}{2\sqrt{2m\Phi}} \approx F_i \cdot 4,46 \cdot 10^{-11} \ \frac{\mathrm{m}}{\mathrm{step}}} \quad , \tag{4.7}$$

with $m = 9.11 \cdot 10^{-31}$ kg, $\hbar = 6,5810^{-16}$ eVs, and $\Phi \approx 4,8$ eV. In this thesis, eq. (4.7) will be addressed as the *tunneling formula*. The barrier height of roughly 4.8 eV is confirmed by low-temperature measurements, where gold tunnel junction can be characterized up to high voltages [30, 106]. For the ensemble of calculated values R_i, we can extract the mean R and a measurement error ΔR. Depending on the data quality, two methods are used to estimate the measurement error ΔR:

1. **if the values R_i scatter weakly**, we use the standard deviation of the ensemble of the obtained values.

2. **if the values R_i show strong scattering**, we define the error such that roughly 80 % of the values R_i are inside the range defined by $R \pm \Delta R$. This method is also applied if the exponential factors differ for closing and opening the junction.

Comparing the two calibrations

In Fig. 4.4, the distance calibration factors R determined using tunneling curves and calculated by the aid of the geometrical formula are presented for 13 samples. Clearly, the calibration factors are different. The apparent discrepancies are:

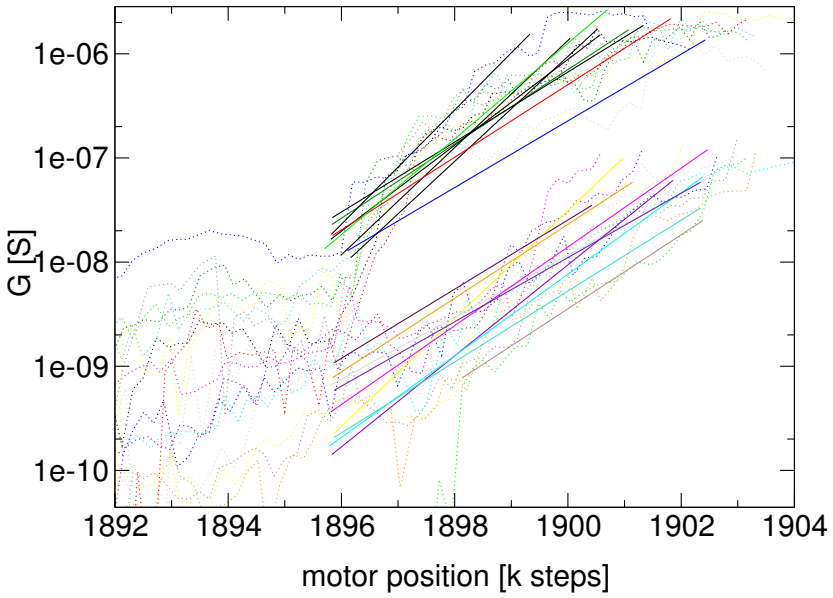

Figure 4.3: *Fitting exponential functions to the data from Fig. 4.2. We select the region in the semilogarithmic plot where the curves show linear behavior. Then exponential functions are fitted to the data. The opening curves and the exponential functions fitted to them have been moved up one decade for clarity. The fits are shown as solid lines and in the region, where the fit was made. The scattering of the slopes can be used as estimate for the measurement error. Sample-id: W132C27S2.*

- The values from the tunneling formula scatter widely
- The values from the tunneling formula are all at least a factor of two higher than those from the geometrical formula.
- Some of the values from the tunneling formula are extremely high.
- The values from the tunneling formula show a correlation between large measurement errors and a high value for R.
- There seems to be no correlation between the magnitudes of the calibration factors evaluated with the two methods.

The discrepancies between the values obtained from the tunneling formula and from the geometrical formula—up to a factor of 10—cannot be explained by deviations from the expected values of the barrier height Φ. Unphysically high values for Φ would have to be assumed, e.g. $\Phi = 480$ eV for sample N° 4 in Fig. 4.4. Before we try to explain this discrepancy, let us first try to evaluate which formula gives the most reliable estimates for the calibration factor R.

Testing the distance calibration

We have seen that the two methods to evaluate the distance calibration factor R give different results. We looked for possibilities to test the distance calibration. These are:

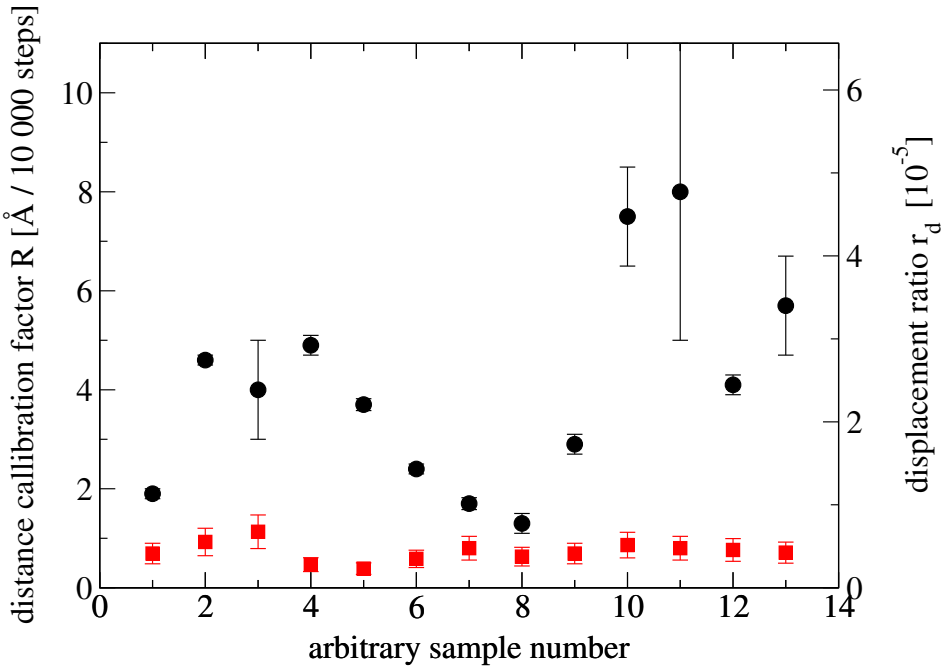

Figure 4.4: *Distance calibration factors R of 13 samples evaluated by fitting tunneling conductance curves (black circles) and by using the geometrical formula (red squares). Using $\xi \approx 1.68 \cdot 10^{-9} \frac{m}{steps}$, we can calculate the corresponding displacement ratio r_d. This is presented on the scale on the right-hand side of the plot.*

1. Contract the metal sheet and the gold tips by cooling down the sample. During the cooling process, the movement of the tips can be compensated by adjusting the motor position such that a constant tunnel current is obtained. Hence, the contraction of the gold and the metal sheet can be measured in motor steps as a function of the temperature. This can be compared with the geometrical formula. Note, both effects (the geometrical formula and the retraction due to cooling) measure strain. Thus, this method cannot be used to directly deduce the distance calibration factor R. Instead, we can deduce if the geometrical formula is in principle correct. Then, the only parameter which could lead to an error in R would be the bridge length u.

2. When a gold contact is torn apart, the gold atoms rearrange in a fashion that enlarges the gap. To close the contact again, the tips have to be approached further than they were pulled apart. We assume that this is roughly the same distance for every gold junction. Thus, it yields an absolute distance which can be compared to TEM or STM measurements, where the tip movement is well calibrated.

We also checked whether there is a correlation between the mechanical hysteresis (cf. section 3.3.2 on page 35) and the distance calibration factor R evaluated according to the tunneling formula. This is presented in Fig. 4.5. As expected there is no correlation apparent.

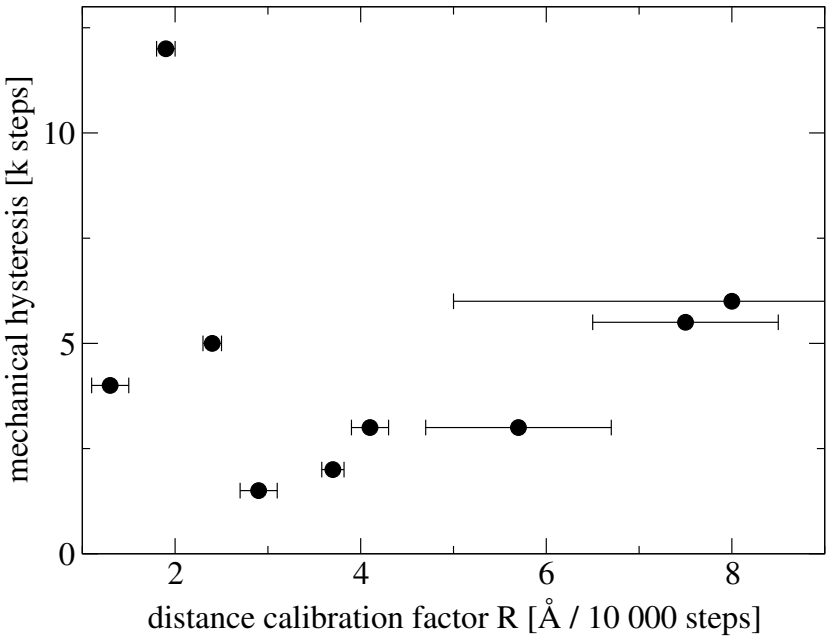

Figure 4.5: *Distance calibration factors R evaluated according to the tunneling formula plotted against the mechanical hysteresis of 9 samples. As expected, there is no apparent correlation between the two quantities.*

4.1.2 Testing the Distance Calibration: Cooling Down the Sample

Unfortunately the method is not exact enough to yield quantitative results. This has several reasons. The sample temperature could only be deduced to an accuracy of roughly ±30 K because the cooling setup reacted very slowly to changes in temperature and due to strong variations of the temperature in the setup and sample. In addition, the linear thermal expansion coefficients of the substrates were difficult to estimate. The substrates are heavily rolled metal plates, hence there are tensions in the material. These lead to strong sample-to-sample fluctuations of the thermal expansion even though the same material is used. Also, the thermal contraction of the pushing rod induces a measurement error which is of the same order magnitude as the measured retraction of the electrodes.

4.1.3 Testing the Distance Calibration: Measuring the Rip–off Hysteresis

Definition of the rip–off hysteresis

When a nanoscopic gold contact is pulled apart, the topmost atoms rearrange in a fashion enlarging the gap. In order to close such a contact again, the tips have to be approached further than to the point where the contact had opened. In this work, we will address this additional distance as *rip–off hysteresis*. It has been observed in TEM [71, 109–111] and STM [112, 113] experiments. An example of how the rip–off hysteresis can be deduced from a TEM measurement is shown in Fig. 4.6. All gold samples in this work showed the rip–off hysteresis, an example of how it is measured is presented in Fig. 4.7. It was routinely evaluated in the step "forming the tips" of the contact protocol (see section 3.5 on page 46).

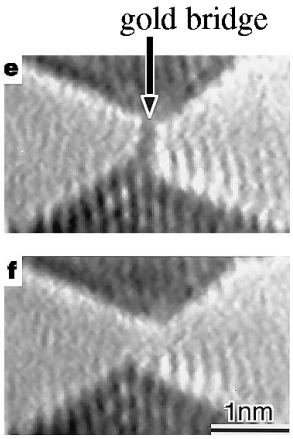

Figure 4.6: *TEM image from which the rip–off hysteresis can be deduced. Gold atoms appear dark in the image. The gap width after rupture of the contact is approximately equal to the rip–off hysteresis. In this image, we measured 5 Å. The image is taken from [71].*

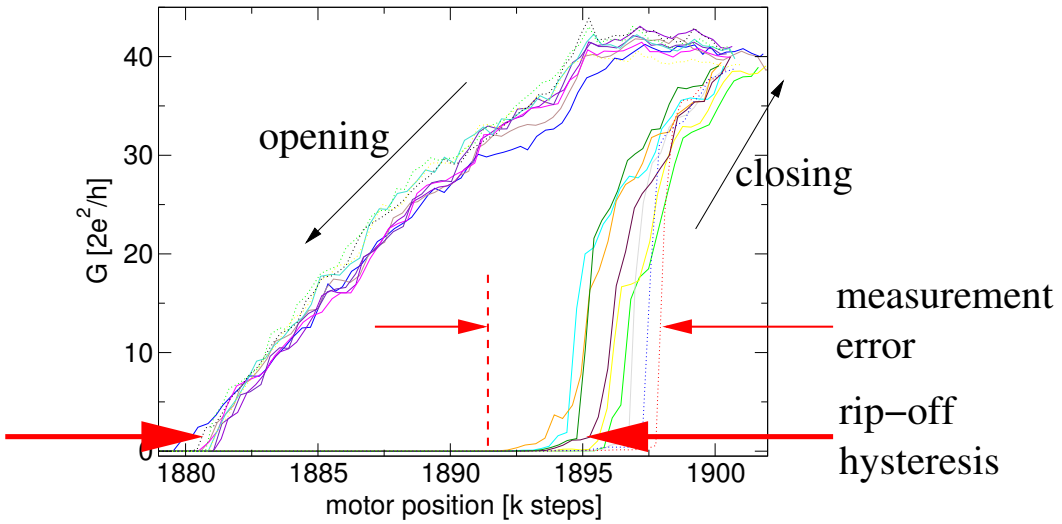

Figure 4.7: *How to measure the rip–off hysteresis. In this viewgraph the conductance of the contact (without the 1 kΩ-resistance) is plotted against the motor position. The contact was subsequently closed and opened 9 times, all conductance curves are displayed to show the scatter in this type of measurement. The rip–off hysteresis is measured as the distance between the opening and closing curves at the level below one conductance quantum $G_0 = \frac{2e^2}{h}$. The scattering of this measure between different curves is used as measurement error. The backlash of the metal transmission sheet is corrected according to eq. (3.10), see page 38. Sample–id: W106C22S1.*

We expect the rip–off hysteresis of nanoscopic gold contacts to show strong sample-to-sample fluctuations but to be a statistically measurable quantity.

Several groups have imaged the breaking process of gold wires in TEMs. In the images of their publications, the rip–off hysteresis of the particular published gold breaking process can be measured. Note, though, that in all TEM measurements carbon contamination is very

likely [114]. Hence, it is important to compare the TEM measurements with values deduced from STM measurements. The rip–off hysteresis deduced from TEM and STM experiments are all of similar magnitude. Thus, the influence of carbon contamination on the value of the rip–off hysteresis seems to be small. We evaluated the following publications for the displayed rip–off hysteresis:

- Kizuka et al. [109]: $\Delta s \lesssim 10$ Å. The authors state in their paper that the electrodes retract a distance of some atom layers.
- Ohnishi et al. [71]: $\Delta s \lesssim 5$ Å.
- Takai et al. [110]: $\Delta s \lesssim$ (7–10) nm.
- Rodrigues et al. [111]: The difference between a chain of 4 atoms and after rupture minus this chain is $\Delta s \approx 4$ Å. Adding the distance of one atom (≈ 3 Å) gives an estimate of $\Delta s \approx 7$ AA.
- Brandbyge et al. [112] (STM with deep indentation of the tip): $\Delta s \lesssim 10$ Å.
- Yanson et al. [113] (STM measurement): $\Delta s \approx (6 \pm 1)$ Å at 4.2 K.

Thus, rip–off hysteresis values of 5–10 Å are reported in the literature. In some of the publications, atomic chains longer than one atom are pulled from the contact. In our experiments, this is not the case — the conductance plateaus at one or two conductance quanta are always very short. Hence, we expect the rip–off hysteresis in our experiments to be closer to 5 Å than 10 Å.

Comparing the reported hysteresis values with our experiments

This section aims at comparing the distance calibration factor R obtained from the geometrical formula, eq. (4.4) with the calibration measured by evaluating the tunneling formula, eq. (4.7). Hence, in this section, we will treat the rip–off hysteresis S_r deduced from the publications cited above as *given* quantity. In contrast, the distance calibration factor R as well as the rip–off hysteresis M_r measured in steps are the *measured* quantities. Eq. (4.4) relates S_r and M_r:

$$S_r = R \cdot M_r \quad . \tag{4.8}$$

The measurement error is obtained according to the Gaussian error propagation rule

$$\Delta S_r = R \cdot \Delta M_r + M_r \cdot \Delta R \quad . \tag{4.9}$$

We calculated S_r and ΔS_r for all samples where the distance calibration factor R could be deduced. The resulting rip–off hysteresis values as a function of R is depicted in Fig. 4.8. The values calculated according to the tunneling formula are presented as black dots, the values deduced using the geometrical formula as blue squares. The expected rip–off hysteresis of 5-10 Å is indicated as yellow bar. All measured values of the rip–off hysteresis have been corrected for the backlash of the metal transmission sheet according to eq. (3.10), see page 38. The rip–off hysteresis values calculated from the geometrical formula are clearly out of range. For the values estimated from tunneling conductance measurements, the data points can be

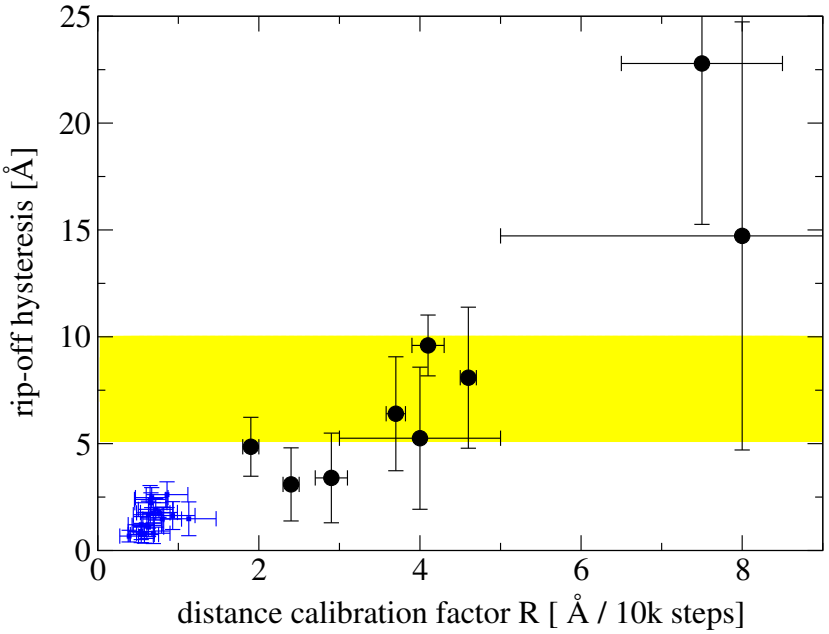

Figure 4.8: *Measured rip–off hysteresis as a function of the distance calibration factor R, where R was either calculated according to the geometrical formula (blue squares) or measured using the tunneling formula (black dots). The measured rip–off hysteresis was corrected for the backlash of the metal transmission sheet and transformed into Ångströms using equations (4.8) and (4.9). The expected range of the rip–off hysteresis is indicated as yellow bar.*

divided into two groups: (i) the points with a small measurement error[2] ΔR, all lie in or close to the expected range between 5 and 10 Å. (ii) points with large error bars ΔR. Two of them are clearly out of range of the expected rip–off hysteresis.

Thus, the only distance calibration factors which reflect the rip–off hysteresis of nanoscopic gold contacts are those which are evaluated from tunnel-conductance measurements and which have, in addition, small error bars. The distance calibration factors evaluated from the geometrical formula clearly are to small. From Fig. 4.8 we estimate an average distance calibration factor from the tunneling formula values which lie in or very close to the expected rip–off hysteresis (yellow bar):

$$\boxed{R \approx (3.3 \pm 1.5)\ \frac{\text{Å}}{10\,000\ \text{steps}}} \quad , \tag{4.10}$$

where the uncertainty of 1.5 $\frac{\text{Å}}{10\,000\ \text{steps}}$ might stem from sample-to-sample fluctuations.

The statistical average of the rip–off hysteresis of 14 samples[3] was measured to be $(23 \pm 14) \cdot 1000$ steps which, using eq. (4.10), roughly corresponds to 7.6 Å in good accordance to the expectation of 5–10 Å stated above.

[2]The measurement error is a measure of how well the tunnel conductance as a function of the gap width is described by an exponential dependence, see page 54

[3]For 5 samples the rip–off hysteresis could be deduced but not the distance calibration factor according to the tunneling formula.

Concluding remarks concerning the distance calibration

We compared the rip–off hysteresis measured in our experiments with values reported in the literature. Only the distance calibration factors deduced (with a small measurement error) from the tunneling formula eq. (4.7) are consistent with these rip–off hysteresis values. The distance calibration factors calculated from the geometrical formula are at least by a factor of 3 too small. Thus, we will use the distance calibration factor $R \approx (3.3 \pm 1.5)\ \frac{\text{Å}}{10\ 000\ \text{steps}}$ to interpret the distance measurements in this work.
How can the discrepancy between the two methods be explained? Assuming that the geometrical formula is correct, the discrepancy can be explained if the bridge length is about three to five times larger than deduced by our measurement technique described in section 3.1.2. This is conceivable because we use no titanium adhesion layer for our samples. Possibly, the first several micrometers of the gold layer can slide freely on the PI substrate. This distance would exhibit strong sample-to-sample fluctuations. These are actually observed in the distance calibration using the tunneling formula.

4.2 Molecular Conductance as a Function of the Electrode Separation

4.2.1 General Description

The first distance sweep is already performed when establishing a molecular contact after molecule deposition, see the contact protocol, section 3.5. To record a distance sweep, a bias voltage is applied, and the contact is repeatedly closed and opened. We performed these sweeps in two modes:

1. Close the contact at a high bias voltage in the range of 1–1.2 V until a maximum current is reached. Then subsequently open the junction at a low bias voltage of 10–20 mV.

2. Close the contact at a low bias voltage of 10–20 mV until a maximum current is reached. Then subsequently open the junction at the same bias voltage.

Method 1 was employed for the first sweeps after molecular deposition in order not to deviate from the contact protocol of former works in the INT [99, 115]. Method 2 was used in later sweeps to reduce the influence on the contact due to the measurement. The advantages of method 2 are reduced electric fields (leading to less contamination and more stable measurements) and reduced Joule heating due to the measurement. The drawback is that only molecular contacts whose IV has a non-zero conductance at 10–20 mV can lead to a conductance plateau in the distance sweeps. An example of a single first (closing-) sweep at high bias was already presented in Fig. 3.26 on page 47 for the asymmetric molecule. In Fig. 4.9 we present an example of three (closing-) distance sweeps of a contact to which the anthracene molecule has been applied. The sweeps were recorded at a low bias voltage of 10 mV. The (opening-) distance sweeps obtained in the same run are presented in Fig. 4.10.

4.2.2 Good Operation Points

We have observed that the most stable IVs occur close to the low-current edge of a plateau. An example where the motor was stopped while closing the junction is indicated as red solid line

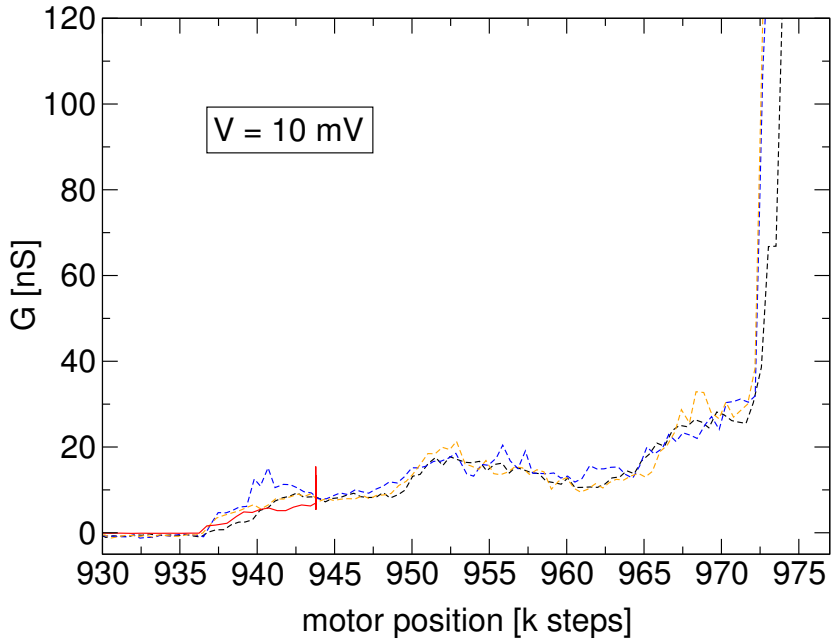

Figure 4.9: *Low-bias voltage distance sweep closing a contact to which the anthracene molecule has been applied. To demonstrate the reproducibility of the measurement, three consecutive sweeps are shown as dotted lines in different colors. Three conductance plateaus are clearly visible. The fourth sweep, presented as solid red line, was stopped at the position 943 k steps to subsequently record IVs of the contact. Sample-id: W107C17S2.*

in Fig. 4.9. It turns further out that stable IVs are better formed during opening operation, rather than during closing.

4.2.3 Evolution of the Distance Sweeps Over Time

Molecular contacts evolve over time. This can be deduced from the distance sweeps. In the beginning, the changes are relatively rapid, i.e. the distance sweeps evolve on the time scale of hours. Then they are relatively stable and show reduced noise for several days. During this period the most reproducible IVs can be measured.
Roughly two weeks after the molecule deposition, the quality of the sweeps decreases. It is then more difficult to obtain stable and non-ohmic IVs, and the conductance plateaus become shorter or disappear totally. Probably, by then, adsorbates have accumulated in the contact region hindering the measurements.

4.2.4 Intermediate Maximum Structure in the Distance Sweeps

Stable IVs cannot always be recorded when molecules have been applied to a junction. We noted a correlation between the form of the opening curves of the distance sweeps and the possibility to obtain stable IVs on a contact. The form of the opening sweeps looks like a "hill" and an example for this is shown in Fig. 4.11. The data is the same as in Fig. 4.10.
We analyzed the distance sweeps of 18 samples to which a molecular solution of one of the four molecules described in section 3.2 was applied. On 13 of these 18 samples we were able to

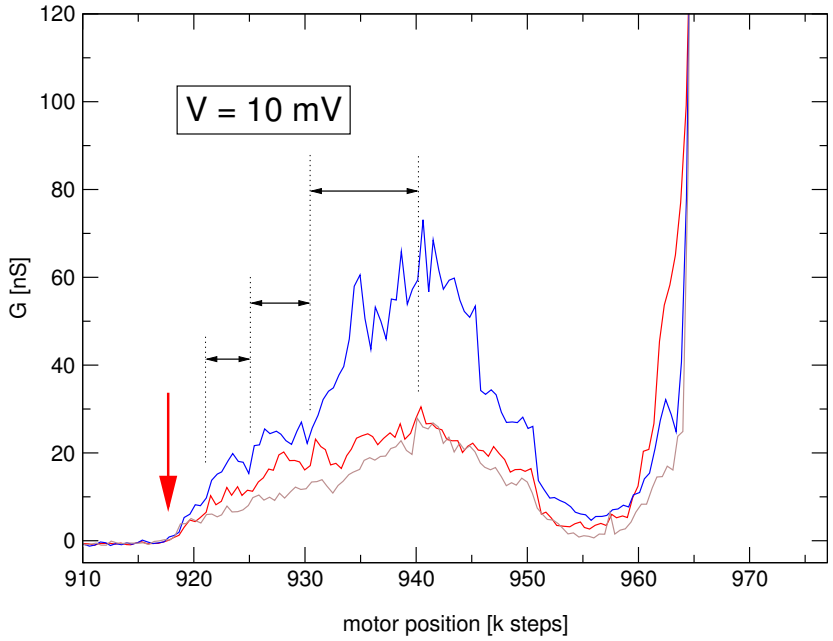

Figure 4.10: *Low-bias voltage distance sweep opening a contact to which the anthracene molecule has been applied. To demonstrate the reproducibility of the measurement, three consecutive sweeps are shown as solid lines of different color. Due to the mechanical hysteresis, the opening sweeps are shifted to the left with respect to the closing sweeps shown in Fig. 4.9. On the left-hand side, plateau-like structures (though not flat) are discernible. They are indicated in the figure (black arrows and dotted lines). Note, the motor position of these "plateaus" is very reproducible, while their conductance is not. In contrast to distance sweeps of bare gold electrodes, molecular contacts show* no rip–off behavior *(see position indicated by the red arrow). Sample-id: W107C17S2.*

record stable IV characteristics. The hill-like structure was present in 9 of the 13 successfully measured contacts. In addition, there was a general tendency that IVs on samples comprising the hill-like structure were more stable than on the other 4 samples. The best location in the distance sweep to stop the motor and record IVs was shortly before the contact was fully opened on the lowest plateaus on the hill.

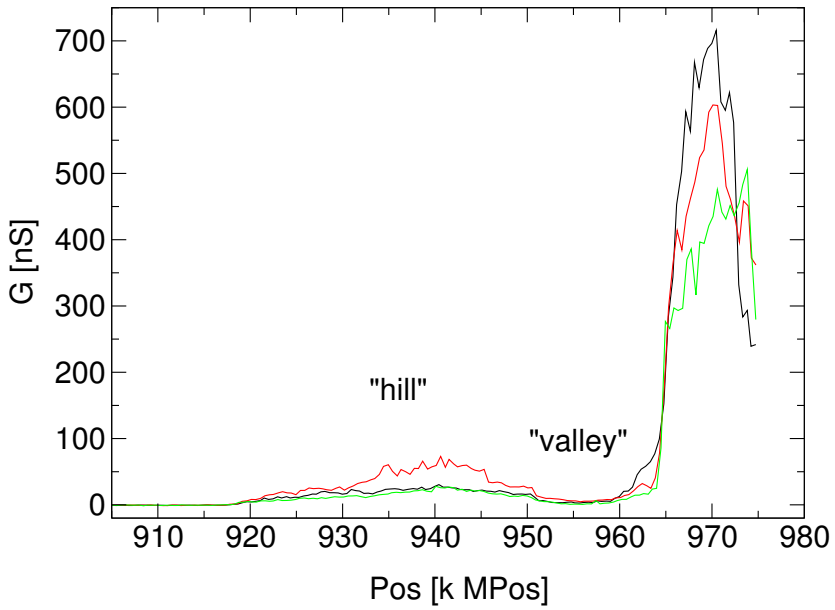

Figure 4.11: *Hill-like structure of the conductance while opening a contact. Three consecutive opening sweeps of a junction comprising the anthracene molecule are shown, the data is the same as in Fig. 4.10. From right to left (this is the measurement direction): after a steep decrease, the conductance goes through a minimum, the "valley", and then over a maximum, the "hill". This hill was observed for most samples where stable IVs could be recorded. The increase from 975 to 970 k is often observed and attributed to relaxation effects in the mechanical setup which lead to a small approach of the electrode tips when the motor motion is reversed. Bias: 10 mV, sample-id: W107C17S2.*

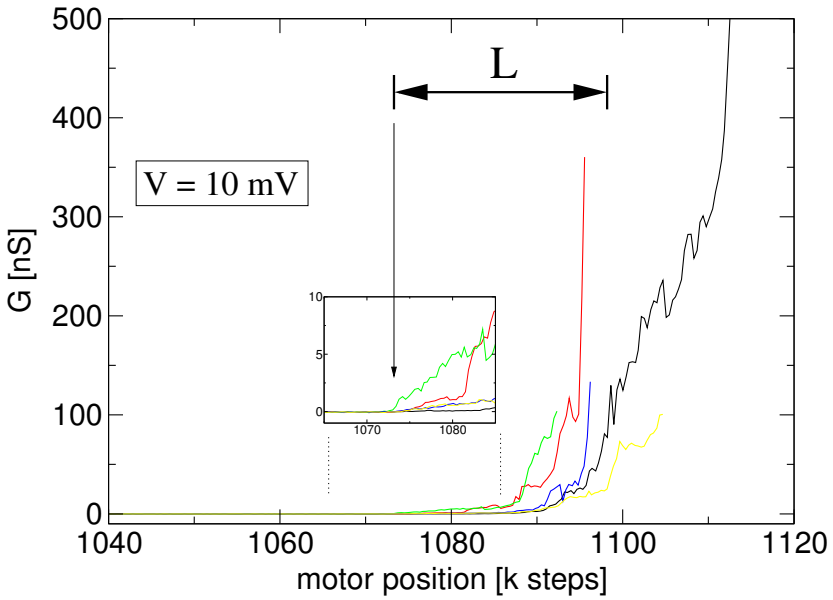

Figure 4.12: *Measuring the distance from the onset of the current to the steep increase in a distance sweep. To this contact, the biphenyl molecule was applied. The onset of the current is in most cases very well defined. The steep increase varies from sweep to sweep (four sweeps are displayed in different colors). The uncertainty of this point is regarded as the measurement error. The distance measured in this figure is* (27 ± 10) *k steps. Sample–id: W107C08S2.*

4.2.5 Is the Molecular Length Reflected in the Distance Sweeps?

It is reasonable to ask whether the length of the molecules applied to a junction is reflected in the distance sweeps. Such a measurement has so far not been performed in molecular MCBJ experiments. The lengths of all molecular species, defined as the distance between the sulphur atoms, are given in section 3.2: Biphenyl molecule: 1.1 nm, anthracene molecule: 1.5 nm, asymmetric molecule: 2.4 nm, and Ru–complex: 2.7 nm. We will now propose a method to measure the length of the molecules in the distance sweeps.

Possible method to measure the length of the applied molecules in the distance sweeps

When closing a contact there is always a very steep increase after having passed the conductance plateaus. We attribute this steep increase to a tunnel current between the electrodes when they come so close to each other that a tunnel current can flow through a large area. The distance from the onset of a measurable current to the steep increase can be measured, see Fig. 4.12, and should correspond approximately to the length of the molecules applied to the junction.
Ideally, we should measure the distance from the onset of the current to the point where the conductance is close to the conductance quantum $G_0 = 77.5\ \mu$S. This means, measuring a current over roughly 5 orders of magnitude. In our experiments the current range was chosen such that the low conductance in the distance sweeps can be analyzed. Hence, the conductance value of G_0 was out of range. Instead, we used the maximum conductance

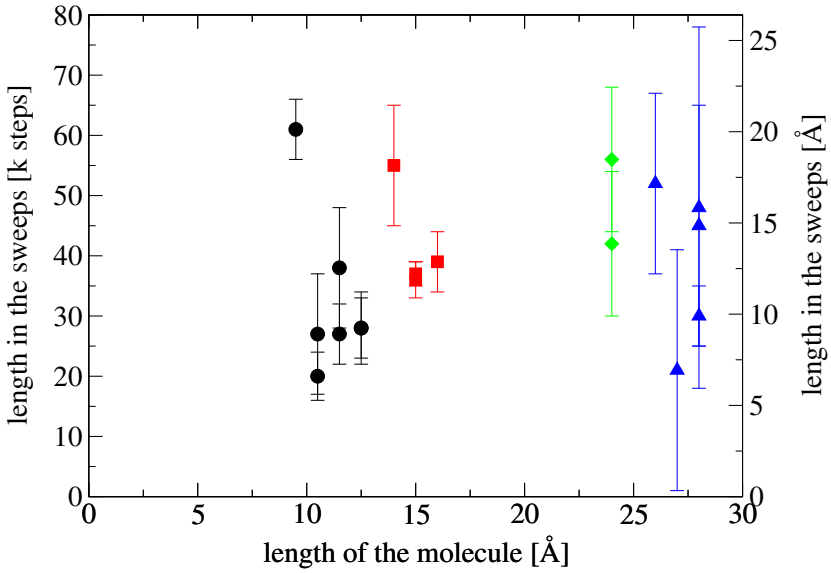

Figure 4.13: *Length of molecular contacts from the onset of the current to the steep increase. The length was deduced as indicated in Fig. 4.12. Measurements on different contacts but comprising the same molecule are shifted by 1 Å on the x-axis. biphenyl molecule: black dots, anthracene molecule: red squares, asymmetric molecule: green diamonds, and Ru–complex: blue triangles. The Ångström scale on the right hand side was calculated from the estimate of the distance calibration eq. (4.10).*

measured in the sweeps. The lengths measured on 11 molecular contacts are presented in Fig. 4.13. They are of the order of 10–15 Å, i.e., the length of the molecules. But the length dependence is not clearly visible.

4.2.6 Histograms of Distance Sweeps

Histograms of conductance distance sweeps have had great success in presenting and interpreting the data of few-atom metal contact measurements [16,112,113,116]. The method has also been applied to molecular contacts by Xu et al [10,16,117].
There is, however, a drawback to using histograms to interpret conductance data. The method aims at finding preferred conductance values of a contact. In our case the conductance values of the current plateaus are of interest. Two properties of these plateaus hamper the interpretation of the data using histograms.

1. The conductance plateaus can be very short. Even very reproducible—but short—conductance plateaus will not contribute noticeably to a conductance histogram. Conductance plateaus of metal contacts are wider than those from molecular contacts.

2. There are indications that the position of the plateaus is better reproducible than their magnitude. Two examples for this behavior are presented in figs. 4.9 and 4.10. To demonstrate this effect, a histogram of the data of Fig. 4.9 is presented in Fig. 4.14. The conductance values measured between 0 and 40 nS were grouped into 50 bins for this figure. The peak at 8 nS can be attributed to the conductance plateau at 945 k steps

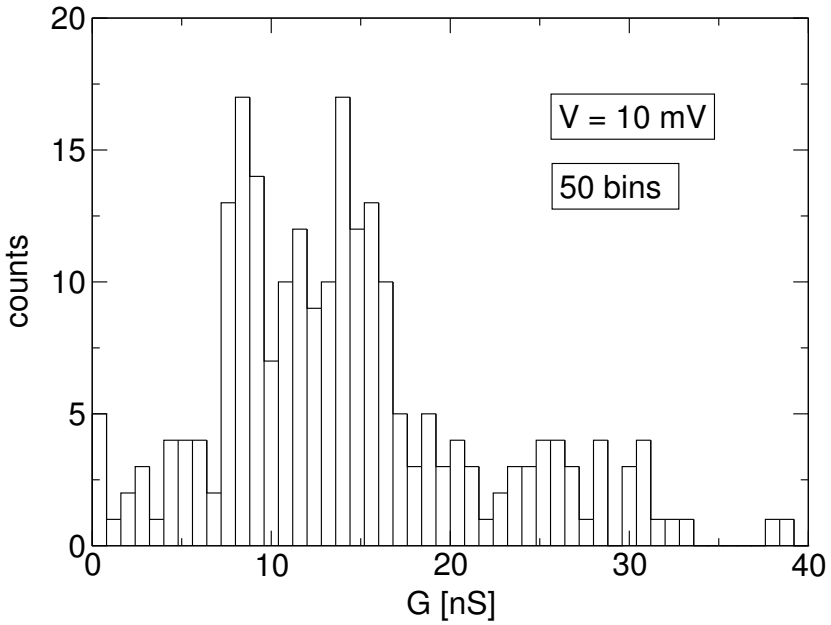

Figure 4.14: *Histogram of the conductance values of the conductance plateaus presented in Fig. 4.9. All data points were grouped into 50 bins between 0 and 40 nS. The conductance of the lowest-lying conductance plateau in Fig. 4.9 is visible as peak centered at 8 nS in the histogram. The two other conductance plateaus at 18 and 24 nS are only very weakly reflected in the histogram.*

in Fig. 4.9. The other conductance plateaus are not clearly discernable in the histogram. No additional insight is gained compared to the distance sweep.

4.3 Interaction with Light

In this section we report on measurements where ultra short light pulses from a titanium sapphire laser were applied to molecular or tunnel break-junctions. The setup is described in section 3.4, see page 43. With this setup, it is in principle possible to study the entire range of effects described in section 2.6.2. In the institute EP1 in Würzburg, a pulse shaper[4] was at hand. It was conceivable to build up an experiment where coherent control of a (purely optical) pump–probe setup could be used to maximize the current response to the illumination. First experiments illuminating metallic tunneling contacts were performed in Würzburg prior to the present experiments using an STM setup [79, 119]. The current signal was dominated by thermal expansion of the STM tip, and it proved difficult to stabilize the current response to the illumination. MCBJs proved to be more stable and easier to handle under illumination.
In this work, the power of the light incident on the sample is either denoted *power* signifying the average power during light–on periods, or *pulse power* if the peak power of a light pulse is addressed. For illumination parameters and the setup of the measurement, see section 3.4. To correct for interfering electrical signals, a dark measurement, i.e. with the laser beam blocked, was always subtracted from the data measured under illumination.

4.3.1 Photoinduced Conductance

The illuminated mechanically-controlled break-junctions proved to be very stable and always exhibited a response to the light, which could be measured to an accuracy so far unreachable in former STM experiments performed in Würzburg. This light-induced response was a current amplification ΔI which was independent of the bias voltage sign. In addition, this current increase was always proportional to the DC current which we measured simultaneously. This is illustrated for a tunnel contact in Fig. 4.15.
To further analyze the signal, we varied the light mode used for illumination and the type of contact, i.e. molecular or tunnel contacts. For these variations, we observed that the light induced current increase always was of the order of a few percent of the DC current and that it showed strong sample-to-sample fluctuations. The response to blue light was roughly an order of magnitude larger than the response to red light. The difference between pulsed and continuous-wave (CW) illumination was negligible, i.e. the variation was smaller then the sample-to-sample fluctuations.
Hence, we found for all contacts and for all light modes:

$$\boxed{\Delta I \propto I} \quad , \tag{4.11}$$

where ΔI denotes the light-induced current change and I the DC current.
To illustrate the time dependence of the signals, we show current traces of a molecular contact comprising the biphenyl molecule recorded with the digital oscilloscope in Fig. 4.16. The traces shown are averages over 1000 scans. The spikes at zero bias result from crosstalk of the acousto–optical modulator used to chop the light in this experiment. They can be used to estimate the time resolution of the current measurement (response to a δ–pulse).

[4] A pulse shaper can give any desired temporal dependence to the envelope $A(t)$ of a short laser pulse. Employing a pulse shaper, the yield of optically triggered chemical reactions can be maximized. [118]

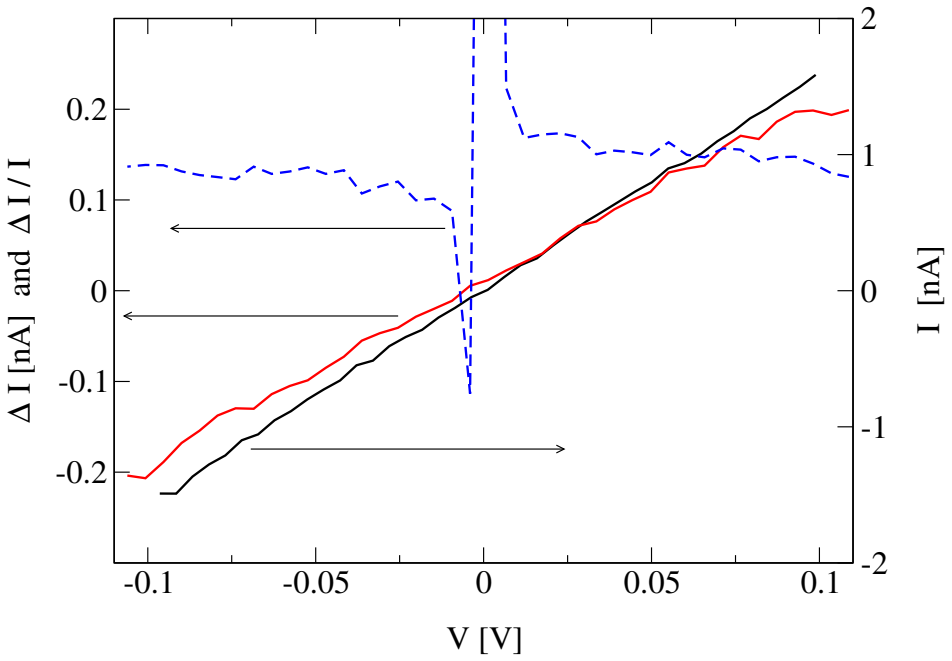

Figure 4.15: *DC current and light-induced current amplification for a tunnel contact for bias voltages between ±100 mV. The DC current I is presented as black line, the light-induced current increase ΔI in red. The ratio $\frac{\Delta I}{I}$ is shown as blue dashed line. Apart form the disturbance around zero bias stemming from a small current offset which will be analyzed in section 4.3.5, ΔI is proportional to I. Light parameters: 20 mW, 800 nm, pulsed. Sample–id: W107C17S2.*

Exponential fits yield an exponential decay time constant of $\tau \approx (0.12 \pm 0.03)$ ms. Within the time resolution of the current measurement setup, the current increased state is a steady state during the entire light-on period. Next, we will take a closer look at the power dependence of the light-induced signal.
The current response as a function of the incident light power on a contact with the anthracene molecule is shown in Fig. 4.17. Basically, the light-induced current increase ΔI depends linearly on the incident illumination power P. Illuminating a contact with the asymmetric molecule and a tunnel contact, we found similar behavior (both not shown). The response of the junctions to blue light was about one order of magnitude higher than that of red light as can be deduced from the slope $\frac{\Delta I}{P}$. The slopes we measured are:

- tunnel contact: 30 $\frac{\text{nA}}{\text{W}}$ (red, pulsed) and 1080 $\frac{\text{nA}}{\text{W}}$ (blue, pulsed). Sample–id: W107C24S2.
- anthracene molecule: 28 $\frac{\text{nA}}{\text{W}}$ (red, pulsed) and 340 $\frac{\text{nA}}{\text{W}}$ (blue, pulsed). Sample–id: W107C17S2.
- asymmetric molecule: 14 $\frac{\text{nA}}{\text{W}}$ (red, CW). Sample–id: W107C24S2.

Note, these data are not corrected for the different FWHM of the blue and red foci. Sample-to-sample fluctuations are greater than this error.

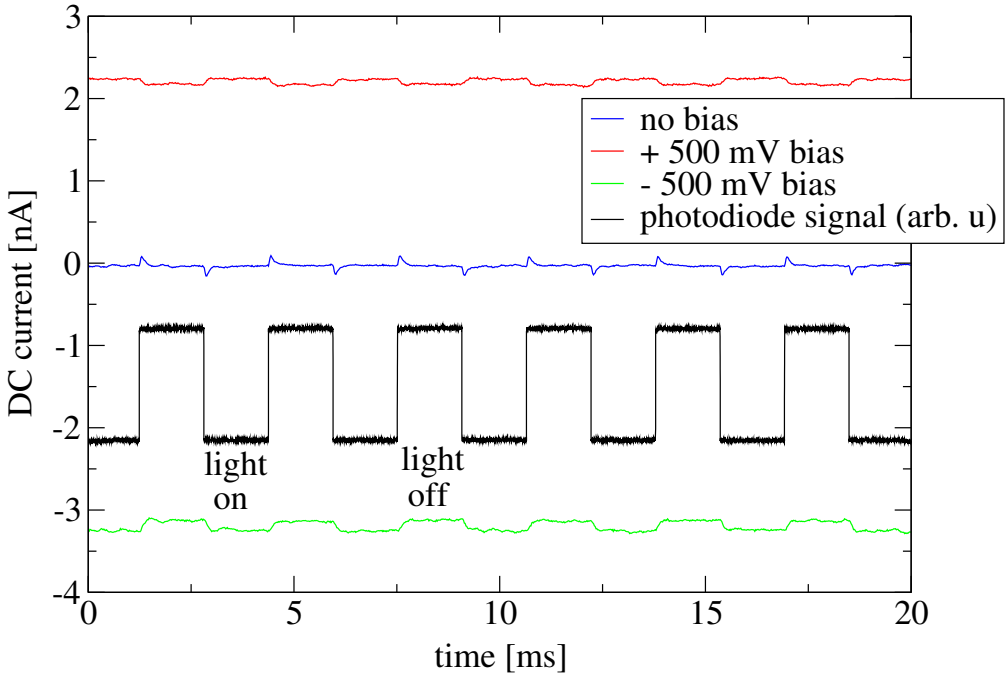

Figure 4.16: *Oscilloscope traces of the light-induced signal of a molecular junction with the biphenyl molecule. The traces are averages over 1000 scans. In blue: no bias, in red: +500 mV, in green: −500 mV, in black: control signal of a diode. The spikes at zero bias result from crosstalk of the acousto–optical modulator used in this measurement. Sample-id: W107C13S1, light: 800 nm, pulsed, 2.6 mW.*

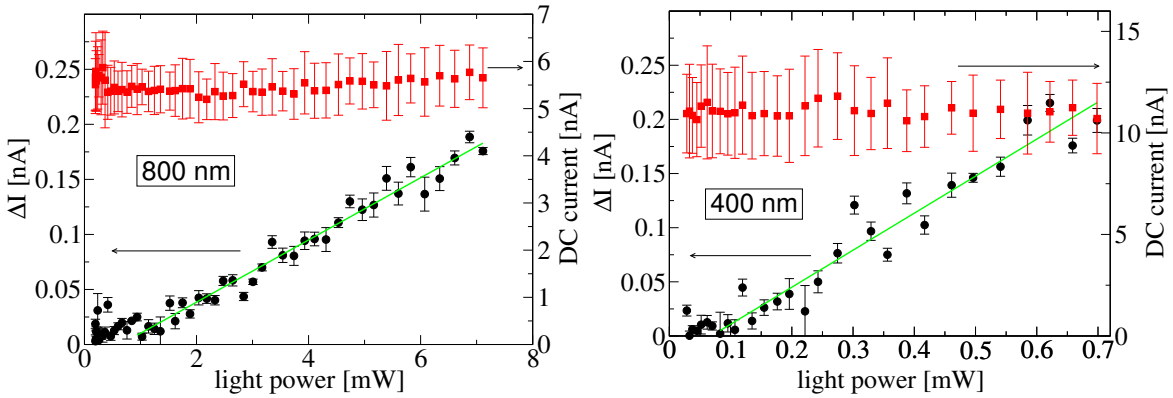

Figure 4.17: *Illumination power dependence of the light-induced signal ΔI of a contact comprising the anthracene molecule. Left: for red pulsed light and right: for blue pulsed light. Red squares: DC current I, black circles: ΔI, green line: linear fit to ΔI. Note the different scales for I and the light power in the two plots. The slopes are 28 $\frac{nA}{W}$ for red and 340 $\frac{nA}{W}$ for blue light. Sample–id: W107C17S2.*

4.3.2 Conductance Enhancement for Tunnel Contacts

Tunnel contacts are better defined systems than molecular contacts. Thus, we will first analyze the conductance enhancement for tunnel contacts in detail and propose a model to explain it.

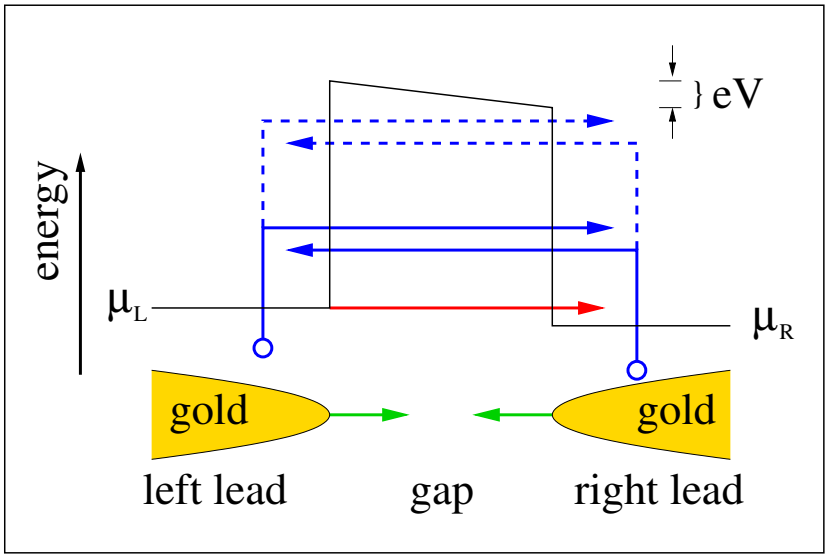

Figure 4.18: *Interaction mechanisms which could lead to a tunnel current enhancement. In red: DC tunnel current; in blue: electrons excited somewhere in the Fermi sea "see" a lower barrier and can thus lead to a large current contribution—two-photon excitation is conceivable; in green: thermal expansion of the electrodes will reduce the gap width leading to a higher current.*

Possible mechanisms

The current increase could originate from different mechanisms that are schematically depicted in Fig. 4.18.

- in red: DC tunnel-current
- in blue: tunneling of excited electrons. If a different number of electrons is excited in each lead, a net current will flow.
- in green: thermal expansion of the electrodes heated by the light. The gap is narrowed leading to an increased DC current.
- not shown: non-linear effects

What behavior of the current enhancement ΔI would we expect for the different mechanisms?

- *excited electrons:* The number N of excited electrons will depend on the absorption of the respective lead. Thus, effects like the geometry of the junction should have a strong influence.

  For excited electrons: ΔI should not show a clear dependence on I.

- *thermal expansion:* from the rectangular form of $\Delta I(t)$, see Fig. 4.16, we know that the illumination leads to a steady state. Thus we expect a fixed temperature during illumination in the thermal expansion model. This will lead to a thermal expansion Δs of the leads while the other parameters of the tunneling barrier, see eq. (4.5), are not changed.

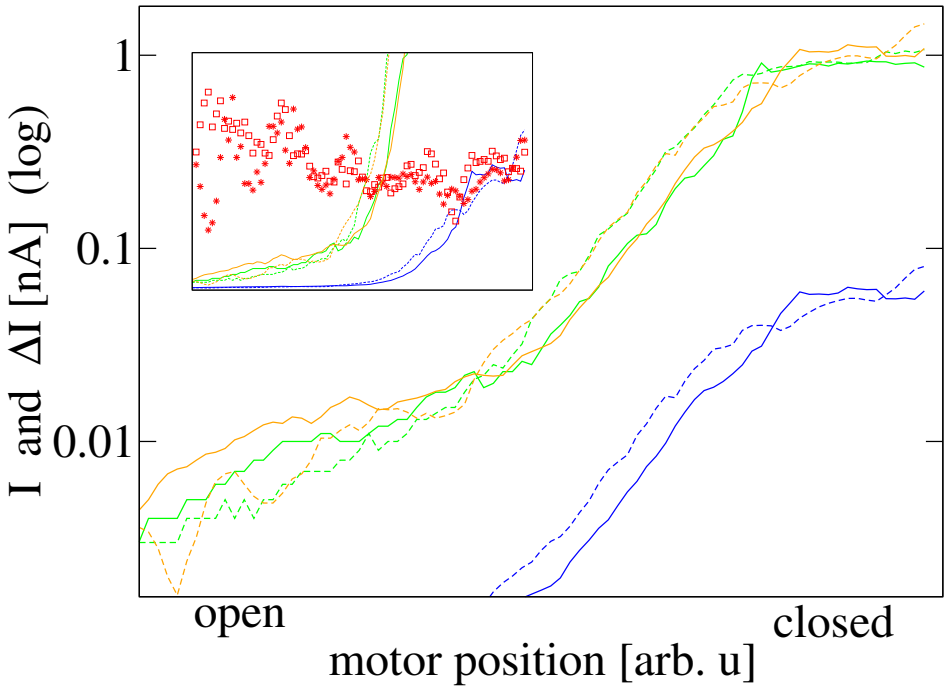

Figure 4.19: *Two consecutive measurements of the tunneling current at 100 mV bias while closing the junction. The current is plotted on a logarithmic scale. In green: DC current I; in blue: current increase ΔI; in orange: $\Delta I \times 18$. In the inset the same plot is shown with the current and $\frac{\Delta I}{I}$ (in red) presented on a linear scale. $\frac{\Delta I}{I}$ is constant over 2 orders of magnitude of the current. Sample-id: W107C24S2, light: 800 nm, pulsed, $P = 2$ mW.*

$$\text{illuminated: } I \propto e^{-\frac{2(s-\Delta s)}{\hbar}\sqrt{2m\Phi}}\ ; \qquad \text{dark: } I \propto e^{-\frac{2s}{\hbar}\sqrt{2m\Phi}} \tag{4.12}$$

If we calculate $\frac{\Delta I}{I}$, we get

$$\frac{\Delta I}{I} = (e^{\frac{2\Delta s}{\hbar}\sqrt{2m\Phi}} - 1) \approx \frac{2\Delta s}{\hbar}\sqrt{2m\Phi} \quad . \tag{4.13}$$

For thermal expansion: $\Delta I \propto I$ and $\frac{\Delta I}{I}$ independent of s.

- *non-linear effects:* The response for CW and pulsed light of the same average power should be different because the photon density is many orders of magnitude increased for pulsed light. In addition, the power dependence should be non–linear.

  For non-linear effects: $\Delta I_{\text{CW}} \neq \Delta I_{\text{pulsed}}$ and ΔI non–linear function of the light power.

In order to find out which of the above effects gives rise to the current increase in tunnel junctions we varied the gap width s. We opened and closed the contact repeatedly while measuring I and ΔI. The result for red pulsed light is presented in Fig. 4.19. Clearly, we find $\frac{\Delta I}{I}$ = constant. The same relation was found for blue pulsed and red CW light. In addition, the current increase depends linearly on the illumination power, see Fig. 4.17. Let's compare these findings with our expectations from above:

- $\Delta I \propto I$ and $\frac{\Delta I}{I}$ does not depend on the gap width s.
- the relation $\Delta I \propto I$ does not change when CW instead of pulsed light is used.
- ΔI seems to depend linearly on the illumination power.

Thus, we conclude thermal expansion of the leads gives rise to the measured current rise. How much do the tips expand?

$$\begin{aligned} \frac{\Delta I}{I} = \frac{1}{18} &\approx \frac{2\Delta s}{\hbar}\sqrt{2m\Phi} \\ \Rightarrow \qquad \Delta s &\approx \frac{\hbar\,\Delta I}{2I\sqrt{2m\Phi}} \\ &\approx 0.026 \text{ Å} \end{aligned} \tag{4.14}$$

From eq. (2.20) we can calculate the temperature rise ΔT that would lead to such an expansion:

$$\Delta T = \frac{\Delta s}{u \cdot \alpha_{\text{gold}}} \approx 0.2 \text{ K} \quad , \tag{4.15}$$

where we used $u = 915$ nm (cf. section 3.1.2) and $\alpha_{\text{gold}} = 13.9 \cdot 10^{-6} \frac{1}{\text{K}}$ [57]. Note, both u and Δs used in the above formula have relatively high measurement errors.
The temperature rise of 0.2 K is consistent with the thermal properties of the sample stated in section 3.1.4. The focus FWHM of the light focus (~ 100 μm) is larger than the parallel heat transport length $x_0 \approx 32$ μm from eq. (3.7) on page 28, hence we will use the model "the sample is heated over a very broad region" (see page 29). The heat flow is predominantly perpendicular to the sample surface and the metal sheet is used as cold heat reservoir. The heat flux $\dot{q} = \gamma \cdot N$ on the gold bridge can be calculated from the absorption coefficient $\gamma \approx 2\,\%$ [120] of gold at 800 nm and the incident light power P. The light intensity N in the center of the spot as a function of $P = 2$ mW and the FWHM $d_0 = 110$ μm of the light focus (red light) is given by eq. (3.12 on page 45). We obtain:

$$\dot{q} = 2\gamma \cdot \frac{P \ln 2}{\pi\, d_0^2} = \frac{2 \cdot 0.02 \cdot 2 \cdot 10^{-3} \ln 2}{\pi \cdot (110)^2 \cdot 10^{-12}} \ \frac{\text{W}}{\text{m}^2} = 1460 \ \frac{\text{W}}{\text{m}^2} \quad . \tag{4.16}$$

The inclination angle of the light to the sample surface normal is 5°. Hence, the bridge is actually illuminated from above *and from below* by reflection on the polished steel substrate.[5] This is accounted for by introducing an additional factor of 2 in eq. 4.16. The temperature increase is then given by $\Delta T = \dot{Q} \cdot R = \dot{q} \cdot \hat{R}$ (cf. eq (3.8)), where $\hat{R} \approx 5 \cdot 10^{-5} \ \frac{\text{K}\cdot\text{m}^2}{\text{W}}$ is the specific thermal contact resistance of the interface. Thus,

$$\Delta T = 0.07 \text{ K} \quad . \tag{4.17}$$

The value for ΔT is smaller than the one calculated from the expansion of the bridge, eq. (4.15). This is expected because the specific thermal contact resistance of the sample is probabely a bit higher than $5 \cdot 10^{-5} \ \frac{\text{K}\cdot\text{m}^2}{\text{W}}$, a value measured on an industrially fabricated chip which was optimized for thermal conduction.

[5] The thickness of the PI layer is 4 μm. Hence, geometrical optics is applicable.

We can calculate an upper bound for ΔT by a method which is independent of the thermal conduction properties of the sample. The exponential response time of our current measurement is $\tau \approx 0.12$ ms (cf. section 4.3.1). We assume that the steady state increased current is reached faster than $\Delta t \approx 2\tau = 0.24$ ms. The thermal energy E deposited on the bridge during this time is (for $\dot{q}$ see eq. (4.16))

$$E = \dot{q} \cdot A_{\text{bridge}} \cdot \Delta t \approx 4 \cdot 10^{-10}\ \text{W} \cdot 0.24\ \text{ms} = 9.6 \cdot 10^{-14}\ \text{J} \quad , \tag{4.18}$$

where $A_{\text{bridge}} \approx 2.77 \cdot 10^{-13}\ \text{m}^2$ is the surface of the bridge.
Now we need the heat capacity C of the bridge. It can be deduced from the specific heat $c = 129\ \frac{\text{J}}{\text{kg K}}$ of gold [89], the volume of the bridge $V = A_{\text{bridge}} \cdot 50$ nm, and the density of gold $\rho = 19.3\ \frac{\text{g}}{\text{cm}^3}$ [89]:

$$C = c \cdot \rho \cdot V \approx 3.5 \cdot 10^{-14}\ \frac{\text{J}}{\text{K}} \quad . \tag{4.19}$$

The upper bound is then

$$\Delta T \leq \frac{E}{C} \approx 2.8\ \text{K} \quad . \tag{4.20}$$

Thus, the light-induced thermal expansion of the junction electrodes is consistent with the thermal transport properties of the sample. The absorption coefficient of gold, γ, for blue light is about an order of magnitude higher than for red light ($\gamma_{\,400\text{ nm}} = 60$ % and $\gamma_{\,800\text{ nm}} = 2$ % [120]). Hence, the increased response of the light-induced current to blue light can also be explained by the thermal expansion model.

4.3.3 Conductance Enhancement for Molecular Contacts

The general behavior of molecular contacts is very similar to that of tunnel contacts. The dominating feature is a light-induced current increase proportional to the current. This increase is independent of the light modus used (CW or pulsed) and the response for blue light is roughly an order of magnitude higher than for red light. For a contact comprising the anthracene molecule, the response to blue light also is higher than for red light. But this cannot unambiguously be identified as influence of the chromophore (the anthracene moiety), because the same behavior is found for all molecular contacts.
Unfortunately, the thermal expansion model cannot explain these findings for molecular contacts for the following reason: According to the thermal expansion model, the electrodes are heated up during the illumination and expand. The gap is thereby reduced by Δs. The measured quantity in the experiment is the current increase ΔI. Hence, what we actually measure is the derivative of the current I with respect to the gap width s: $\frac{dI}{ds}$. To our understanding, a basic feature of molecular contacts is the conductance plateau described in section 3.5. We actually use this plateau as a criterion when the molecular contact is established. Hence, we would expect $\frac{dI}{ds} \approx 0$ for molecular contacts. Thus, two "methods" to close the contact (heating with light and manually by turning the motor) lead to different behavior of $\frac{dI}{ds}$. What are the differences between these two "methods"?

1. Different timescales: the expansion of the leads caused by illumination takes place on a timescale of tenths of milliseconds, thus the closing speed is roughly 100 $\frac{\text{Å}}{\text{s}}$. The motor is approximately 1000 times slower. Usually we close contacts with a speed of 400–1000 $\frac{\text{steps}}{\text{s}} \approx 0.2\ \frac{\text{Å}}{\text{s}}$.

2. Light: another difference is of course the illumination. When building molecular contacts, no light is applied.

3. Accuracy: the light-induced current increase can be measured very exactly employing the lock-in amplifier technique because it is possible to chop the light. When we measure distance sweeps, the DC current is directly measured to a much lower accuracy and with a largely increased noise. Hence, we might not detect a small increase of the current on a current plateau even if it were present.

One possibility to explain the discrepancy are relaxation processes which are slow against the chopper period but fast with respect to the electrode movement when using the motor. Chopper periods are roughly 3 ms and the time resolution of the current measurement when building the molecular contact is 250 ms.
Another scenario would be that of multiple current paths. The molecules are relatively short. If we treat them merely as a spacer in between gold leads, still a measurable DC current can flow. Such behavior is, e.g., seen for alkane chains [121]. As a crude approximation, the Simmons formula, eq. (2.11), can be used to estimate the conductance of such a system. For a barrier of 5 Å width and 3 eV height, the zero-bias conductance then amounts to 1.3 nS. This is of the same order of magnitude as the conductance of many of our molecular contacts. For all of these findings, the molecule has seemingly no influence on the light-induced currents. In the following, we will discuss results, where there is a qualitative influence of the molecule.

Abrupt changes in the relation $\Delta I \propto I$ for molecular contacts

The proportionality factor in the relation $\Delta I \propto I$ depends on the microscopic configuration of the contact. $\frac{\Delta I}{I}$ is locally constant over a range of several 1000 steps (this corresponds roughly to 0.3 Å) but changes its value several times during the experiments. This is presented in Fig. 4.20, where a distance sweep for a contact comprising the anthracene molecule is shown. During the measurement $\frac{\Delta I}{I}$ discretely changes its value from 1 % to 0.6 %, to 0.2 %, and finally to 0.3 %. Abrupt changes in I can be (see, e.g., at 23 k steps), but are not always (see, e.g., at 43 k steps), accompanied by abrupt changes of $\frac{\Delta I}{I}$. This discrete behavior of $\frac{\Delta I}{I}$ is not observed for tunnel contacts, see Fig. 4.19. Thus, the light-induced signal *depends on details of the molecular contact configuration.*

4.3.4 Symmetry Properties of the Light Enhanced Current

What happens when an asymmetric molecular contact is illuminated? The IV of contacts with asymmetric molecules is always asymmetric with respect to voltage inversion [29, 98, 99, 115, 122]. In Fig. 4.21 we present a measurement of ΔI and I performed on a contact comprising the asymmetric molecule. To point out the asymmetry, we show the absolute values of the IV (solid lines) and $\Delta I(V)$ (dashed lines). The asymmetry of the IV is clearly visible but *not* reflected in the light-induced current enhancement. This measurement supports the hypothesis of different current paths, discussed above. One current path could lead to the asymmetric molecular IV and the other could be amplified by the illumination.
So far, we presented only the most prominent feature measured when light was applied to our contacts: a light-induced current increase. In addition, we found a light-induced current offset, which we present in the next section.

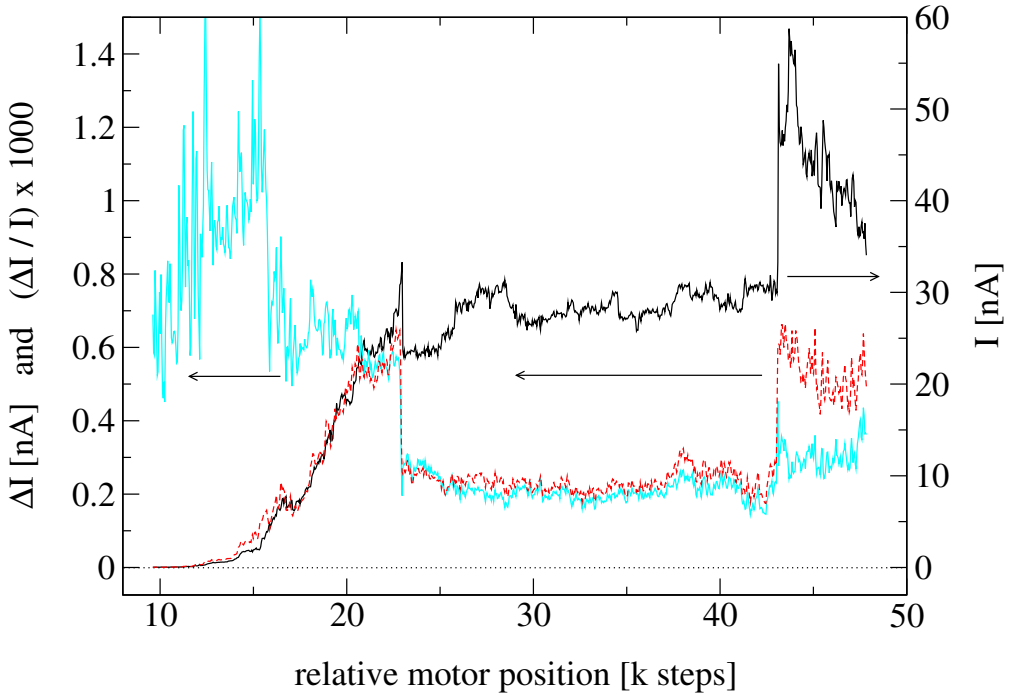

Figure 4.20: *Distance sweep of an illuminated junction with the anthracene molecule. Solid black: the DC current I, dashed red: light-induced current increase ΔI, and solid light blue: $1000 \cdot \frac{\Delta I}{I}$. $\frac{\Delta I}{I}$ is locally constant over a range of several 1000 steps (this corresponds roughly to 0.3 Å) but discretely changes its value from 1 % to 0.6 % at 16 k steps, to 0.2 % at 23 k steps, and finally to 0.3 % at 43 k steps. Abrupt changes in I can be (see, e.g., at 23 k steps), but are not always (see, e.g., at 43 k steps), accompanied by abrupt changes of $\frac{\Delta I}{I}$. Light: 8 mW, 800 nm, pulsed. Sample–id: W107C17S2.*

4.3.5 Light Induced Current Offset

In Fig. 4.22 we show the absolute value $|I(V)|$ of the DC current of a tunnel contact (black circles) and $|\Delta I(V)|$ (red squares). Closely looking at the data reveals a current offset I_O. $|\Delta I(V)|$ is shifted to the left with respect to $|I(V)|$. For this measurement, $I_O = 7.4$ pA.
The dependence of the light-induced current offset on the illumination power was measured for the same sample whose data is presented in Fig. 4.22. The measurement is presented in Fig. 4.23. For 800 nm illumination, the dependence is predominantly linear.
The current offset I_O for all samples where it could—at least partially—be evaluated is presented in table 4.1 for tunnel and table 4.2 for molecular contacts. In general, the values show wide scattering in magnitude and sign.

Current offset of the anthracene molecule

A special case for the current offset was seen on a contact comprising the anthracene molecule: The current offset had an opposing sign for blue and red light. To ensure that the contact did not change while recording the data, we employed the following algorithm: (i) measure an IV while illuminating with red pulsed light. (ii) measure an IV without illumination. (iii) measure an IV while illuminating with blue pulsed light. This cycle was looped five times

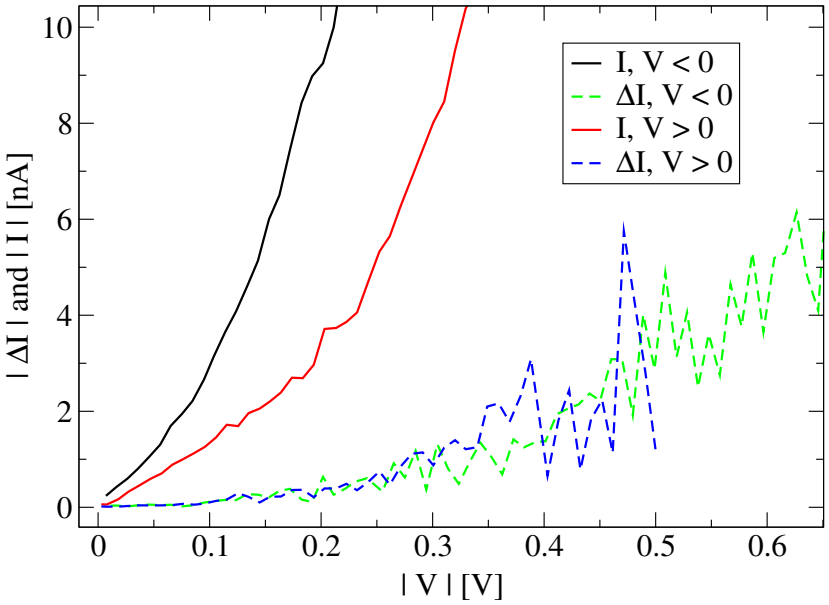

Figure 4.21: *Absolute value of the DC current $|I|$ (solid) and current increase $|\Delta I|$ (dashed) as a function of the voltage. The expected asymmetry of $I(V)$ with respect to V is clearly visible but $\Delta I(V)$ is* symmetric. *The data is an average of several consecutive voltage sweeps. Light power: 8 mW, 800 nm, CW. Sample-id: W107C24*

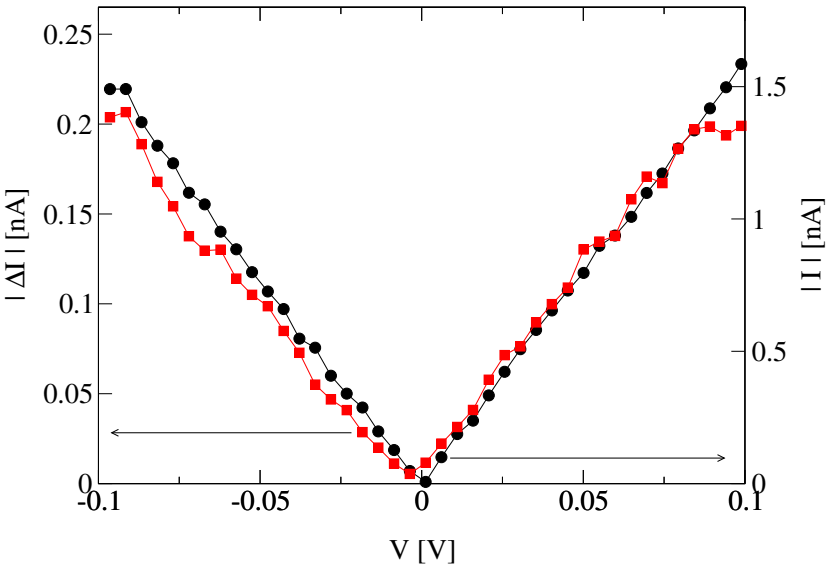

Figure 4.22: *Absolute value of the DC current $|I|$ (black circles) and $|\Delta I|$ (red squares) as a function of the voltage applied to a tunnel contact. $|\Delta I(V)|$ is shifted to the left with respect to $|I(V)|$, revealing a current offset. Incident light: 20 mW, 800 nm, pulsed. Sample–id: W107C17S2. The data is the same as in Fig. 4.15.*

and the respective average of the IVs calculated. The resulting IVs $|I(V)|$ and $|\Delta I(V)|$ are presented in Fig. 4.24. The light-induced current offset clearly depends on the wavelength.

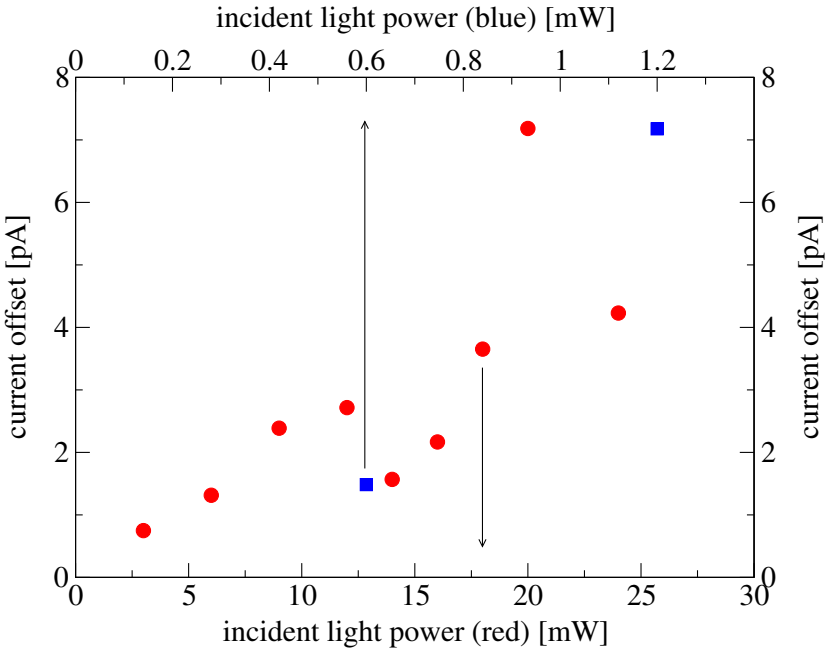

Figure 4.23: *Illumination power dependence of the light-induced current offset for 800 nm (red dots, lower x-axis) and 400 nm (blue squares, upper x-axis). The data for 800 nm indicate a linear dependence. Sample–id: W107C17S2.*

Sample–id	λ [nm]	P [mW]	I_O direction	$\lvert I_O \rvert$ [pA]
W107C07S1	800	16	(+)	/
W107C12S1	800	/	–	2.9
W107C13S1	800	/	–	13.3
W107C17S2	800	6	–	2.7
W107C23S2	400	0.4	/	/

Table 4.1: *Measurement statistics of the light-induced current offset I_O of the five tunnel contacts of which IVs under illumination were recorded. The symbols signify: +: same direction as positive bias, − opposite direction as positive bias, and /: could not be measured or was not recorded. Brackets signify a high measurement error.*

In solution, the molecule absorbs light at a wavelength of (394 ± 4) nm, and this is attributed to the anthracene moiety, see section 3.2.2. Thus, the wavelength-dependence of the light-induced current offset may stem from an influence of the chromophore.

Model to explain the current offset

Let us reflect again the criteria defined in section 4.3.1 (see page 68) for the different interaction mechanisms that could lead to a current increase in tunnel contacts. The findings for the current offset are consistent with the interpretation that they originate from excited electrons in the leads: Magnitude and sign of the signal are seemingly independent of the DC current. To test this hypothesis, we will calculate the quantum efficiency necessary to explain the magnitude of the current offset.

Sample–id	molecule	λ [nm]	P [mW]	I_O direction	$\lvert I_O \rvert$ [pA]
W107C09S1	biphenyl molecule	800	/	(+)	/
W107C11S2	biphenyl molecule	800	/	(+)	6.2
W107C11S2	biphenyl molecule	800	/	−	130
W107C13S1	biphenyl molecule	800	/	−	1.9
W107C08S1	anthracene molecule	800	/	(0)	/
W107C17S2	anthracene molecule	400	0.1	+	7.1
W107C17S2	anthracene molecule	800	0.4	−	7.1
W107C24S2	asymmetric molecule	400	2	0	0
W107C24S2	asymmetric molecule	800 (CW)	5	(−)	/
W107C24S2	asymmetric molecule	800 (CW)	2	/	/
W107C24S2	asymmetric molecule	800 (CW)	24	0	0
W106C08S1	asymmetric molecule	800 (CW)	8	0	0

Table 4.2: *Measurement statistics of the light-induced current offset I_O of the seven molecular contacts of which IVs under illumination were recorded. The symbols signify: +: same direction as positive bias, − opposite direction as positive bias, 0: no current offset, and /: could not be measured or was not recorded. Brackets signify a high measurement error. The two values for the contact 'W107C11S2' (2^{nd} and 3^{rd} line) were recorded on two consecutive days. The contact was closed up to metallic contact in between the measurements and the form of the electrode tips could have changed in the process. This might explain the large difference in $\lvert I_O \rvert$ of the two measurements.*

Quantum efficiency calculation

If the current offset is a result of excited electrons in the leads, we can calculate a lower bound of the quantum efficiency of the whole process, i.e. how many tunneling electrons are created per incident photon. We will present the calculation for the data shown in Fig. 4.22. The chopper frequency during this measurement was 1360 Hz, thus the light-on period was $\Delta t = 0.37$ ms. The relaxation time of bulk gold electrons is about $\tau \approx 10$ fs [64, 79]. Their velocity is roughly the Fermi velocity of electrons in gold, $v_F = 1.4 \cdot 10^6 \ \frac{\mathrm{m}}{\mathrm{s}}$ [64]. Thus, only electrons excited closer than $\approx$ 10–20 nm to the contact can contribute to the current, i.e. they all originate from an illuminated area of approximately $A \approx (15 \text{ nm})^2 = 2.3 \cdot 10^{-16}$ m^2. In the best case, they are all excited on one side of the contact and about half of them will move in the direction of the gap. The illumination power in the experiment was $P = 20$ mW. From eq. (3.12) we get the intensity N in the center of the spot:

$$N = 3.6 \cdot 10^5 \ \frac{\mathrm{W}}{\mathrm{m}^2} = 3.6 \cdot 10^9 \ \frac{\mathrm{W}}{\mathrm{cm}^2} \quad .$$

The upper bound Z_γ of incident photons of energy $E_\gamma = \frac{hc}{800 \text{ nm}} \approx 2.5 \cdot 10^{-19}$ J per chopper period $2\Delta t$ then is:

$$Z_\gamma = \frac{1}{2} \cdot \frac{N \Delta t \, A}{E_\gamma} \approx 6.2 \cdot 10^4 \tag{4.21}$$

The corresponding number of electrons Z_e that constitute the current offset I_O is

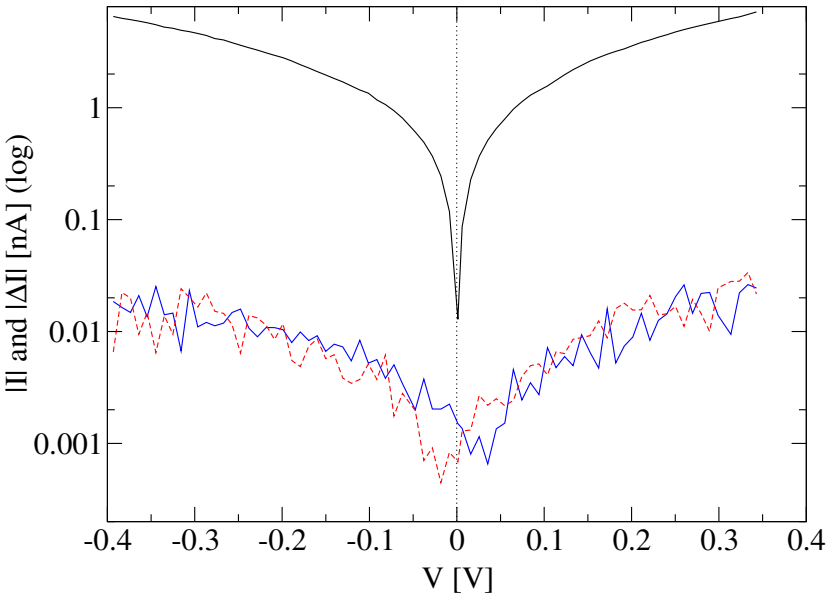

Figure 4.24: *Absolute value of the DC current $|I|$ (solid black) and the light-induced current increase $|\Delta I|$ as a function of the voltage V of a contact comprising the anthracene molecule for red (dashed red) and blue (solid blue) light. $|I|$ and $|\Delta I|$ are presented on the same logarithmic scale. The current offset $|\Delta I(V)|$ shifts in different directions for red and blue light. Light: 100 μW (blue), 400 μW (red), pulsed. Sample–id: W107C17S2.*

$$Z_e = \frac{I_O \, 2\Delta t}{e} \approx 3.4 \cdot 10^4 \quad . \tag{4.22}$$

We obtain

$$\frac{Z_e}{Z_\gamma} \approx \frac{1}{8} \quad . \tag{4.23}$$

If we take into account that a maximally excited electron still has to tunnel through a barrier of approximately $\Phi \approx 4.8$ eV $- 1.5$ eV height—the tunneling probability according to eq. (2.4) for an excited particle of energy $E_F + 1.5$ eV ≈ 7 eV through a rectangular barrier of 3.3 eV height and 1 nm width is on the order of 10^{-8}—, the quantum yield is by many orders of magnitude too high. In [79] a value of $3 \cdot 10^{-10}$ is calculated from a measurement given in [123] for red light incident on a ($Al/Al_2O_3/Au$) contact.
Thus, the origin of the current offset remains unclear and a measurement error cannot be excluded. But a systematic error is improbable for two reasons. (i) The values for the current offset show wide scatter. (ii) For the measurement on the contact comprising the anthracene molecule, the current offset changed when *only* the light parameters were varied.

Electromigrated contacts

To further test the thermal expansion model, we structured planar electromigration contacts on a glass substrate. These contacts [107, 124] consist of planar electrodes which are entirely connected to the substrate. The interaction of these contacts with light was studied by Daniel Wolpert in the Würzburg group as diploma thesis [125]. Indeed the thermal expansion of the

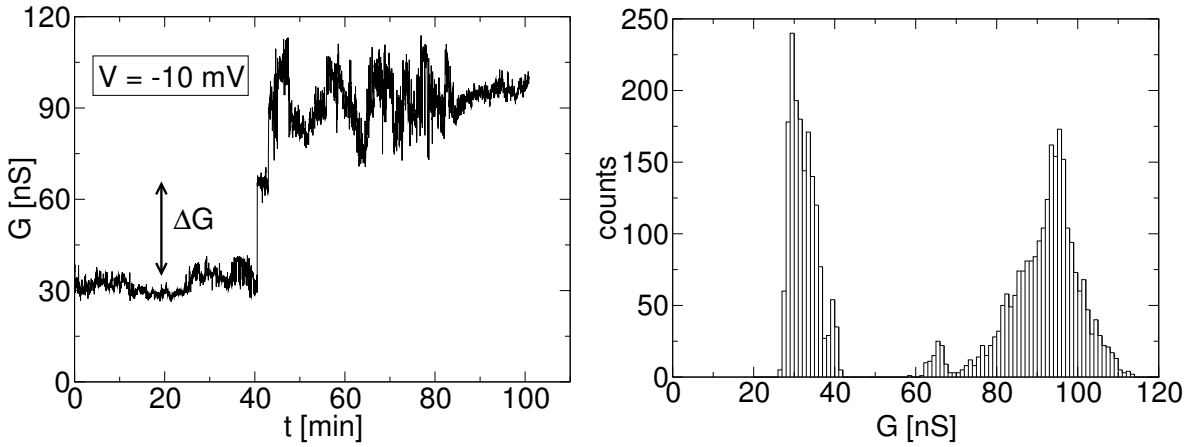

Figure 4.25: *Long-term low-bias conductance of a molecular contact of the anthracene molecule (left-hand side) and the conductance histogram of the measurement (right-hand side). The conductance is first relatively stable at 30 nS, then jumps to roughly 65 nS and shortly afterwards to 95 nS. Then, after a period of increased noise, the conductance stabilizes at approximately 95 nS. The expected peaks at approximately 30, 65 and 95 nS are well visible in the histogram. Sample–id: W107C17S2.*

electrodes was sufficiently suppressed. In his work, D. Wolpert could identify a light-induced current increase which was attributed to a two-photon excitation process.

4.4 Discrete Conductance Switching

In this work, we measure the conductance of a molecular contact for a very long time at a low bias voltage. Such measurements can be performed for several days. Prior to the measurement, the quality of the molecular contact is verified by measuring reproducible current–voltage characteristics (IVs). We address this type of measurement as *long-term low-bias conduction*.

4.4.1 Stochastic Switching in the Long-Term Low-Bias Conduction

When measuring the long-term low-bias conductance of a molecular contact, switching behavior is often observed. An example of such a measurement, performed on a contact to which the anthracene molecule had been applied, is presented on the left-hand side in Fig. 4.25. The conductance is first relatively stable at 30 nS, then jumps to a value sightly above 60 nS and shortly thereafter jumps again to approximately 95 nS. The amplitude of these two jumps is roughly the same. After the second jump, the conductance shows strong noise but finally the noise decreases towards the end of the measurement. Stochastic discrete switching behavior of molecular contacts has already been reported by other groups in STM experiments:

- Donhauser et al. [6] investigated the conductance of conjugated organic monothiols protruding from an alkane–monothiol SAM with an STM. They report on two distinct conductive states of the molecules. The molecules in the "off" state (low conductance) can still be seen. Hence, the "on" and "off" states are really measured on the same molecule. Disorder of the alkane SAM strongly enhances the switching activity.

- Ramachandran et al. [9] used an STM to study the conductance of small conjugated organic dithiols protruding from an alkane–monothiol SAM — the main difference to [6] is the use of dithiols instead of monothiols. They observe stochastic switching between a low and a high conducting state and find strong indications, that this can be attributed to breaking and establishing of the bond to the underlying gold. The measurements were performed in solution.

- Wassel et al. [126] measured the conductance through monothiol alkane chains whose opposite terminal group was either a forrocenyl- or viologen–complex. They were embedded in a monothiol alkane matrix on a gold surface. Switching was observed as above and the different two classes of molecules behaved in a similar manner.

- Xu et al. [10] did not directly measure stochastic switching. They measured the conductance of an STM-junction that was repeatedly opened and closed in a molecular solution. Histograms of these conduction measurements show equidistant peaks which were interpreted as the conductance of single molecules.

- Reichert [115] observed switching behavior between two different relatively stable IVs.

To analyze the amplitude of the fluctuations, we calculated a conductance histogram of the measurement, presented on the right-hand side in Fig. 4.25. The conductance was divided into 100 bins from 20 to 120 nS, and the number of data points in every bin counted. After this measurement, IVs were recorded and the contact was opened. Then the molecular contact was established anew. The subsequent long-term low-bias conductance measurement and the histogram calculated from it is presented in Fig. 4.26. Towards the end of the conductance measurement, the switching behavior is particularly well visible. The amplitude of the fluctuations is the same as in Fig. 4.25. Then the contact was again opened and closed and the long-term low-bias conduction measured. This measurement and its histogram are presented in Fig. 4.27.
The histograms of all three measurements are presented in one plot in Fig. 4.28. All of the histograms have common peaks and altogether equidistant peaks can be labeled from one to three and six. The amplitude of the conductance fluctuations is 30–35 nS.
The number of equidistant peaks that can be labeled in the conductance histograms is up to six in the measurement presented. In addition, the switching amplitude is independent of the actual conductance of the junction (see Figs 4.25 through 4.27). This suggests that something which is (i) stable and (ii) exists in many equal units carries the current in our molecular junctions. The molecules that have been applied to the junction are plausible candidates for these "units". Hence, we interpret the conductance fluctuations as single molecules breaking and establishing the chemical bond to one of the electrodes.
It is reasonable to ask whether equidistant conductance fluctuations like the ones just described are also present in contacts to which different molecules have been applied. We also found equidistant conductance fluctuations on a contact comprising the biphenyl molecule. The corresponding long-term low-bias measurement is presented in the upper left plot of Fig. 4.29. In the zoom shown on the lower left in the figure, the switching behavior is clearly visible. In the histogram presented on the lower right, three equidistant conductance peaks are well displayed. The switching amplitude for this measurement was $\Delta G \approx 6$ nS.
For a contact comprising the asymmetric molecule, we likewise found equidistant conductance fluctuations. The long-term low-bias conduction measurement and its respective histogram

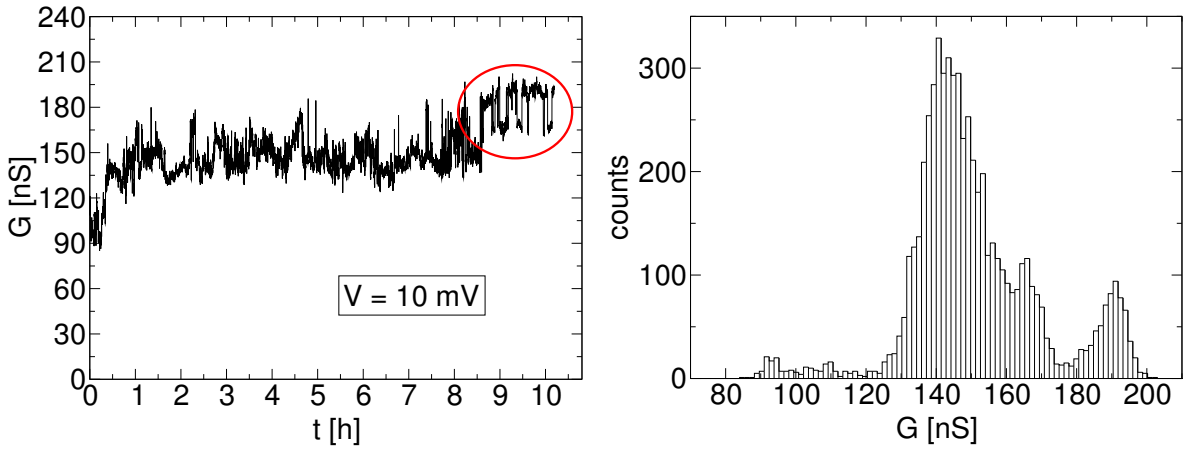

Figure 4.26: *Long-term low-bias conductance measurement on the same sample as in fig 4.25 after completely opening and closing the contact. Switching behavior is still present and the switching amplitude remains the same—best visible in the region indicated by the red ellipse. The histogram of the whole measurement is presented on the right-hand side. Sample–id: W107C17S2.*

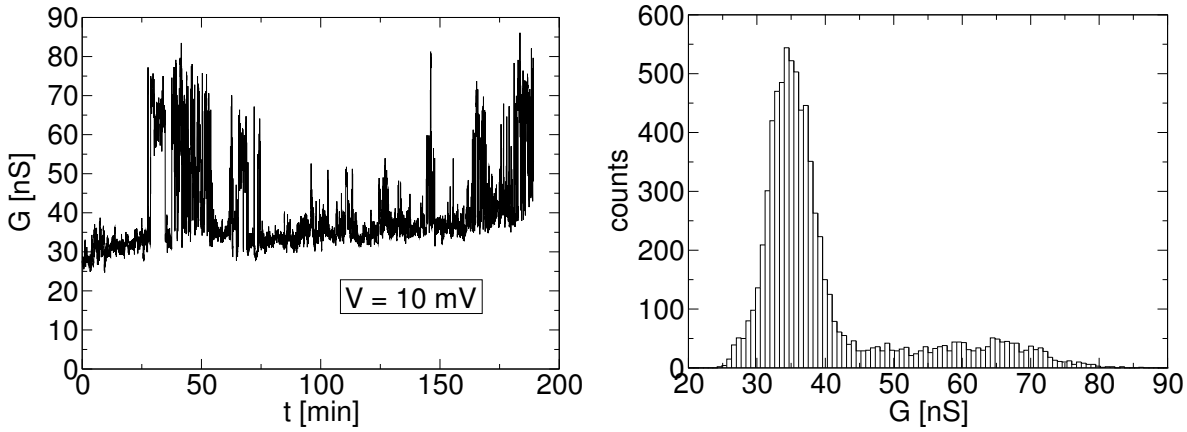

Figure 4.27: *Long-term low-bias conductance measurement on the same sample as in fig 4.25 after completely opening and closing the contact twice. Switching behavior is still present and the switching amplitude remains the same. The histogram of the whole measurement is presented on the right-hand side. Sample–id: W107C17S2.*

of the region of low conductance towards the end of the measurement are presented in Fig. 4.30. The data quality is slightly reduced compared to the other two molecular contacts presented above but the equidistant peaks are still visible in the histogram. For comparison, the histogram of the full conductance measurement is presented in Fig. 4.31. There, it is difficult to locate equidistant peaks.

We have presented several examples comprising different molecules where equidistant jumps in the long-term low-bias conductance have been measured. This is not the only method by which conductance steps can be identified. Next, we will present switching behavior in distance sweeps.

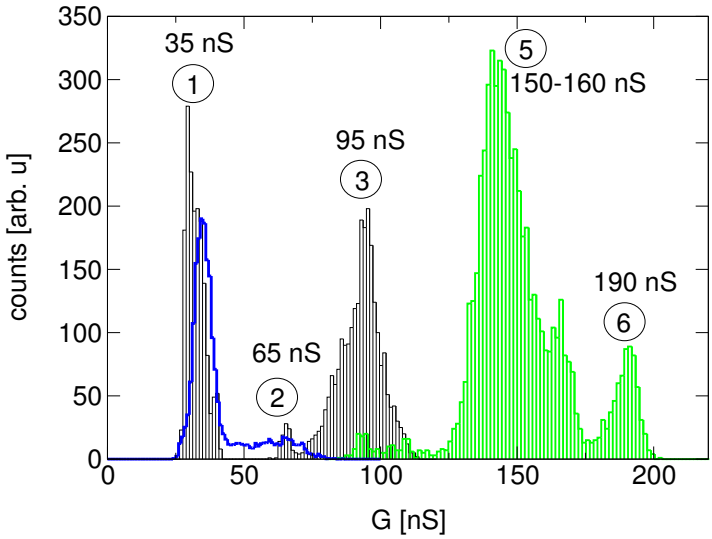

Figure 4.28: *Conductance histograms of three different long-term low-bias measurements performed on the same sample. In black: from Fig. 4.25; in green: from Fig. 4.26; in blue: from Fig. 4.27. The contact was completely opened and closed between the respective measurements. The equidistant conductance peaks can be labeled up to a number of six. All measurements were performed at + or − 10 mV. Sample–id: W107C17S2.*

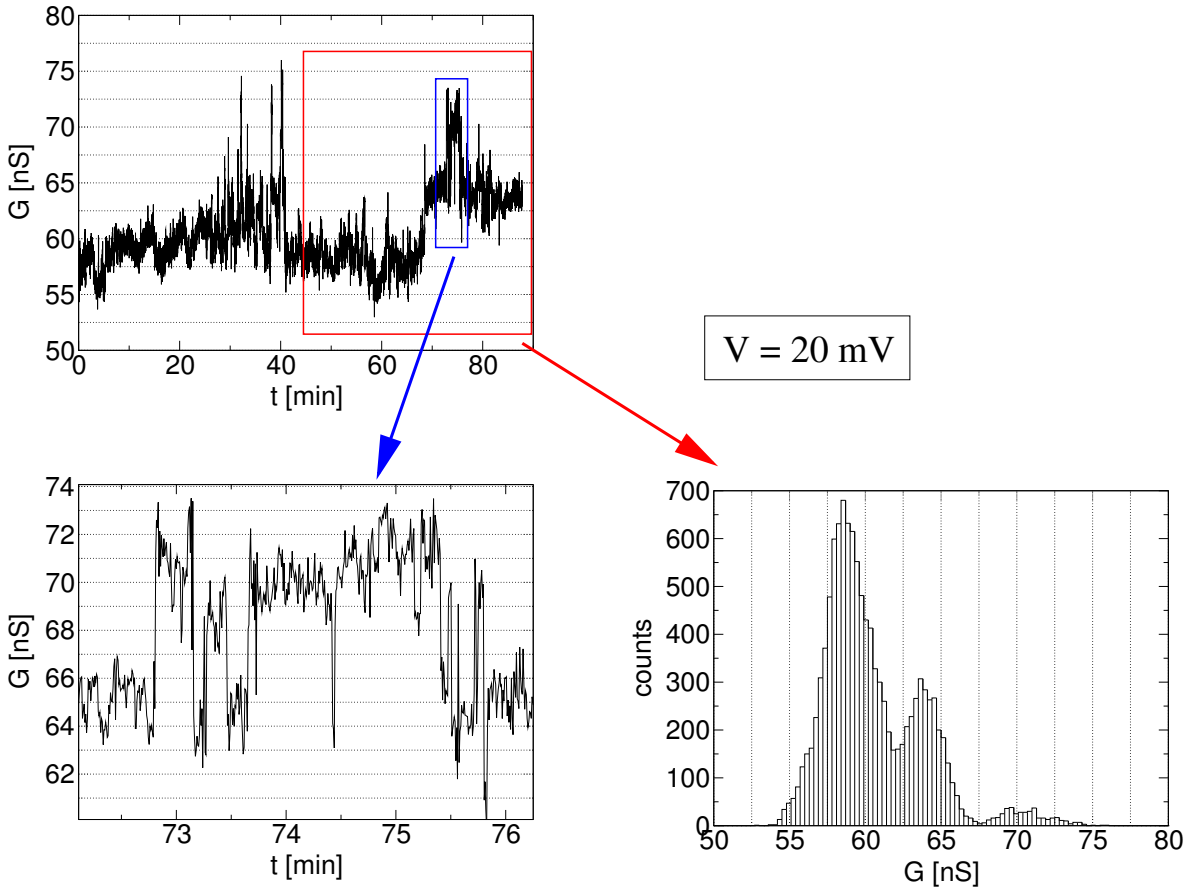

Figure 4.29: *Long-term low-bias conductance of a contact comprising the biphenyl molecule. The conductance measurement is presented in the upper-left viewgraph. After the contact has calmed down, switching events are clearly visible (see lower-left viewgraph). A histogram of the second half of the conductance measurement is presented in the lower-right viewgraph, revealing three very clear equidistant conductance peaks. Sample–id: W107C11S2.*

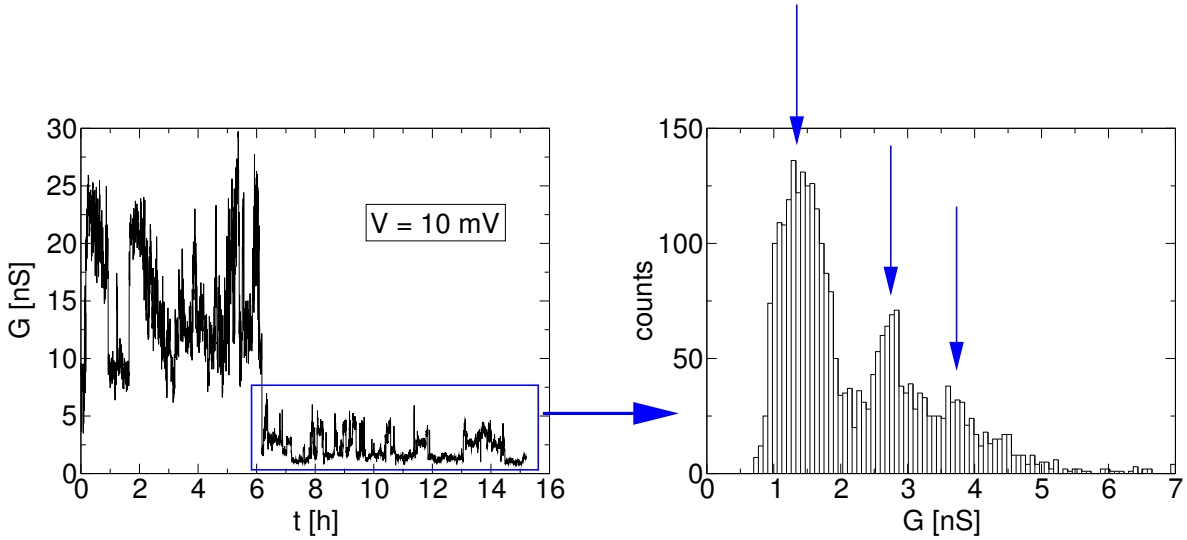

Figure 4.30: *Long-term low-bias conductance of a contact comprising the asymmetric molecule (left-hand side). After 6 hours, the noise of the contact has reduced and equidistant peaks are visible in the conductance histogram presented on the right-hand side. Sample-id: W107C24S2.*

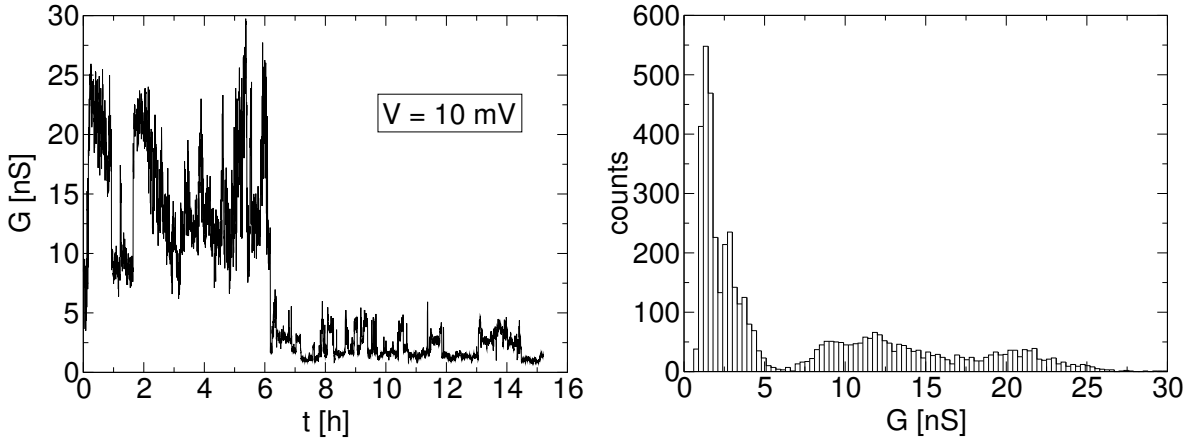

Figure 4.31: *Histogram of the entire measurement presented in Fig. 4.30 for comparison. In this histogram it is difficult to locate equidistant peaks. Sample-id: W107C24S2.*

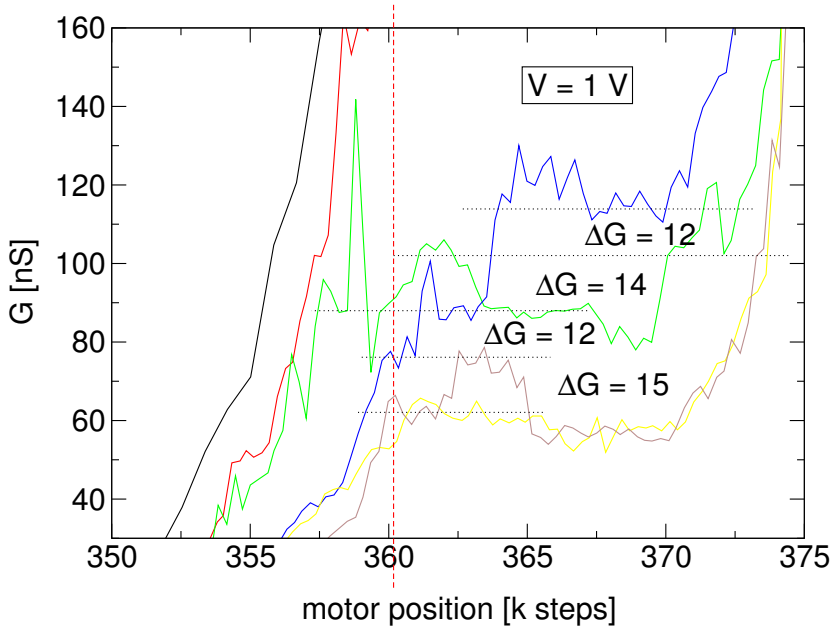

Figure 4.32: *Closing distance sweeps of the same contact as in Fig. 4.29 comprising the biphenyl molecule. Several consecutive sweeps are displayed in different colors. The sweeps were recorded at a relatively high voltage, thus the signal is relatively noisy. Increased noise at high voltages is observed in most measurements on molecular contacts. Nevertheless, equidistant plateaus are visible, and their respective distance is approximately between 12 and 15 nS. Note, not for every sweep plateaus are observed, e.g. for the two first sweeps (black and red solid line). The dashed red line indicates the position where the data presented in Fig. 4.33 was recorded. Sample-id: W107C11S2.*

4.4.2 Switching in Distance Sweeps

Taking a closer look at a distance sweep of the contact to which the biphenyl molecule had been applied reveals approximately equidistant conductance plateaus. Several consecutive conductance measurements while closing the junction are presented in Fig. 4.32. Though not as clear as in the long-term low-bias conductance, equidistant plateaus are visible. The distance sweep was recorded at 1 V, hence the noise is considerably increased compared to measurements at low bias. This behavior is observed in most measurements on molecular contacts. The switching amplitude, roughly 13 nS, is higher than for the data presented in Fig. 4.29. This is expected, because the (non-linear) conductance of all contacts comprising the biphenyl molecule measured in this work increased with the applied voltage.
After the last distance sweep measurement, the contact was again closed and the motor stopped at the position indicated by the dashed red line in Fig. 4.32. Subsequently, we recorded IVs of the contact and found several discrete stable sets of IVs at this position.

4.4.3 Switching Between IVs

Switching behavior between two stable IVs is sometimes observed in molecular conductance experiments. Here, we present an example where five stable sets of IV characteristics have been measured by consecutively sweeping the bias voltage between +1 V and −1 V. The con-

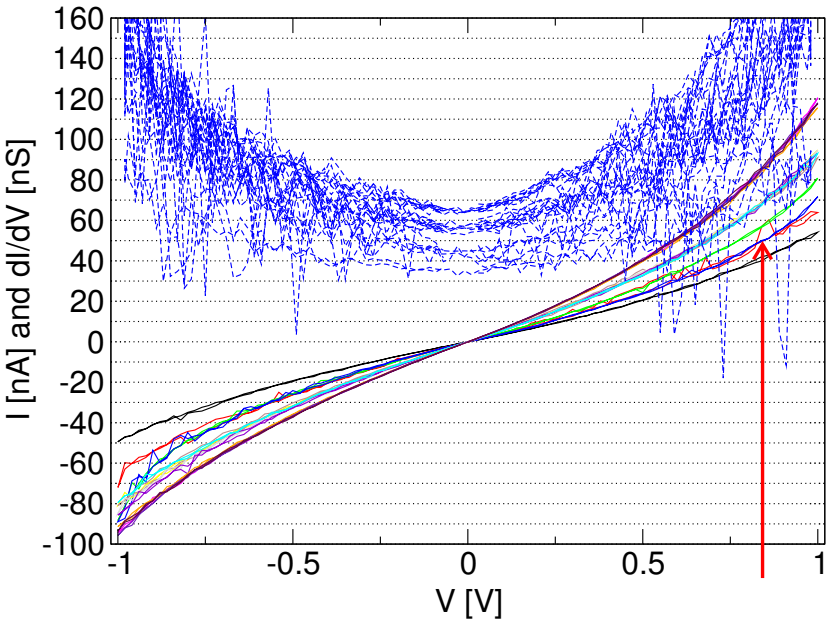

Figure 4.33: *Discrete sets of current–voltage characteristics of a contact with the biphenyl molecule. After having recorded the distance sweeps presented in Fig. 4.32, the motor was stopped (while closing the junction) at the position indicated by the red line in Fig. 4.32. Subsequently, IVs were recorded and are displayed in this figure. Several stable sets of curves are visible with different current amplitudes. Switching between these sets is observed, indicated by the red arrow. Sample-id: W107C11S2.*

tact is the same contact with the biphenyl molecule that has been described in the preceeding paragraphs. The IV characteristic of this contact, recorded at the motor position indicated by a red line in Fig. 4.32 is presented in Fig. 4.33. Five sets of stable IV characteristics are clearly discernible. The current can fluctuate between two stable sets of curves, indicated by the red arrow in the figure.

We will now compare the data of the biphenyl–contact just described with data recorded in a different setup and at low temperature.

4.4.4 Comparison with Data Recorded at Low Temperatures

In her Diploma Thesis [96], M. Di Leo measured IVs of a contact comprising the biphenyl molecule in our second MCBJ setup at a temperature of 40 ± 10 K. One of the IVs, possibly of a single-molecule contact, is presented in Fig. 4.34. The switching behavior observed in this work might be identified with single molecules locking into and unlocking from the contact. We will compare them with the IV characteristics shown in Fig. 4.34. The zero-bias conductance $G_0 = 6.5 \pm 0.5$ is in very good accordance to the low-bias switching amplitude deduced for the contact with the biphenyl molecule displayed in Fig. 4.29. Another quantity which can be compared, is the conductance $G = \frac{I}{V}$ (*not* $\frac{dI}{dV}$) of the contacts at 1 V. In the low-temperature IV, see Fig. 4.34, this conductance is 13 nS. This corresponds well to the vertical spacing of the plateaus in the distance sweep recorded at 1 V which are presented in Fig. 4.32. There, the deduced fluctuations are between 12 and 15 nS.

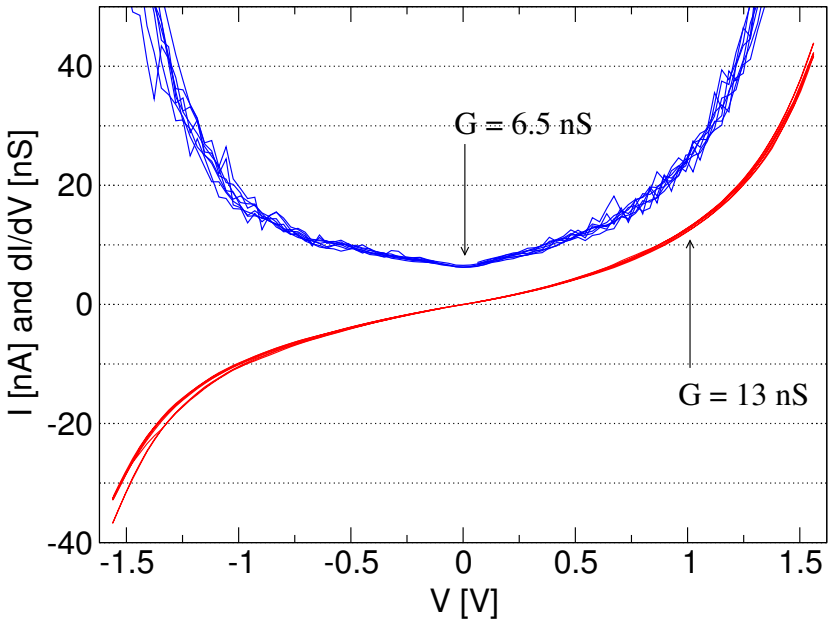

Figure 4.34: *Current–voltage characteristic of a contact with the biphenyl molecule measured at low temperatures in another setup. The IV was measured by M. Di Leo in 2002 [96] in our second MCBJ setup at a temperature of* 40 ± 10 *K. The zero-bias conductance* $G_0 = (6.5 \pm 0.5)$ *nS corresponds well to the low-bias fluctuation amplitude deduced in Fig. 4.29. In addition, the conductance* $G = \frac{I}{V} \approx 13$ *nS* (not $\frac{dI}{dV}$) *is in good accordance with the spacing between the conductance plateaus deduced in Fig. 4.32.*

Next, we will analyze the fluctuations between stable IVs displayed in Fig. 4.33. If the fluctuations in Fig. 4.33 can be identified with single molecules locking into and unlocking from the contact, the difference of the current between sets of curves in that figure should be of similar magnitude as the IV presented in Fig. 4.34. The current difference between the two lowest lying sets of curves in Fig. 4.33 and the IV of Fig. 4.34 are presented in one plot in Fig. 4.35. The IV obtained from subtracting the current is quite noisy but—especially for positive voltages—compares well to the low-temperature IV.

We observed conductance fluctuations whose amplitude were independent of the actual conductance of the molecular junction. In histograms of the long-term low-bias conductance measurements, these fluctuations can be identified as equidistant peaks. We interpret these as chemical bond fluctuations of molecules breaking and establishing the contact to one of the gold electrodes. For the biphenyl molecule, this interpretation is consistent with a former, presumably single-molecule, measurement performed in another MCBJ setup at low-temperature. This interpretation implies that we observed electrical transport through molecules in parallel and that the interaction between neighboring molecules in our contacts is weak.

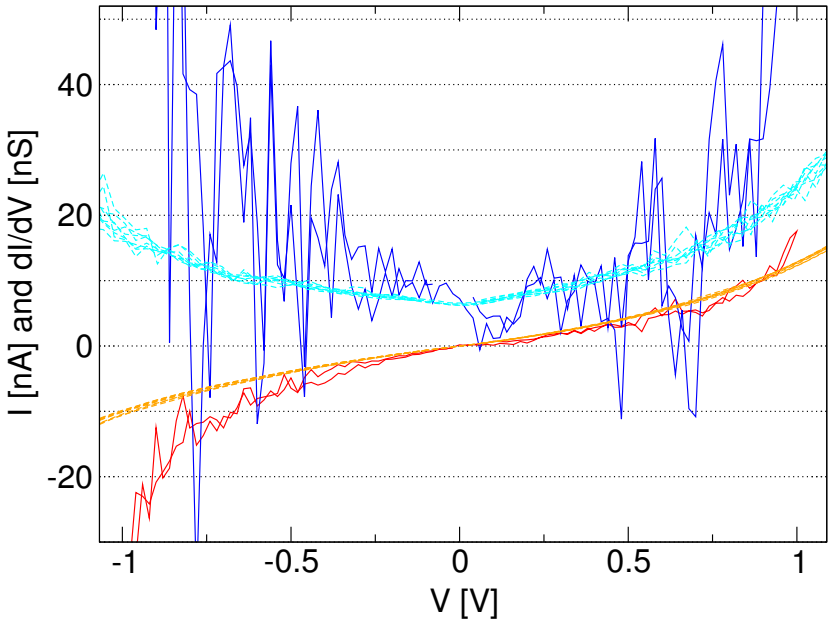

Figure 4.35: *Comparing the sets of stable current–voltage characteristics of Fig. 4.33 with a low-temperature measurement on a contact with the same molecule. The difference of the current of the two lowest lying sets of curves in Fig. 4.33 is presented in red. In blue, the 5 point running average of the numerically calculated* $\frac{dI}{dV}$ *of that curve is presented. For comparison, the IV and* $\frac{dI}{dV}$ *from Fig. 4.34 are shown in dashed orange and dashed light blue respectively. For positive bias voltage, the accordance is quite good. On the negative branch, the order of magnitude is well reproduced.*

4.5 Are we Measuring the Molecules?

How sure can we be that the current–voltage characteristics measured in mechanically-controlled break-junctions really represent the conductance of metal–molecule–metal contacts? There are several indications that this is indeed the case:

1. The conductance plateau and the reduced noise on those plateaus are an indication that we measure a stable configuration. We interpret this as a sign for a stable (covalent) chemical bond.

2. The maximum voltage that can be applied to a molecular contact (≈ 1.8 V) is roughly twice as high as for a gold tunnel contact (≈ 1 V) of comparable conductance. This shows again the stability of the molecular junctions.

3. Of the molecular contacts in this work, reproducible IVs can be recorded for very long periods of time. If the maximum voltage is low enough($\approx \pm 0.8$ V) this can be done up to at least an hour. This also proves the stability of the contact and indicates a covalent chemical bond. Measurements on unbound molecules are a lot more difficult to perform and very unstable [7].

4. Our measurements reproduce the symmetry properties of the molecule. Molecules exhibiting a permanent electric dipole along their axis always lead to contacts exhibiting asymmetric IV characteristics. Molecules which are symmetric with respect to a mirror plane perpendicular to the axis defined by the sulphur atoms usually lead to relatively symmetric IVs. Slight asymmetries can have several reasons, e.g., by asymmetric coupling to the electrodes or an asymmetrical polarizability of the souroundings of the molecular junction. For a more detailed description of effects leading to slight asymmetries, see section 2.4.3 on page 14.

5. The asymmetry is not the only symmetry property reflected in the molecular measurements. By steric hindrance due to methyl-substituents, the electronic overlap between neighboring phenyl rings can be greatly reduced. This was used to design a molecule that was expected to lead to IVs resembling those of a tunnel contact: the biphenyl molecule, described in section 3.2.1 on page 29. As anticipated, the IV characteristics of molecular contacts of this molecule almost always resembled IVs expected for tunneling contacts.

6. We observed conductance fluctuations of a fixed value, independent of the actual conductance in the long-term low-bias conductance of molecular junctions. In conductance histograms of these measurements, equidistant peaks are visible. The molecules are plausible candidates as the conducting moiety in these junctions.

7. Recently, M. Koentopp [43, 98] was able to predict 7 out of 9 bias voltage positions at which current steps were observed in a low temperature IV measurement performed by R. Ochs on a contact comprising the asymmetric molecule [98,99]. The DFT-calculation employed for the calculation was a full ab initio method, i.e. it had no adjustable parameters.

Chapter 5

Conclusions and Outlook

In this work, we have attempted to further analyze molecular conductance with mechanically-controlled break-junctions (MCBJs) by a variety of techniques.
The calibration of the electrode distance of gold MCBJs at room temperature has so far not been accomplished to a satisfactory degree of accuracy. The reason for this is that most methods characterizing tunnel junctions employ voltages above the tunnel barrier-height. For gold contacts, this is experimentally not possible at room temperature because the tunnel contacts are instable above roughly 1 V due to the strong surface diffusion. The two standard methods which can be employed to calibrate the distance of the electrodes are: (i) characterization of the tunneling gap using the low-bias conductance, and (ii) geometrical considerations of the MCBJ setup. The results of these two methods deviate considerably. We have investigated this discrepancy by comparing our findings with TEM and STM measurements reported in the literature, and could calibrate the electrode spacing for our setup. The distance calibration evaluated from tunneling conductance measurements was in agreement with these TEM and STM measurements. With this at hand it was possible to analyze the distance information of molecular MCBJ measurements.

A simple resistor network model describing the thermal transport in MCBJs, when these are heated either by illumination or by Joule heating due to the measurement current, has been tested by illuminating the contacts. The data are consistent with a relatively good thermal contact between the gold leads and the underlying layers. The thermal resistance for the heat transport away from the junction is thus roughly $2 \cdot 10^5 \ \frac{\mathrm{K}}{\mathrm{W}}$. It can now be estimated whether the Joule heating leads to the instabilities found at voltages above ~ 1.5 V when measuring molecular current–voltage characteristics. For molecular contacts of up to 1 MΩ resistance, a temperature increase of up to only ~ 1 K is estimated. This indicates that, in addition to Joule heating, other mechanisms contribute to the observed instabilities.

We found that molecules measured in a MCBJ setup exhibit discrete switching behavior of the long-term conductance. The switching amplitude was independent of the actual conductance of the junction, and in histograms we observed up to 6 equidistant conductance peaks. Discrete switching of molecular conductance was observed on molecular contacts of different molecular species and was found in various types of measurements, namely: (i) by measuring the conductance at low bias for a very long period of time (up to several days), (ii) by analyzing the conductance as a function of the electrode separation, and (iii)

by several discrete sets of curves in a current–voltage characteristic. We speculate that the observed behavior is induced by additional molecules locking into or unlocking from the contact. For the biphenyl molecule, this interpretation is consistent with former, presumably single-molecule, measurements performed by M. Di Leo at a temperature of roughly 40 K.

In collaboration with the group of Dr. W. Pfeiffer in Würzburg, we were able to measure the current response of tunneling and molecular mechanically-controlled break-junctions illuminated by ultrashort laser pulses. The junctions were very stable and the light-induced current signal could be measured to an accuracy thus far unreached in similar, e.g. STM, experiments.
We found a light-induced current increase proportional to the current on all tunnel and symmetrical-molecule contacts to be the dominating effect. It was of the order of several percent for light intensities in the range of $10^9 \frac{\mathrm{W}}{\mathrm{cm}^2}$. For tunnel contacts, the results can be explained by thermal expansion of the freestanding parts of the metal bridge due to heating by the light. For molecular contacts, the situation is less clear: The symmetry properties of an asymmetrical current–voltage characteristic are not reflected in the light-induced signal. In addition, molecular contacts are always measured on current plateaus. Hence, a current rise due to thermally expanding electrodes is not expected. The mechanism leading to the current increase of molecular contacts is thus unclear.
In addition to the—presumably thermally induced—linear current increase, we found a light-induced current offset for both tunnel and molecular contacts. This effect exhibited strong sample-to-sample fluctuations and was wavelength-dependent—in particular for a contact comprising the anthracene molecule which, in solution, absorbs blue light. There the sign of the current offset was different for red and blue light. This could indicate an influence of the chromophore of the molecule.

In this work, we provided new approaches to analyze the electronic transport through molecular contacts measured with mechanically-controlled break-junctions. Additionally, we analyzed the optical and thermal properties of these junctions. For a more in-depth analysis of the optical experiments a new setup is desirable where the diameter of the light focus can be controlled as well as the wavelength of the illumination. This can be accomplished by a "home-built optical microscope" where a lens mounted directly above the sample in the vacuum chamber is used as objective. The rest of the microscope can be mounted outside the vacuum chamber above the viewport. With such a setup focal diameters down to roughly 40 μm can be achieved. By using a white-light source and filters, the entire optical spectrum would be accessible. With such a setup the current response to the illumination as a function of the wavelength could be compared to the expected absorption of the gold tips. That way, the thermal expansion model could be verified in more detail. In addition, smaller foci offer the possibility to reduce the thermal load on a junction while keeping a constant density of incident photons on the junction. Thus the ratio of thermal to other optical effects could be reduced. By varying the focal size, the thermal resistance of the samples could be studied and verified in further detail. For example the crossover from the regime of local heating to heating over a broad region (described in section 3.1.4) could be studied. A small focus might also allow to measure thermoelectric effects.

A new type of break-junction aiming at reducing the thermal expansion was developed at the INT by R. Rick, M. Di Leo and H.B. Weber: mechanically-controlled break-junctions

where the gold wire is replaced by a three layered structure of roughly 50 nm SiO_2, 2 nm titanium and 12 nm gold. The mechanical stability is thus provided by the SiO_2 allowing for a very thin metal layer. This thin layer is more transparent for light, i.e. it will absorb less energy, and in addition, the thermal expansion of the bridge will presumably be dominated by that of SiO_2 which is much smaller than for gold.

A completely different direction for optical experiments is to investigate the electroluminescence of molecular junctions instead of the photo-conductivity that we have investigated here. Electroluminescence has been measured by several groups on metal tunnel contacts and also on molecular contacts [73, 127–129]. The "home-built optical microscope" described above can directly be used to measure electroluminescence provided a very sensitive detector is at hand.

For a verification of our proposal that the observed discrete conductance steps can be attributed to the room-temperature conductance of single molecules, better measurement statistics are desirable. The measurement of these conductance fluctuations can be automated in order to increase the time of data acquisition. In addition, the temperature dependence of the fluctuation rate could be analyzed and used to increase the rate of switching events in the experiment.
Similarly, with a higher number of measured samples one could verify to a higher accuracy whether the length of the molecules is reflected in the distance sweeps. This in turn provides another test for the distance calibration of mechanically-controlled gold break-junctions.

We wish to thank the Volkswagen Stiftung, the Center for Functional Nanostructures and the Forschungszentrum Karlsruhe for financial support.

Appendix A

Nomenclature Table

e	electron charge ($e < 0$)
$f()$	Fermi distribution function
l	a length
$\dot{q}$	heat flux in $[\frac{\mathrm{W}}{\mathrm{m}^2}]$
s	tunneling barrier width
u	freestanding length of the bridge
v	velocity
x, y, z	coordinates
A	area
E	energy
G	conductance
G_0	conductance quantum, $G_0 = \frac{2e^2}{h} \approx 77.5\ \mu\mathrm{S}$
I	electrical current
M	variable for the motor position readout in [steps].
N	intensity in the center of the laser focus in $[\frac{\mathrm{W}}{\mathrm{m}^2}]$
P	power
$\dot{Q}$	heat flow in [W], $\frac{\dot{Q}}{A} = \dot{q}$
R	electrical or thermal resistance
$\hat{R}$	specific thermal contact resistance
R	distance calibration factor in $[\frac{\mathrm{m}}{\mathrm{step}}]$
T	temperature
$\mathbf{T}$	transmission matrix
V	voltage
α	linear thermal expansion coefficient
ε	energy alignment point
λ	thermal conductivity in $[\frac{\mathrm{W}}{\mathrm{m}\cdot\mathrm{K}}]$
Φ	tunnel barrier height
ξ	conversion factor to convert motor positions into the pushing rod movement

Appendix B

Technical Terms of this Thesis

Some technical terms which are not common knowledge are defined explicitly in this thesis. They are listed the following table with the page on which they are defined.

Appendix C

Frequently used Abbreviations

AFM	Atomic Force Microscope
AOM	Acousto–Optical modulator
IV	Current–Voltage Characteristic
MCBJ	Mechanically-Controlled Break-Junction
MIM	Metal–Insulator–Metal
RIE	Reactive Ion Etching
SEM	Scanning Electron Microscope
STM	Scanning Tunneling Microscope
THF	Tetrahydrofurane
CW	Continuous Wave
DC	Direct Current

List of Figures

List of Tables

Danke

Sehr viele Personen haben zum Gelingen dieser Arbeit beigetragen. Ihnen allen gilt mein großer Dank. Prof. Heiko B. Weber danke ich für die Betreuung, seinen Einsatz und, dass er mir ermöglichte auf diesem sehr aktuellen und interessanten Thema zu promovieren. Prof. Hilbert von Löhneysen danke ich für die Unterstützung meiner Arbeit und die Möglichkeit bei ihm zu promovieren. Prof. Elmar Dormann danke ich für die Übernahme des Korreferats und sein Interesse an der Arbeit.

Mein besonderer Dank gilt Detlef („der Master“) Beckmann für seine unbezahlbare Unterstützung in messtechnischen und physikalischen Fragen, für die Messsoftware und für die Geduld. Ohne ihn wäre diese Arbeit nicht möglich gewesen.

Ganz herzlich möchte ich mich bei meiner Arbeitsgruppe bedanken. Michelle Di Leo, die mir vor allem gegen Ende der Arbeit unglaublich den Rücken frei gehalten hat und für die schöne Zeit im Büro, Daniel Secker für die moralische Unterstützung und viel Spaß bei der Arbeit, Ralph Krupke, mit dem ich jederzeit über meine Arbeit diskutieren konnte, Rolf Ochs, Sébastien Champigny, Jakob Brauer und Christoph Marquardt für die nette Zeit (und die Schokolade) und Ramon Rick für sein immerwährendes Interesse an allen Fragen über mechanisch kontrollierbare Bruchkontakte.

Vielen Dank auch an die Gruppe in Würzburg, Sandra Dantscher, Sven und Claudia Schramm, Walter Pfeiffer und Daniel Wolpert, mit denen ich eine sehr schöne Zeit in Würzburg verbracht habe und die sich zusammen mit mir die Nächte um die Ohren geschlagen haben, um möglichst viele Daten aufnehmen zu können.

Ebenso gebührt mein Dank den Chemikern des INT für die fruchtbare und angenehme Zusammenarbeit und viele Diskussionen: Mark Elbing, Christophe Stroh, Matthias Fischer, Mario Ruben, Marcel Major und Aitor Landa. Mark Elbing möchte ich ganz besonders danken für die schöne Zeit in unserer WG und dass er nie müde wurde, einem Physiker chemische Zusammenhänge selbst abends bei einem Bier zu erklären.

Desweiteren gilt mein besonderer Dank Michelle Di Leo und Joachim Reichert für die Einführung in die Technik mechanisch kontrollierbarer Bruchkontakte; Max Köntopp, Thomas Korb, Matthias Hettler, Ferdinand Evers, Heidi Förster und Axel Thielmann für die Einführung in die Theorie des mesoskopischen elektronischen Transportes; Fabian Pérez-Willard für die Einführung in die Herstellung von Nanoporen; Christian Lemier, Kai Grube, Paul Popovich, Stefanie Drobnik und Dominik Kramer für ausgiebige Wärmedilatationsmessungen; Stefan Walheim für Ellipsometriemessungen; Claudia Ditsches und Simone Herth für eine Einführung in die Kunst des Polierens; Stefan Linden für seine große Hilfe bei meinem optischen Aufbau; Harald Rösner für alle möglichen Materialinformationen und TEM Aufnahmen; Matthias Barczewski für Tipps und Hilfen. Erika Schütze und Olaf Wollersheim möchte ich für die vielen netten Unterhaltungen und den reibungslosen Ablauf aller organisatorischen

Dinge am INT danken. Auch gilt mein Dank den Mitarbeitern der IFP-Werkstatt, die meine Aufträge stets zuverlässig und schnell erledigten.
Mein sehr großer Dank gilt meinen KorrekturleserInnen, die mich in unermüdlicher Kleinarbeit mit einem $4\frac{1}{2}$ cm hohen Stapel voller Verbesserungsvorschläge versorgt haben: Michelle Di Leo („DiLeo.org“), Heidi Förster, Thomas Korb, Max Köntopp, Mark Elbing, Sandra Dantscher, Gernot Maier, Christiane Becker, Christian Lemier, Christoph Marquardt, Axel Thielmann und Aina Quintilla. Thomas Hertweck möchte ich für seine unschätzbaren Hilfen und Tipps zu Linux und LaTeX danken.
Ganz besonders herzlich möchte ich mich bei meinen vielen Freunden innerhalb und außerhalb des INT bedanken für die schöne Zeit, die ich in den vier Jahren meiner Arbeit hatte. Ebenso möchte ich meiner alten Arbeitsgruppe am IPE danken für ihre Unterstützung sowie die netten Frühstücke und Grillfeste.
Nicht zuletzt gilt mein besonderer Dank meinen Geschwistern, meinen Eltern und Heidi, die mich immer nach allen Kräften unterstützt haben und meiner Großmutter, die trotz ihrer 80 Jahre genau erklärt haben wollte, wie Stromtransport durch Moleküle funktioniert.

Bibliography

[1] R.L. Carroll and C.B. Gorman, The Genesis of Molecular Electronics, Angew. Chem. Int. Ed. **41**, 4378 (2002).

[2] M. Elbing, *Functional Molecular Building Blocks*, PhD thesis, Universität Karlsruhe, 2005, (FZKA-Berichte, FZKA-7102;
http://bibliothek.fzk.de/zb/berichte/FZKA7102.pdf).

[3] Cherie R. Kagan and Mark A. Ratner, Molecular Transport Junctions: An Introduction, MRS Bulletin **29**(6), 376 (2004).

[4] A. Nitzan and M.A. Ratner, Electron Transport in Molecular Wire Junctions, Science **300**, 1384 (2003).

[5] M. Mayor, H.B. Weber, and R. Waser, Molecular Electronics, in *Nanoelectronics and Information Technology*, edited by R. Waser, chapter 20, Wiley-VCH, Weinheim, 2003.

[6] Z.J. Donhauser, B.A. Mantooth, K.F. Kelly, L.A. Bumm, J.D. Monnell, J.J. Stapleton, D.W. Price Jr., A.M. Rawlett, D.L. Allara, J.M. Tour, and P.S: Weiss, Conductance Switching in Single Molecules Through Conformational Changes, Science **292**, 2303 (2001).

[7] X.D. Cui, A. Primak, X. Zarate, J. Tomfohr, O.F. Sankey, A.L. Moore, T.A. Moore, D. Gust, G. Haris, and S.M. Lindsay, Reproducible Measurement of Single-Molecule Conductivity, Science **294**, 571 (2001).

[8] L. Patrone, S. Palacin, J.P. Bougoin, J. Lagoute, T. Zambelli, and S. Gauthier, Direct comparison of the electronic coupling efficiency of sulfur and selenium anchoring groups for molecules adsorbed onto gold electrodes, Chemical Physics **281**, 325–332 (2002).

[9] G.K. Ramachandran, T.J. Hopson, A.M. Rawlett, L.A. Nagahara, A.L. Primak, and S.M. Lindsay, A Bond-Fluctuation Mechanism for Stochastic Switching in Wired Molecules, Science **300**, 1413 (2003).

[10] B. Xu and N.J. Tao, Measurement of Single-Molecule Resistance by Repeated Formation of Molecular Junctions, Science **301**, 1221 (2003).

[11] J.G. Kushmerick, J. Naciri, J.C. Yang, and R. Shashidhar, Conductance Scaling of Molecular Wires in Parallel, Nano Letters **3**, 897 (2003).

[12] A.S. Blum, J.G. Kushmerick, S.K. Pollack, J.C. Yang, M. Moore, J. Naciri, R. Shashidhar, and B.R. Ratna, Charge Transport and Scaling in Molecular Wires, J. Phys. Chem. B **108**, 18124 (2004).

[13] J. Moreland and J.W. Ekin, Electron tunneling experiments using Nb-Sn "break" junctions, Journal of Applied Physics **58**, 3888 (1985).

[14] M.A. Reed, C. Zhou, C.J. Muller, T.P. Burgin, and J.M. Tour, Conductance of a Molecual Junction, Science **278**, 252 (1997).

[15] C. Kergueris, J.-P. Bourgoin, S. Palacin, D. Esteve, C. Urbina, M. Magoga, and C. Joachim, Electron Transport through a metal-molecule-metal junction, Physical Review B **59**, 12505 (1999).

[16] R.H.M. Smit, Y. Noat, C. Untiedt, N.D. Lang, M.C. von Hemert, and J.M. van Ruitenbeek, Measurement of the conductance of a hydrogen molecule, Nature **419**, 906 (2002).

[17] D. Dulić, S.J. van der Molen, T. Kudernac, H.T. Jonkman, J.J.D. de Jong, T.N. Bowden, J. van Esch, B.L. Feringa, and B.J. van Wees, One-way opto-electronic switsching of photochromic molecules on gold, Physical Review Letters **91**, 207402 (2003).

[18] T. Böhler, J. Grebing, A. Mayer-Gindner, H. von Löhneysen, and E. Scheer, Mechanically controllable break-junctions for use as electrodes for molecular electronics, Nanotechnology **15**, S465 (2004).

[19] A.R. Champagne, A.N. Pasupathy, and D.C. Ralph, Mechanically-adjustable and electrically-gated single-molecule transistors, cond-mat , 0409134 (2004).

[20] N.B. Zhitenev, H. Meng, and Z. Bao, Conductance of Small Molecular Junctions, Physical Review Letters **88**, 226801 (2002).

[21] S. Kubatkin, A. Danilov, M. Hjort, J. Cornil, J.-L. Brédas, N. Stuhr-Hansen, P. Hedegård, and T. Bjørnholm, Single-electron transistor of a single organic molecule with access to several redox states, Nature **425**, 698 (2003).

[22] Y.V. Kervennic, D. Vanmaekelbergh, L.P. Kouwenhoven, and H.S. Van der Zant, Planar nanocontacts with atomically controlled separation, Applied Physics Letters **83**, 3782 (2003).

[23] H. van der Zant and Y.V. Kervennic, Unconventional gate effect in a molecular junction with small organic molecules, presented at the ADMOL conference, Dresden, 2004.

[24] J. Park, A.N. Pasupathy, J.I. Goldsmith, C. Chang, Y. Yaish, J.R. Petta, M. Rinkoski, J.P. Sethna, H.D. Abruña, P.L. McEuen, and D.C. Ralph, Coulomb blockade and the Kondo effect in single atom transistors, Nature **417**, 722 (2002).

[25] W Liang, M.P. Shores, M. Bockrath, J.R. Long, and H. Park, Kondo resonance in a single-molecule transistor, Nature **417**, 725 (2002).

[26] H. Park, J. Park, A.K.L. Lim, E.H. Anderson, A.P. Alivisatos, and P.L. McEuen, Nanomechanical oscillations in a single-C60 transistor, Nature **407**, 57 (2000).

[27] J.M. van Ruitenbeek, A. Alvarez, I. Piñeyro, C. Grahmann, P. Joyez, M.H. Devoret, D. Esteve, and C. Urbina, Adjustable nanofabricated atomic size contacts, Review of Scientific Instruments **67**(1), 108 (1996).

[28] H.B. Weber, J Reichert, F. Weigend, R. Ochs, D. Beckmann, M. Mayor, R. Ahlrichs, and H. von Löhneysen, Electronic transport through single conjugated molecules, Chemical Physics **281**, 113–125 (2002).

[29] J. Reichert, R. Ochs, D. Beckmann, H.B. Weber, M. Mayor, and H. von Löhneysen, Driving current through single organic molecules, Physical Review Letters **88**(17), 176804 (2002).

[30] C. Untiedt, A.I. Yanson, R. Grande, G. Rubio-Bollinger, N. Agraït, N. Vieira, and J.M. van Ruitenbeek, Calibration of the length of a chain of single gold atoms, Physical Review B **66**(8), 085418 (2002).

[31] E. Scheer, P. Joyez, D. Esteve, C. Urbina, and M.H. Devoret, Conduction channel transmissions of atomic-size aluminium contacts, Physical Review Letters **78**, 3535 (1997).

[32] E. Scheer, Agraït Nicolás, J.C. Cuevas, A.L. Yeyati, B. Ludoph, A. Martín-Rodero, G. Rubio Bollinger, L.M. van Ruitenbeek, and C. Urbina, The signature of chemical valence in the electrical conduction through a single-atom contact, Nature **394**, 154 (1998).

[33] E. Scheer, J.C. Cuevas, A.L. Yeyati, A. Martín-Rodero, P. Joyez, M.H. Devoret, D. Esteve, and C. Urbina, Conduction channels of superconducting quantum point contacts, Physica B **280**, 425–431 (2000).

[34] E. Scheer, W. Belzig, Y. Naveh, M.H. Devoret, D. Esteve, and C. Urbina, Proximity Effect and Multiple Andreev Reflections in Gold Atomic Contacts, Physical Review Letters **86**(2), 284 (2001).

[35] S. Kohler, J. Lehmann, and P. Hänggi, Driven quantum transport on the nanoscale, Physics Reports **406**, 379–443 (2005).

[36] Supriyo Datta, Electrical resistance: an atomistic view, Nanotechnology **15**, S433 (2004).

[37] A. Nitzan, Electron transmission through molecules and molecular interfaces, Ann. Rev. Phys. Chem. **52**, 681–750 (2001).

[38] M. Paulsson, Non Equilibrium Green's Functions for Dummies: Introduction to the One Particle NEGF equations, cond-mat , 0210519 (2002).

[39] D.K. Ferry and S.M. Goodnick, *Transport in nanostructures*, Cambridge Univ. Press, 1999.

[40] S. Datta, *Electronic transport in mesoscopic systems*, Cambridge Univ. Press, 1995.

[41] R. Landauer, Electrical resistance of disordered one–dimensional lattices, Philosophical Magazine **21**, 863 (1970).

[42] Y. Meir and N.S. Wingreen, Landauer Formula for the Current through an Interacting Electron Region, Physical Review Letters **68**, 2512 (1992).

[43] M.B. Koentopp, *Theory of electronic transport through molecular nanostructures*, PhD thesis, Universität Karlsruhe, 2005, (FZKA-Berichte, FZKA-7121; http://bibliothek.fzk.de/zb/berichte/FZKA7121.pdf).

[44] F. Evers, F. Weigend, and M. Koentopp, Conductance of molecular wires and transport calculations based on density-functional theory, Physical Review B **69**, 235411 (2004).

[45] Roland Wiesendanger, *Scanning Probe Microscopy and Spectroscopy. Methods and applications*, Cambridge University Press, 1994.

[46] Flemming Besenbacher, Scanning tunneling microscopy studies of metal surfaces, Rep. Prog. Phys. **59**, 1737–1802 (1996).

[47] A. Messiah, *Mécanique Quantique tome 1*, Dunod, Paris, 2^e edition, 1995, ISBN: 2 10 002426 4.

[48] J.J. Sakurai, *Modern Quantum Mechanics*, Addison Wesley, revised edition, 1994, ISBN: 0-201-53929-2.

[49] G. Binnig, N. Garcia, and H. Rohrer, Electron-metal-surface interaction potential with vacuum tunneling: Observation of the image force, Physical Review B **30**, 4816 (1984).

[50] J. Bardeen, Tunnelling from a Many-Particle Point of View, Physical Review Letters **6**, 57 (1961).

[51] G. Rubio-Bollinger, P. Joyez, and N Agraït, Metallic Adhesion in Atomic-Size Junctions, Physical Review Letters **93**, 116803 (2004).

[52] O. Yu. Kolesnychenko, O.I. Shklyarevskii, and H. van Kempen, Giant Influence of Adsorbed Helium on Field Emission Resonance Measurements, Physical Review Letters **83**(11), 2242 (1999).

[53] N.D. Lang, Theory of Single-Atom Imaging in the Scanning Tunneling Microscope, Physical Review Letters **56**, 1164 (1986).

[54] R.J.P. Keijsers, O.I. Shklyarevskii, and H. van Kempen, Spectroscopic study of the tunnel-current reduction due to adsorbed helium, Physical Review B **61**, 7328 (2000).

[55] X. Cui, M. Freitag, R. Martel, L. Brus, and P. Avouris, Controlling Energy-Level Alignments at Carbon Nanotube/Au Contacts, Nano Letters **3**, 783 (2003).

[56] R.J.P. Keijsers, J. Voets, O.I. Shklyarevskii, and H. van Kempen, Influence of the shape of the electrodes on the tunnel current, Low Temperature Physics **24**, 730 (1998).

[57] N.W. Ashcroft and N.D. Mermin, *Solid State Physics*, Saunders College, Philadelphia, international edition, 1976.

[58] P.A. Anderson, Work Function of Gold, Phys. Rev. **115**, 553 (1959).

[59] L. Olesen, M. Brandbyge, M.R. Sørensen, K.W. Jacobsen, E. Lægsgaard, I. Stensgaard, and F. Besenbacher, Apparent Barrier Height in Scanning Tunneling Microscopy Revisited, Physical Review Letters **76**, 1485 (1996).

[60] Colin J. Smithells, *Metals reference book*, Butterworths, London, 4 edition, 1967.

[61] *EnvironmentalChemistry.com*, http://environmentalchemistry.com.

[62] O.Y. Kolesnychenko, A.J. Toonen, O.I. Shklyarevskii, and H. van Kempen, Millisecond dynamics of thermal expansion of mechanically controllable break junction electrodes studied in the tunneling regime, Applied Physics Letters **79**, 2707 (2001).

[63] M. Büttiker and R. Landauer, Traversal Time for Tunneling, Physical Review Letters **49**, 1739 (1982).

[64] R. Antoine, P.F. Brevet, H.H. Girault, D. Bethell, and D.J. Schiffrin, Surface plasmon enhanced non-linear optical response of gold nanoparticles at the air/toluene interface, Chem. Commun. , 1901 (1997).

[65] J.G. Simmons, Generalized Formula for the Electric Tunnel Effect between Similar Electrodes Separated by a Thin Insulating Film, Journal of Applied Physics **34**(6), 1793 (1963).

[66] W.F. Brinkman, R.C. Dynes, and J.M. Rowell, Tunneling Conductance of Asymmetrical Barriers, Journal of Applied Physics **41**(5), 1915 (1970).

[67] F. Zahid, A.W. Ghosh, M. Paulsson, E. Polizzi, and S. Datta, Charging induced asymmetry in molecular conductors, cond-mat , 0403401 (2004).

[68] S.N. Yaliraki and M.A. Ratner, Molecule-interface coupling effects on electronic transport in molecular wires, Journal of Chemical Physics **109**, 5036 (1998).

[69] N.D. Lang and Ph. Avouris, Electrical conductance of parallel atomic wires, Physical Review B **62**, 7325 (2000).

[70] J. Lagerqvist, Y.-C. Chen, and M. Di Ventra, Shot noise in parallel wires, Nanotechnology **15**, S459 (2004).

[71] H. Ohnishi, Y. Kondo, and K. Takayanagi, Quantized conductance through individual rows of suspended gold atoms, Nature **395**, 780 (1998).

[72] P. Johansson, G. Hoffmann, and R. Berndt, Light emission from Na/Cu(111) induced by a scanning tunneling microscope, Physical Review B **66**, 245415 (2002).

[73] G. Hoffmann, J. Kröger, and R. Berndt, Color imaging with a low temperature scannung tunneling microscope, Review of Scientific Instruments **73**(2), 305 (2002).

[74] Germar Hoffmann, *Light Emission from Metals and Adsorbates in the Scanning Tunneling Microscope*, PhD thesis, Universität Kiel, 2001.

[75] T.W. Ebbesen, H.J. Lezec, H.F. Ghaemi, T. Thio, and P.A. Wolff, Extraordinary optical transmission through sub wavelength hole arrays, Nature **391**, 667 (1998).

[76] T. Thio, K.M. Pellerin, R.A. Linke, H.J. Lezec, and T.W. Ebbesen, Enhanced light transmission through an single subwavelength aperture, Optics Letters **26**(24), 1972 (2001).

[77] R. Hillenbrand, T. Taubner, and F. Kellmann, Phonon-enhanced light-matter interaction at the nanometre scale, Nature **418**, 159 (2002).

[78] A.J. Meixner, T. Vosgröne, and M. Sackrow, Nanoscale Sufrace-enhanced resonance Raman scattering spectroscopy of single molecules on isolated silver clusters, Journal of Luminescence **94-95**, 147–152 (2001).

[79] Andreas Thon, *Tunnelprozesse im intensiven Laserfeld*, PhD thesis, Universität Würzburg, 2002.

[80] A.H. Dayem and R.J. Martin, Quantum Interaction of Microwave Radiation with Tunneling Between Superconductors, Physical Review B **8**, 246 (1962).

[81] M. Paulsson and S. Datta, Thermionic effect in molecular electronics, Physical Review B , 241403 (2003), also as cond-mat: 0301232.

[82] *Introduction to Engineering Heat Transfer*, MITOPENCOURSEWARE, lecture notes of the Massachusetts Institute of Technology, 2002.

[83] F.P Incropera and D.P. De Witt, *Introduction to Heat Transfer*, John Wiley & Sons, 3 edition, 1996.

[84] *Gutekunst Stahlverformung KG*, http://www.gutekunst-kg.de/.

[85] R. Waser, editor, *Nanoelectronics and Information Technology*, Wiley-VCH, Weinheim, 2003.

[86] Michael Johannes Nasse, *Development of a Confocal and Near-field Scanning Optical Microscope for Polarization-resolved Temporal Studies of Single Nano-objects*, PhD thesis, Université Joseph Fourier, Grenoble, 2004.

[87] D.R. Stewart, D.A.A. Ohlberg, P.A. Beck, Y. Chen, R.S. Williams, J.O. Jeppesen, K.A. Nielsen, and J.F. Stoddart, Molecule-Independent Electrical Switching in PT/Organic Monolayer/Ti Devices, Nano Letters **4**, 133 (2004).

[88] D. Erts, H. Olin, L. Ryen, E. Olsson, and A. Thölén, Maxwell and Sharvin conductance in gold point contacts investigated using TEM-STM, Physical Review B **61**, 12725 (2000).

[89] *Goodfellow Material Informationen*, http://www.goodfellow.com/csp/active/static/.

[90] J.M. Tour, L. Jones II, L. Pearson, J.J.S. Lamba, T.P. Burgin, G.M. Whitesides, D.L. Allara, A.N. Parikh, and S.V. Atre, Self-Assembled Monolayers and Multilayers of Conjugated Thiols, α,ω-Dithiols, and Thioacetyl-Containing Adsorbates. Understanding Attachments between Potential Molecular Wires and Gold Surfaces, Journal of the American Chemical Society **117**(37), 9529–9534 (1995).

[91] D.T. Gryko, C. Clausen, and J.S. Lindsey, Thiol-derivatized porphyrins for attachment to electroactive surfaces, J. Org. Chem. **64**, 8635–8647 (1999).

[92] G.E. Poirier, Characterisation of Organosulfur Molecular Monolayers on Au(111) using Scanning Tunneling Microscopy, Chemical Reviews **97**, 1117 (1997).

[93] R. Berthe and J. Halbritter, Coulomb barriers and adsorbate effects in scanning tunneling microscopy, Physical Review B **43**, 6880 (1991).

[94] T. Heinzel, R. Held, S. Lüscher, K. Ensslin, W. Wegschneider, and Bichler M., Electronic properties of nanostructures defined in Ga[Al]As heterostructures by local oxidation, Physica E **9**, 84 (2001).

[95] M. Elbing, M. Di Leo, J. Reichert, C. von Hänisch, H.B. Weber, and M. Mayor, Oligophenylene Rods As Building Blocks For Molecular Electronic Devices, in preparation.

[96] Michelle Di Leo, Stromfluss durch organische Moleküle: Herstellung und Charakterisierung von Einzelmolekülkontakten, Diploma thesis, FH München, 2002.

[97] A. Aviram and M.A. Ratner, Molecular Rectifiers, Chemical Physics Letters **29**, 277 (1974).

[98] M Elbing, M. Köntopp, M. Fischer, C. von Hänisch, F. Weigend, F. Evers, H.B. Weber, and M. Mayor, A Single-Molecule Diode, Proceedings of the National Academy of Sciences **102**, 8815 (2005).

[99] Rolf Ochs, *Untersuchung der Symmetrieeigenschaften des Stromtransports durch einzelne Moleküle*, PhD thesis, Universität Karlsruhe, 2004, (FZKA-Berichte, FZKA-7074;
http://bibliothek.fzk.de/zb/berichte/FZKA7074.pdf).

[100] G. Rubio, N. Agraït, and S. Vieira, Atomic-Sized Metallic Contacts: Mechanical Properties and Electronic Transport, Physical Review Letters **76**, 2302 (1996).

[101] M. Mayor, C. von Hänisch, H.B. Weber, J. Reichert, and D. Beckmann, A *trans*-Platinum(II) Complex as a Single-Molecule Insulator, Angw. Chem. Int. Ed. **41**(7), 1183 (2002).

[102] J.A.M. Sondag-Huethorst, C. Schönenberger, and L.G.J. Fokkink, Formation of Holex in Alkanethiol Monolayers on Gold, J. Phys. Chem. **98**, 6826 (1994).

[103] K. Edinger, M. Grunze, and Ch. Wöll, Corrosion of Gold by Alkane Thiols, Physical Chemistry **101**(12), 1811 (1997).

[104] T.M. Mayer, J.E. Houston, G.E. Franklin, G.E. Erchak, and T.A. Michalske, Electric field induced surface modification of Au, Journal of Applied Physics **85**, 8170 (1999).

[105] K.H. Gundlach, Zur Berechnung des Tunnelstromes durch eine Trapezförmige Potentialstufe, Solid State Electron. **9**, 949 (1966).

[106] O.Y. Kolesnychenko, O.I. Shklyarevskii, and H. van Kempen, Calibration of the distance between electrodes of mechanically controlled break junctions using field emission resonance, Rev Sci Instrum **70**(2), 1442 (1999).

[107] M.F. Lambert, M.F. Goffman, J.P. Bourgoin, and P. Hesto, Fabrication and characterisation of sub-3 nm gaps for single-cluster and single-molecule experiments, Nanotechnology **14**, 772 (2003).

[108] N. Agraït, A.L. Yeyati, and J.M. van Ruitenbeek, Quantum properties of atomic-sized conductors, Physics Reports **377**, 81–279 (2003).

[109] R. Kizuka, Atomic Process of Point Contact in Gold Studied by Time-Resolved High-Resolution Transmission Electron Microscopy, Physical Review Letters **81**, 4448 (1998).

[110] Y. Takai, T. Kawasaki, Y. Kimura, Ikuta T., and R. Shimizu, Dynamic Observation of an Atom-Sized Gold Wire by Phase Electron Microscopy, Physical Review Letters **87**(10), 106105 (2001).

[111] V. Rodrigues and D. Ugarte, Real-time imaging of atomistic process in one-atom-thick metal junctions, Physical Review B **63**, 073405 (2001).

[112] M. Brandbyge, J. Schiøtz, M.R. Sørensen, P. Stoltze, K.W. Jacobsen, J.K. Nørskov, L. Olesen, E. Laegsgaard, I. Stensgaard, and F. Besenbacher, Quantized conductance in atom-sized wires between two metals, Physical Review B **52**, 8499 (1995).

[113] A.I. Yanson, G. Rubio Bollinger, H.E. van den Brom, N. Agraït, and J.M. van Ruitenbeek, Formation and manipulation of a metallic wire of single gold atoms, Nature **395**, 783 (1998).

[114] S.B. Legoas, D.S: Galvão, V. Rodrigues, and D. Ugarte, Origin of Anomalously Long Interatomic Distances in Suspended Gold Chains, Physical Review Letters **88**, 076105 (2002).

[115] Joachim Reichert, *Leitfähigkeitsmessungen an einzelnen organischen Molekülen*, PhD thesis, Universität Karlsruhe, 2003, (FZKA-Berichte, FZKA-6851; http://bibliothek.fzk.de/zb/berichte/FZKA6851.pdf).

[116] A. Halbritter, Sz. Csonka, G. Mihály, E. Jurdik, O.Yu. Kolesnychenko, O.I. Shklyarevskii, S. Speller, and H. van Kempen, Transition from tunneling to direct contact in tungsten nanojunctions, Physical Review B **68**, 035417 (2003).

[117] X. Xiao, B. Xu, and N.J. Tao, Measurement of Single Molecule Conductance: Benzenedithiol and Benzenedimethanethiol, Nano Letters **4**(2), 267 (2004).

[118] A. Assion, T. Baumert, M. Bergt, T. Brixner, B. Kiefer, M. Seyfried, M. Strehle, and Gerber G., Control of Chemical Reactions by Feedback-Optimized Phase-Shaped Femtosecond Laser Pulses, Science **282**, 919 (1998).

[119] V. Gerstner, A. Knoll, W. Pfeiffer, A. Thon, and G. Gerber, Femtosecond laser assisted scanning tunneling microscopy, Journal of Applied Physics **88**(8), 4851 (2000).

[120] *L.O.T.-Oriel GmbH & Co. KG*, Im tiefen See 58, 64293 Darmstadt, Germany.

[121] W. Wang, T. Lee, and M.A. Reed, Mechanism of electron conduction in self-assembled alkanethiol monolayer devices, Physical Review B **68**, 035416 (2003).

[122] J. Reichert, H.B. Weber, M. Mayor, and H. von Löhneysen, Low-temperature conductance measurements on single molecules, Applied Physics Letters **82**, 4137 (2003).

[123] Z. Burshtein and J. Levinson, Photo-induced tunnel currents in Al-Al_2O_3-Au structures, Physical Review B **12**, 3453 (1975).

[124] H. Park, A.K.L. Lim, A.P. Alivisatos, J. Park, and P.L. McEuen, Fabrication of metallic electrodes with nanometer separation by electromigration, Applied Physics Letters **75**(2), 301 (1999).

[125] Daniel Wolpert, Optische Spektroskopie an Nanokontakten, Diploma thesis, Universität Würzburg, 2004.

[126] R.A. Wassel, R.R. Fuierer, N. Kim, and C.B. Gorman, Stochastic Variation in Conductance on the Nanometer Scale: A General Phenomenon, Nano Letters **3**, 1617 (2003).

[127] Z.-C. Dong, A.S. Trifonov, X.-L. Guo, K. Amemiya, Yokoyama S., T. Kamikado, T. Yamada, S. Mashiko, and T. Okamoto, Tunneling electron induced photon emission from monolayered H_2TBP porphyrin mlecules on Cu(100), Surface Science **532-535**, 237 (2003).

[128] Z.-C. Dong, X.-L. Guo, A.S. Trifonov, P.S. Dorozhkin, K. Miki, K. Kimura, Yokoyama S., and S. Mashiko, Vibrationally Resolved Flourescence from Organic Molecules near Metal Surfaces in a Scanning Tunneling Microscope, Physical Review Letters **92**(8), 086801 (2004).

[129] G. Hoffmann, L. Libioulle, and R. Berndt, Tunneling-induced luminescence from adsorbed organic molecules with submolecular lateral resolution, Physical Review B **65**, 212107 (2002).